

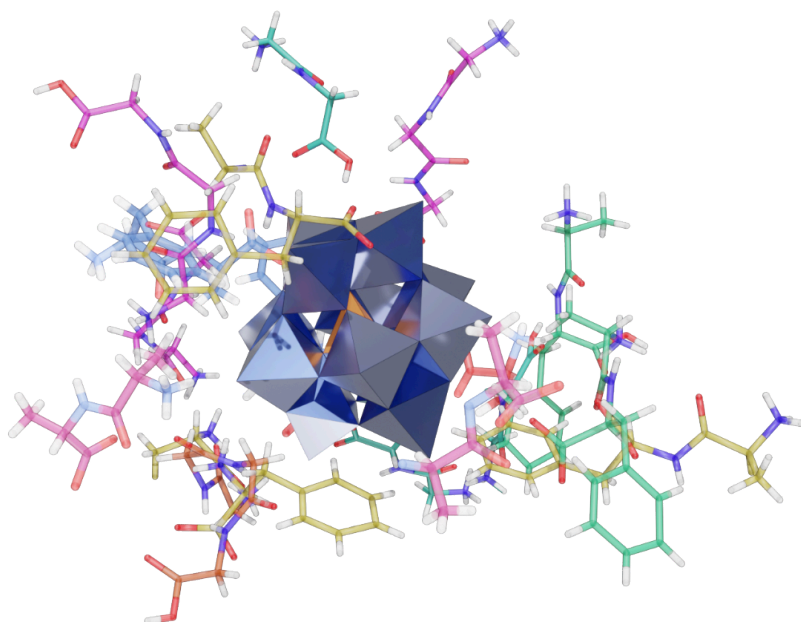


DOCTORAL THESIS NO. 2024:69
FACULTY OF NATURAL RESOURCES AND AGRICULTURAL SCIENCES

Polyoxometallate ions as models for mineral nanoparticle interactions with proteins

Insight into structure and reactivity

BJÖRN H. GREIJER



Polyoxometallate ions as models for mineral nanoparticle interactions with proteins

Insight into structure and reactivity

Björn H. Greijer

Faculty of Natural Resources and Agricultural Sciences

Department of Molecular Sciences

Uppsala



SWEDISH UNIVERSITY
OF AGRICULTURAL
SCIENCES

DOCTORAL THESIS

Uppsala 2024

Acta Universitatis Agriculturae Sueciae
2024:69

Cover: Selected structures of oligopeptides in complex with Keggin POM, overlaid to show the difference in arrangement around the POM.

ISSN 1652-6880

ISBN (print version) 978-91-8046-360-7

ISBN (electronic version) 978-91-8046-396-6

<https://doi.org/10.54612/a.6mk4ag2usu>

© 2024 Björn H. Greijer, <https://orcid.org/0000-0001-6725-5970>

Swedish University of Agricultural Sciences, Department of Molecular Sciences, Uppsala, Sweden

The summary chapter of this thesis is licensed under CC BY 4.0. To view a copy of this license, visit <https://creativecommons.org/licenses/by/4.0/>. Other licences or copyright may apply to illustrations and attached articles.

Print: SLU Grafisk service, Uppsala 2024

Polyoxometallate ions as models for mineral nanoparticle interactions with proteins

Abstract

Keywords: Polyoxometallate, Oligopeptide, X-ray single crystal study, NMR, Electrospray mass-spectrometry, Electrocatalysis

Mineral nanoparticles (NPs) form naturally by weathering of rock, and artificially by industry. They are abundant in our surroundings, so it is important to know what the effects on living organisms might be. NPs often interact with proteins, important building blocks and biocatalysts in all living things. The potential effects of NPs on proteins could be either detrimental or beneficial, and it is important to know which. Using a model system, we have identified a number of factors which can affect how NPs interact with biomolecules. These are: 1) the polarity of the metal-oxide bond, as determined by the metal atom's electronegativity; 2) the hydrophobicity of the ligand, determined in our model by the length of an oligoglycine; 3) the ionic strength of the solution, as cations in excess will compete for binding spots with the ligand, replacing it on the NP surface; 4) The shape of the ligand, as demonstrated by structure determining peptides; 5) The relative affinity of ligands, as shown by one NP readily crystallizing with a buffer molecule rather than a peptide, but not interacting noticeably with a similar buffer. Certain NPs are unstable under specific conditions, such as pH, while others tolerate it, and complexes with ligands can differ for these NPs. In addition, compounds used in the model were used as a model in a study on antiviral activity, and were also used to produce a Sol-Gel material with remarkable efficacy in electrocatalytic water splitting.

Polyoxometallatjoner som modeller för mineralnanopartiklars interaktion med proteiner

Abstract

Minerala nanopartiklar (NPs) bildas naturligt genom vittring av sten, och artificiellt från industri. De är vanliga i våra omgivningar, så det är viktigt att veta vad effekten på levande organismer kan vara. NPs interagerar ofta med proteiner, viktiga byggstenar och biokatalysatorer i alla levande ting. De potentiella effekterna av NPs på proteiner kan vara endera skadliga eller gynnande, och det är viktigt att veta vilket. Genom ett modellsystem har vi identifierat ett antal faktorer som kan påverka hur NPs interagerar med biomolekyler. Dessa är: 1) Polariteten hos metall-oxidbindningar, som bestäms av metallatomens elektronegativitet; 2) Hydrofobiciteten av liganden, som i vår modell bestäms av längden på en oligoglycin; 3) Lösningens jonstyrka, då katjoner i överflöd kan tävla om bindningsplatser med en ligand, och ersätta den på ytan av en NP; 4) Ligandens form, vilket demonstreras av strukturbestämmande peptider; 5) Den relativa affiniteten av ligander, som visas av att en NP lätt bildar kristaller med en buffertmolekyl istället för en peptid, men inte interagerar märkbart med en liknande buffert. Vissa NPs är instabila under särskilda förhållanden, så som pH, medan andra tolererar dem, och komplex med ligander kan skilja sig för dessa NPs. Dessutom var ämnen som användes i modellen även använda som en modell i en studie om antiviral aktivitet, och användes för att producera Sol-Gel-material med anmärkningsvärd effekt i elektrokatalytisk vattensplittring.

Keywords: Polyoxometallat, Oligopeptid, Röntgenkristallografi, NMR, Elektrospray mass-spectrometri, Elektrokatalys

Contents

List of publications	9
List of tables	13
List of figures	15
Abbreviations	21
1. Introduction	23
1.1 Metal oxide nanoparticles	23
1.1.1 POMs	25
1.1.2 Chemistry	26
1.2 Proteins	26
1.2.1 Oligopeptides	27
1.3 NPs in biology	27
1.4 The model system	28
1.5 Characterization techniques	29
1.5.1 X-ray diffraction	29
1.5.2 Scanning Electron Microscopy	32
1.5.3 Transmission Electron Microscopy	33
1.5.4 Energy-Dispersive X-ray Spectroscopy	33
1.5.5 Atomic Force Microscopy	35
1.5.6 Fourier Transform Infrared Spectroscopy	36
1.5.7 Mass spectrometry	37
1.5.8 Nuclear Magnetic Resonance	37
1.5.9 Thermogravimetric analysis	39
2. Methods	41
2.1 Synthesis of compounds	41
2.2 Characterization	44
2.2.1 Crystals	44
2.2.2 Other material	44

2.3	Catalysis	45
2.3.1	Peptide bond degradation	45
2.3.2	Electrocatalysis.....	45
3.	Results and discussion	47
3.1	M-O bond and hydrophobicity of ligands	49
3.1.1	Structure Nr 1 - (HGly ₃) ₃ [PMo ₁₂ O ₄₀]·5H ₂ O	49
3.1.2	Structure Nr 2 - (HGly ₃) ₃ [PW ₁₂ O ₄₀]·8H ₂ O.....	51
3.1.3	Structure Nr 3 - (HGly ₄) ₂ (H ₃ O)[PMo ₁₂ O ₄₀]·9H ₂ O	53
3.1.4	Structure Nr 4 - (HGly ₄) _{1.33} (H ₃ O) _{1.67} [PW ₁₂ O ₄₀]·H ₂ O	57
3.1.5	Discussion	60
3.2	pH and salinity	60
3.2.1	Structure Nr 5 - (HGly-Gly) ₃ [PMo ₁₂ O ₄₀]·4H ₂ O.....	61
3.2.2	Structure Nr 6 - (HGly-Gly) ₃ [PMo ₁₂ O ₄₀]·3H ₂ O.....	63
3.2.3	Structure Nr 7 - Na(HGly-Gly) ₂ [PMo ₁₂ O ₄₀]·8H ₂ O	64
3.2.4	Structure Nr 8 - Na(HGly-Gly) ₂ [PMo ₁₂ O ₄₀]·8H ₂ O	67
3.2.5	Structure Nr 9 - Na(HGly-Gly) ₂ (H ₃ O) ₃ [PMo ₁₂ O ₄₀] ₂ ·3H ₂ O	68
3.2.6	Structure Nr 10 - Na(HGly-Gly) ₂ (H ₃ O) ₃ [PMo ₁₂ O ₄₀] ₂ ·4H ₂ O.....	69
3.2.7	Structure Nr 11 - [La(H ₂ O) ₉](H ₃ O) ₃ [PW ₁₂ O ₄₀] ₂ ·19H ₂ O.....	71
3.2.8	Discussion	71
3.3	Structure determining peptides	72
3.3.1	Structure Nr 12 - (H ₃ O) ₂ (HPhe-Ala) ₄ [PW ₁₂ O ₄₀] ₂ ·11H ₂ O	73
3.3.2	Structure Nr 13 - (HAla-Phe) ₂ [HPW ₁₂ O ₄₀]·4H ₂ O	76
3.3.3	Structure Nr 14 - (HAla-Phe) ₃ [PW ₁₂ O ₄₀]	77
3.3.4	Structure Nr 15 - (HTyr) ₂ [HPW ₁₂ O ₄₀]·4H ₂ O.....	79
3.3.5	Structure Nr 16 - (HAla-Ala) ₂ [HPW ₁₂ O ₄₀]·4H ₂ O	80
3.3.6	Structure Nr 17 - (HAla) ₅ [PW ₁₂ O ₄₀] ₂ ·4H ₂ O	82
3.3.7	Discussion	83
3.4	Stabilization at higher pH via complex formation	84
3.4.1	Structure Nr 18 - (HGly ₃) ₄ [SiW ₁₂ O ₄₀]·2H ₂ O	85
3.4.2	Structure Nr 19 - (HEPES) ₃ (H ₃ O)[SiW ₁₂ O ₄₀]·H ₂ O	85
3.4.3	Discussion	86
3.5	Sol-Gel materials	86
3.5.1	ZrP	86
3.5.2	PW microspheres	89
4.	Conclusions	93
	References.....	95

Popular science summary	103
Populärvetenskaplig sammanfattning	105
Acknowledgements	107
Appendix	109
Crystallographic data	109

List of publications

This thesis is based on the work contained in the following papers, referred to by Roman numerals in the text:

- I. Greijer, B., De Donder, T., Nestor, G., Eriksson, J.E., Seisenbaeva, G.A. & Kessler, V.G. (2021). Complexes of Keggin POMs [PM₁₂O₄₀]³⁻ (M=Mo, W) with GlyGlyGly and GlyGlyGlyGly Oligopeptides. *European Journal of Inorganic Chemistry*, 2021 (1), 54–61.
<https://doi.org/10.1002/ejic.202000855>
- II. Greijer, B.H., Nestor, G., Eriksson, J.E., Seisenbaeva, G.A. & Kessler, V.G. (2022). Factors influencing stoichiometry and stability of polyoxometalate – peptide complexes. *Dalton Transactions*, 51 (24), 9511–9521.
<https://doi.org/10.1039/D2DT00717G>
- III. Greijer, B., De Turck, W., Daniel, G., Saha, J., Johnsson, M., Seisenbaeva, G.A. & Kessler, V. (2024). Functional Nanostructures from Sol–Gel Synthesis Using Keggin Polyoxometalate Phosphotungstic Acid as a Precursor. *Inorganic Chemistry*, 63 (7), 3428–3435.
<https://doi.org/10.1021/acs.inorgchem.3c04122>
- IV. Greijer, B., Stigell, E., Guerin, T. & Kessler, V.G. (2024). Complexes of Oligopeptides of Structure-Determining Amino Acids with Phosphotungstic Acid. *Crystal Growth & Design*,. *In press*, <https://doi.org/10.1021/acs.cgd.4c00806>

- V. Björn Greijer, Alexandra Nefedova, Tatiana Agback, Peter Agback, Vambola Kisand, Kai Rausalu, Alexander Vanetsev, Gulaim A. Seisenbaeva, Angela Ivask, Vadim G. Kessler (2024). Molecular Mechanisms behind the Anti Corona Virus Activity of Small Metal Oxide Nanoparticles. *Manuscript*, submitted

Papers I-V are reproduced with the permission of the publishers.

The contribution of Björn H. Greijer to the papers included in this thesis was as follows:

- I. Synthesis of compounds. Analysis of structures. Wrote major part of the manuscript.
- II. Synthesis of compounds. Participated in solving structures of compounds. Analysis of structures. Performed SEM/EDS. Performed NMR analysis. Wrote major part of the manuscript.
- III. Synthesis of compounds. Performed SEM/EDS. Participated in solving X-ray structure. Wrote major part of the manuscript.
- IV. Solved X-ray structures. Analysis of structures. Performed SEM/EDS. Wrote major part of the manuscript.
- V. Provided SiW controls. Synthesized compounds for the studies. Participated in solving X-ray structures. Wrote minor part of the manuscript.

List of tables

Table 1. An overview of the structures produced in this project.....	48
Table 2. Crystallographic data for structure 1	109
Table 3. Crystallographic data for structure 2	110
Table 4. Crystallographic data for structure 3	111
Table 5. Crystallographic data for structure 4	112
Table 6. Crystallographic data for structure 5	113
Table 7. Crystallographic data for structure 6	114
Table 8. Crystallographic data for structure 7	115
Table 9. Crystallographic data for structure 8	116
Table 10. Crystallographic data for structure 9	117
Table 11. Crystallographic data for structure 10	118
Table 12. Crystallographic data for structure 11	119
Table 13. Crystallographic data for structure 12	120
Table 14. Crystallographic data for structure 13	121
Table 15. Crystallographic data for structure 14	122

Table 16. Crystallographic data for structure 15	123
Table 17. Crystallographic data for structure 16	124
Table 18. Crystallographic data for structure 17	125
Table 19. Crystallographic data for structure 18	126
Table 20. Crystallographic data for structure 19	127

List of figures

Figure 1. Some examples of polyoxometallates. Left to right: Lindqvist ($\text{Mo}_6\text{O}_{19}^{2-}$), Keggin ($\text{PW}_{12}\text{O}_{40}^{3-}$), Dawson ($\text{P}_2\text{W}_{18}\text{O}_{62}^{6-}$), molybdenum blue ($\text{Mo}^{\text{VI}}_{126}\text{Mo}^{\text{V}}_{28}\text{O}_{462}\text{H}_{14}(\text{H}_2\text{O})_{70}^{-14}$).....	25
Figure 2. Schematic view of Molybdenum Storage Protein with ligands highlighted. Molybdate “clusters” can be seen at the centre.....	28
Figure 3. An X-ray diffractometer. The beam hits a crystal, diffracts and creates a pattern on the receiver.....	29
Figure 4. Scheme of how interference can cancel out or enhance emitted electromagnetic waves.....	31
Figure 5. Make up of a scanning electron microscope.....	32
Figure 6. Make up of a transmission electron microscope.....	33
Figure 7. Scheme of EDS mechanism.....	34
Figure 8. Make up of an atomic force microscope.....	35
Figure 9. Make up of a mass spectrometer.....	37
Figure 10. Make up of a thermogravimetric analyser.....	39
Figure 11. Structure 1 shown as molecular arrangement (A) and packing motif (B).....	49

Figure 12. Data for compound 1 . A: MS spectra. B: EDS spectrum. C: FT-IR spectrum. D: ³¹ P NMR spectrum.	50
Figure 13. Structure 2 shown as molecular arrangement (A) and packing motif (B).	51
Figure 14. Data for compound 2 . A: MS spectra. B: EDS spectrum. C: FT-IR spectrum. D: ³¹ P NMR spectrum.	52
Figure 15. Structure 3 shown as molecular arrangement (A) and packing motif (B).	53
Figure 16. Part of structure 3 , showing close contacts between PMo and tetraglycine even in groups with low charge.	53
Figure 17. Data for compound 3 . A: MS spectra. B: EDS spectrum. C: FT-IR spectrum. D: ³¹ P NMR spectrum.	55
Figure 18. MS spectra of 3 at four time points after dissolution (A). Area of signals plotted against time for 3 (B) and control without peptide (C).	56
Figure 19. Structure 4 shown as molecular arrangement (A) and packing motif (B).	57
Figure 20. Expanded packing motif of 4 , showing how tetraglycine surrounds PW and fills the gaps between the particles.	57
Figure 21. Data for compound 4 . A: MS spectra. B: EDS spectrum. C: FT-IR spectrum. D: ³¹ P NMR spectrum.	59
Figure 22. Structure 5 shown as molecular arrangement (A) and packing motif (B).	61
Figure 23. MS of 5 dissolved in (A) 0.2 M HCl, (B) water, and (C) 5 mM phosphate buffer, pH 6.5.	61
Figure 24. Data for compound 5 Displayed in A: EDS, B: TGA, C: FT-IR .	62

Figure 25. Structure 6 shown as molecular arrangement (A) and packing motif (B).....	63
Figure 26. Data for compound 6 Displayed in A: TGA, B: FT-IR	64
Figure 27. Structure 7 shown as molecular arrangement (A) and packing motif (B).....	64
Figure 28. PMo anions/particles bridged by sodium ions.....	65
Figure 29. Data for compound 7 displayed in A: EDS, B: TGA, C: FT-IR..	66
Figure 30. Structure 8 shown as molecular arrangement (A) and packing motif (B).....	67
Figure 31. EDS spectrum for compound 8	67
Figure 32. Structure 9 shown as molecular arrangement (A) and packing motif (B).....	68
Figure 33. Data for compound 9 displayed in A: TGA, B: FT-IR.....	69
Figure 34. Structure 10 shown as molecular arrangement (A) and packing motif (B).....	69
Figure 35. Data for compound 10 displayed in A: EDS, B: TGA, C: FT-IR	70
Figure 36. Structure 11 shown as molecular arrangement (A) and packing motif (B).....	71
Figure 37. pH and salinity plotted for structures in publication II.	72
Figure 38. Structure 12 shown as molecular arrangement (A) and packing motif (B).....	73
Figure 39. Structure 12 shown as packing motif with hydrophobic groups highlighted.	74
Figure 40. (A) EDS spectrum and (B) FTIR spectrum of 12	75

Figure 41. Structure 13 shown as molecular arrangement (A) and packing motif (B).....	76
Figure 42. Structure 13 shown packing motif with highlighted (A) peptide chains and (B) POM columns.....	76
Figure 43. Structure 14 shown as molecular arrangement (A) and packing motif (B).....	77
Figure 44. (A) EDS spectrum and (B) FTIR spectrum of 14	78
Figure 45. Structure 15 shown as molecular arrangement (A) and packing motif (B).....	79
Figure 46. Structure 15 shown as packing motif with (A) stacked tyrosine and (B) PW columns highlighted.	79
Figure 47. EDS spectrum of 15	80
Figure 48. Structure 16 shown as molecular arrangement (A) and packing motif (B).....	80
Figure 49. (A) EDS spectrum and (B) FTIR spectrum of 16	81
Figure 50. Structure 17 shown as molecular arrangement (A) and packing motif (B).....	82
Figure 51. (A) EDS spectrum and (B) FTIR spectrum of 17	83
Figure 52. Structure 18 shown as molecular arrangement (A) and packing motif (B).....	85
Figure 53. Structure 19 shown as molecular arrangement (A) and packing motif (B).....	85
Figure 54. A: SEM image of ZrP particles at 30 000 times magnification. B: EDS spectrum of ZrP particles.	87

Figure 55. ¹ H-NMR spectra of diglycine before incubation with ZrP (blue), after incubation (red) and a control without ZrP (green).	88
Figure 56. A: ¹ H-NMR spectra focused on the Gly signal at different times of incubation (normalized against a DSS signal). B: Integral of signals plotted against time.	89
Figure 57. A-C: TEM of PW microspheres. D-G: AFM of microspheres.	90
Figure 58. Analysis of PW microspheres. A: SEM image. B: XRPD. C: Size distribution. D: TGA curve. E: EDS spectrum.....	91
Figure 59. Electrochemical measurements at pH 0, 3, and 7. A: LSV, B: CV, C: pH dependence of the overpotential and Tafel slope.	92

Abbreviations

AFM	Atomic Force Microscopy
Ala	Alanine
CA	Chronoamperometry
CV	Cyclic Voltammetry
EDS	X-ray Energy Dispersive Spectroscopy
Gly	Glycine
HEPES	4-(2-hydroxyethyl)-1-piperazineethanesulfonic acid
HER	Hydrogen Evolution Reaction
LSV	Linear Sweep Voltammetry
MES	(2-(N-morpholino)ethanesulfonic acid)
MOF	Metal-Organic Framework
MS	Mass-Spectrometry
NMR	Nuclear Magnetic Resonance
NP	Nanoparticle
OER	Oxygen Evolution Reaction
Phe	Phenylalanine
PMo	Phosphomolybdic acid
POM	Polyoxometallate
PW	Phosphotungstic acid
RHE	Reversible Hydrogen Electrode
ROS	Reactive Oxygen Species
SEM	Scanning Electron Microscope
SiW	Silicotungstic acid
TEM	Transmission Electron Microscope
TGA	Thermogravimetric Analysis
Tyr	Tyrosine

XRPD
ZrP

X-ray Powder Diffraction
Zirconium phosphate

1. Introduction

Billions of years ago, Life first emerged in the primordial soup. This mixture contained organic molecules, formed randomly over eons of wet, hot and electric conditions, as well as minerals weathered, dissolved and reformed as nanoparticles due to the same. Mineral nanoparticles (NPs) have been with us since the beginning, and still affect us in ways that are not always clear. This work may shed a small light on what, exactly, NPs do to us.

1.1 Metal oxide nanoparticles

Metal oxide nanoparticles (NPs) are a highly diverse class of compounds, consisting of oxides of main group or transition metals, which form particles in the 1-100 nanometre range. These will form naturally over time from weathering of minerals, but can also be synthesized artificially for a purer or more specialized product. Some of the most common natural NPs include certain clays and iron or manganese oxides. Such NPs often contribute to biological abundance by making micronutrients available to organisms, for example by providing iron to phytoplankton (Hochella et al. 2008).

When synthesizing NPs, they can be doped. That is, other elements than the main constituents can be included. This is often done to enhance physical or chemical properties, such as conductivity, catalytic ability, or structure (Guo et al. 2013; Chavali & Nikolova 2019; Chen et al. 2020; Zhou et al. 2020).

Many of the chemical properties of NPs are dependent on how the surface is composed (Lundqvist et al. 2008), as it is the surface which interacts with the surroundings. NPs are ideal for catalysis, as they, due to the square cube law, have much greater surface area than larger particles. The square cube

law states that as objects grow in size, the volume increases at a faster rate than the surface area. Conversely, a given mass of material has much higher net surface area if it is divided into smaller particles. This makes NPs more effective than the bulk material of the same compound.

Photocatalysis can occur directly, where photoexcitation of the catalyst causes redox reactions in a molecule, or indirectly, through various reactive oxygen species (ROS), which attack the molecule (Bertucci & Lova 2024). Other means of producing ROS, such as the Fenton reaction (Koppenol 1993), requires addition of chemical precursors, e.g. hydrogen peroxide, but with an efficient photocatalyst only water and light are needed. Electrocatalysis also adds or removes electrons from a molecule, but through electric potential rather than excitation. This approach necessitates contact with the electrode, so the surface material needs to be conductive, have affinity with the reagents, as well as having a large surface area (McCreery 2008; Roduner 2018). Many reactions in nature are catalysed by enzymes, but due to the limitations and challenges of working with protein catalysts at larger scales, alternatives are sought. Nanozymes, NPs which mimic enzyme activity, can replace enzymes for many purposes (Wei & Wang 2013).

Many NPs are amorphous, vary in size and shape, and are not completely homogeneous in their makeup. For these reasons, it is difficult to study their interactions with other compounds in close detail. Fortunately, there are NPs without these drawbacks, which can be used as a model for the less amenable ones.

1.1.1 POMs

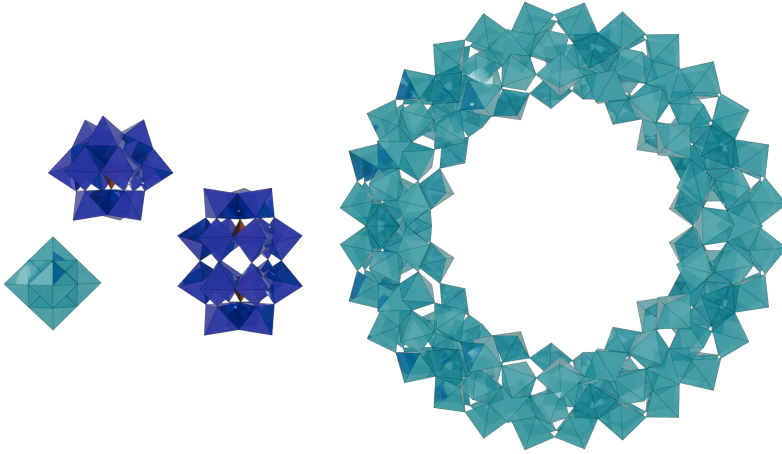


Figure 1. Some examples of polyoxometallates. Left to right: Lindqvist ($\text{Mo}_6\text{O}_{19}^{2-}$), Keggin ($\text{PW}_{12}\text{O}_{40}^{3-}$), Dawson ($\text{P}_2\text{W}_{18}\text{O}_{62}^{6-}$), molybdenum blue ($\text{Mo}^{\text{VI}}_{126}\text{Mo}^{\text{V}}_{28}\text{O}_{462}\text{H}_{14}(\text{H}_2\text{O})_{70}^{-14}$).

Polyoxometallates (POMs) are a class of NPs consisting of a series of distinctly ordered arrangements of metal oxides (Fig. 1). They are typically small, water soluble, and chemically individual. They form by nucleation of dissolved metal oxides, very similar to the Sol-Gel process (Kessler & Seisenbaeva 2023). Nearly all metals can form some kind of POM, particularly as an intermediate when forming bulk oxide materials. POMs stable at less extreme conditions tend to be based on molybdenum, tungsten, vanadium, niobium or tantalum.

The earliest described, and perhaps most well studied, POM are the Keggin POMs (Keggin & Bragg 1934), which consist of a central heteroatom in a cage of twelve transition metal atoms in their highest oxidation state, with the formula $[\text{XM}_{12}\text{O}_{40}]^n$ for the anion ($\text{X} = \text{P}, \text{Si}; \text{M} = \text{W}, \text{Mo}, \text{V}$). Since then, the diversity of POMs have exploded. Keggin POMs have been modified with titanium (Hayashi et al. 2005), iron (Farsani & Yadollahi 2014), zirconium (T. Ly et al. 2013), niobium (Abramov et al. 2016) among others. A number of distinct structures have also appeared, from the small Lindqvist structure, to the huge wheels of molybdenum blue (Müller et al. 1995, 1998). Many of these different types have also been modified with heteroatoms (Coyle et al. 2012; Anyushin et al. 2018), and even organic

groups (Di et al. 2020; Salazar Marcano et al. 2024). Beyond modifying the POMs themselves, they can be used as components in higher order structures (Amiri et al. 2021; Soria-Carrera et al. 2022; Salazar Marcano et al. 2024), and have seen some use in protein crystallography (Bijelic & Rompel 2015).

1.1.2 Chemistry

Keggin phosphometallic acids are unstable at neutral and alkaline conditions, but form spontaneously in acidic conditions if the phosphate to metallate ratio is 1:12. This degradation is stepwise, with certain pH ranges providing the $[\text{PM}_{11}\text{O}_{39}]^{-7}$ or $[\text{PM}_9\text{O}_{34}]^{-9}$ lacunary anions, among others (Zhu et al. 2003; Bajuk-Bogdanović et al. 2016; I. Gumerova & Rompel 2020). Modulating the pH allows for control of which species is dominant in a solution. It also allows modification of the POM, by inserting a different metal ion in the open spot. These doped POMs sometimes exhibit increased catalytic activity (Absillis & Parac-Vogt 2012; Coyle et al. 2012; Aoto et al. 2014; Song et al. 2016; Sun et al. 2020). Even the unmodified POM is reactive, particularly under intense light (Han et al. 2002). As the metals are in their highest oxidation state, +6, the phosphotungstic (PW) and phosphomolybdic (PMo) acids are readily reduced to lower oxidation states (I. Gumerova & Rompel 2020), which can be observed as a colour change. PW is normally colourless, and PMo yellow, while the reduced forms are blue for both, often showing as a green mixture for PMo. Such redox-properties are attractive in many areas. In some cases, partial reduction of POM can lead to novel structures (Long et al. 2013; Colliard & Nyman 2021)

1.2 Proteins

When introduced into a biological context, NPs often form a shell of different protein species, called a protein corona (Cedervall et al. 2007; Lundqvist et al. 2008).

Proteins are one of the universal biopolymer molecules present in all life, along with DNA and RNA. They are highly diverse in structure and function, and are used for everything from building blocks to catalysis. Proteins are polymers of amino acids, folded into shapes that determine their function. Most amino acids have side chains, and are divided into types based on their properties. Hydrophobic side chains are typically found in the core of globular proteins, and play a greater role in maintaining the structure, while

hydrophilic side chains are more often found on the surface, and interact with the environment. Certain spatial arrangements of residues can aid in chemical reactions, such as the “catalytic triad,” a motif often found in proteases (Buller & Townsend 2013).

An important function of proteins is signalling (Hamm 1998). Receptors detecting changes in the environment by binding ligands, thus changing conformation in a way that transmits the signal is essential in e.g. neuron communication (Tuteja 2009). Other signalling pathways include modifications to the protein, e.g. phosphorylation by kinase enzymes (Johnson 2015). This is common in the immune system. Phosphate groups often bind strongly to mineral NPs (Daou et al. 2007; Antelo et al. 2015), and so NPs may interfere with biological processes through such a mechanism.

1.2.1 Oligopeptides

Oligopeptides are similar in makeup to proteins, but contain fewer amino acid residues, between 2 and 20. Naturally occurring oligopeptides are frequently employed as toxins (Meinecke & Meinecke-Tillmann 1993; Faltermann et al. 2014). Those used in this project are 2-4 residues, largely for the sake of simplicity, as they are easy to work with in respect to solubility, availability, and characterization.

1.3 NPs in biology

Mineral weathering causes formation of natural NPs. It is therefore reasonable to assume they were present since the very beginnings of life on Earth (Sharma et al. 2015). Interactions between early biomolecules and NPs might have been as inevitable as their interaction with water. Indeed, there are still proteins which bind NPs, e.g. the Molybdenum Storage Protein (Fig. 2) (Brünle et al. 2018).

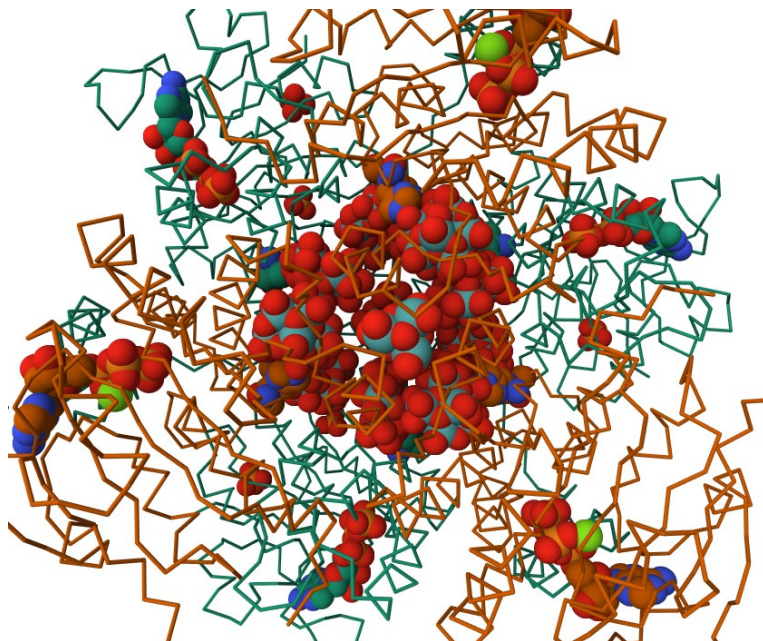


Figure 2. Schematic view of Molybdenum Storage Protein with ligands highlighted. Molybdate “clusters” can be seen at the centre.

In modern times, research into NP interactions with biomolecules is largely centred on medical applications. Natural and artificial NPs are frequently employed for e.g. drug delivery (Blanco et al. 2015). Many drugs are difficult to deliver to the location where they are effective, so a delivery system may be required. NPs which can bind drugs and are themselves nontoxic can be used for this purpose. Their large surface area, which can be further increased through porosity, also means more of the drug can be loaded, and a higher dose can be achieved. Depending on the properties of the NP, the release of the drug can be controlled. A slow release is desired when treating chronic conditions, while a faster release is better for e.g. painkillers.

1.4 The model system

Because NPs are not typically homogeneous in size and shape (Karlsson et al. 2009), an analogue is needed to study their interactions with different molecules. Proteins are difficult to study for different reasons, i.e. short lifetime and lengthy synthesis and purification. While there are established

methods for studying them at the atomic level (Timofeev & Samygina 2023), they are time consuming and expensive. Thus, an analogue of proteins is also necessary to facilitate the experiments.

This project seeks to create a model system of how NPs might interact with biomolecules, specifically proteins, by analysing complexes of Keggin POMs with oligopeptides. Keggin POMs have a similar surface to NPs, while being far more consistent in their structure, and thus more suitable for X-ray crystallography. Oligopeptides are similar to proteins, but are far simpler to work with. By studying complexes of POMs and oligopeptides, one can make predictions about how NPs and proteins might interact.

1.5 Characterization techniques

These techniques were used to analyse the materials produced.

1.5.1 X-ray diffraction

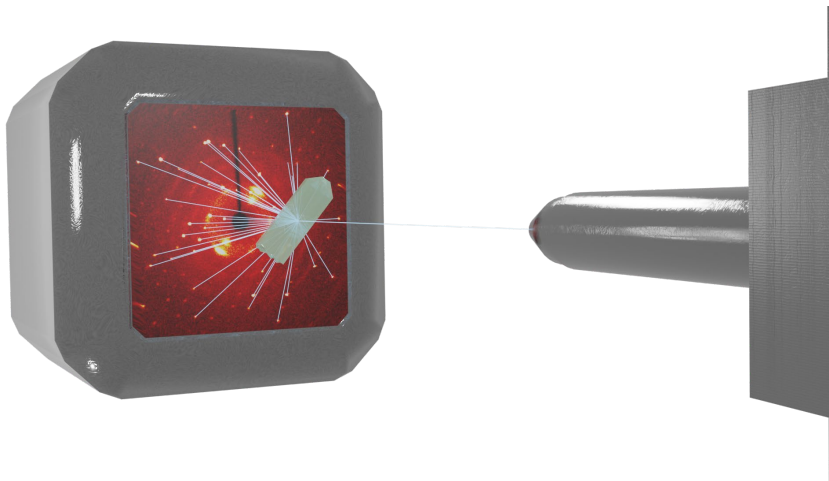


Figure 3. An X-ray diffractometer. The beam hits a crystal, diffracts and creates a pattern on the receiver.

Single crystal X-ray crystallography is a means of observing materials on an atomic level. It is done by shooting a crystal with a beam of X-rays ($\lambda = 0.1 - 10$ nm) and collecting the resulting diffraction pattern (Fig. 3) at many

different angles. The pattern occurs due to the unique properties of crystals, i.e. their symmetrical, repeating makeup. The X-rays interact with the electrons in the atoms making up the crystal to an extent proportional to the size of the atom, and thus the amount of electrons. Knowing the intensity and angle of the reflections and the distance between the crystal and the detector, the structure of the crystal material can be solved mathematically.

The nature of a crystal causes planes in the structure, along which atoms are ordered in repeating patterns. Diffraction patterns occur for an X-ray beam hitting a crystal when Bragg's law (equation 1) is satisfied:

$$1 \qquad n\lambda = 2d \sin \theta$$

Where n is an integer, λ is the wavelength, d is the distance between planes and θ is the angle between the plane and the X-ray beam (Fig. 4A). The result of this is that due to interference between the reflected beams, only certain portions are visible (Fig. 4B). Destructive interference, where they are out of phase and negate each other, gives a weaker signal (Fig. 4C), while constructive interference, where the beams are in phase and combine into a single beam, gives a stronger signal (Fig. 4D). The result is the "starry sky" illustrated in Fig. 3.

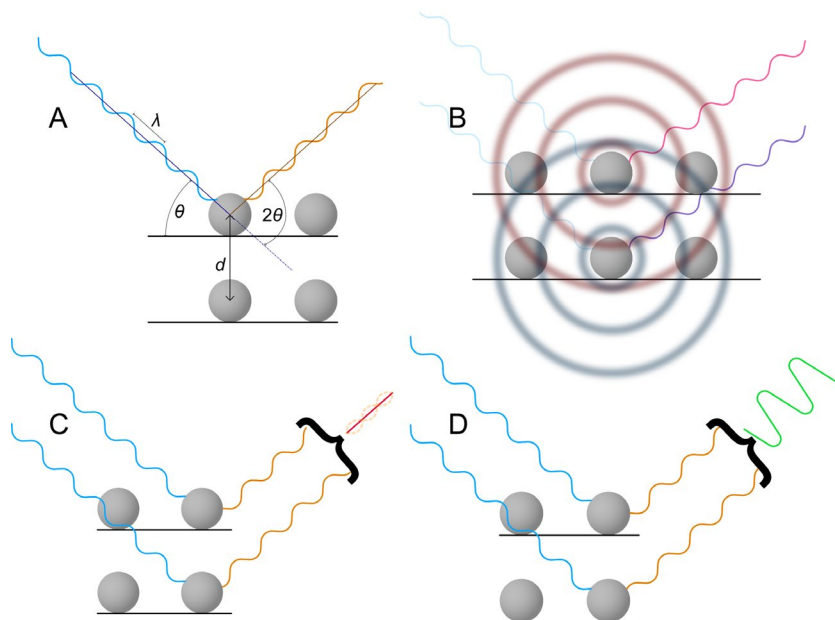


Figure 4. Scheme of how interference can cancel out or enhance emitted electromagnetic waves.

The reflections are recorded with intensity and angles relative to the beam, as well as the rotation of the crystal. From this, an electron density map is constructed, where atoms correspond to high concentrations of electrons. It is then necessary to refine the structure, as the crystal is rarely perfectly ordered; the disorder needs to be treated by various statistical operations. Once the structure is solved, however, it shows how the atoms in the crystal are arranged.

Powder diffraction uses the same principles, but instead of using a single, large crystal, it uses a multitude of tiny ones, assumed to be arranged randomly. This means the pattern recorded is a series of concentric rings rather than a pattern of dots, as it collects every possible angle all at once. Solving the structure can be attempted with this method through Rietveld refinement (Rietveld 1969), though most commonly the pattern of the rings can be turned into a graph showing their intensity plotted against the scattering angle. Each compound has a unique “fingerprint” in such a graph, allowing identification of the material.

1.5.2 Scanning Electron Microscopy

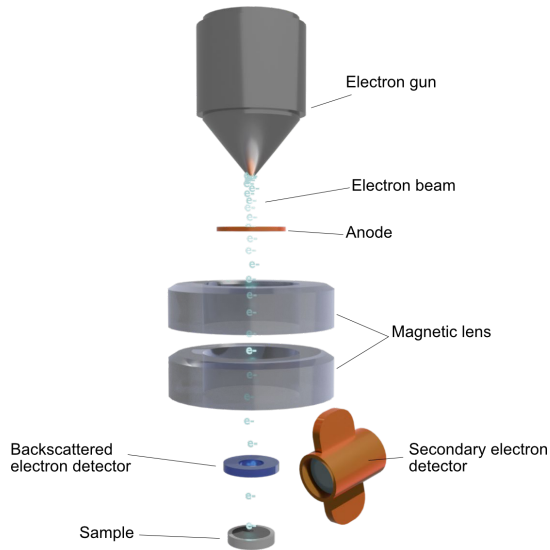


Figure 5. Make up of a scanning electron microscope.

SEM (Fig. 5) works by launching electrons towards a sample, then detecting the backscattered or secondary electrons. Electrons are ejected by an electron gun and the beam is focused and directed using magnetic lenses. When electrons hit the sample, it emits electrons and radiation which can be detected. The sample is loaded on a stage covered in carbon or copper tape, depending on its contents. Because SEM requires vacuum, the water (or other solvents) should be removed from the sample beforehand. If this is not feasible, e.g. if high vacuum will damage the sample, instruments with variable pressure exist. Some samples need to be sputtered, i.e. covered by a thin layer of gold, to improve the conductivity of the sample. Different materials can have different conductivity, which is visible as different intensity in the image. Certain materials will also build up charge, which can change the intensity in the image, and possibly damage the sample. More information can be found in Egerton 2016.

1.5.3 Transmission Electron Microscopy

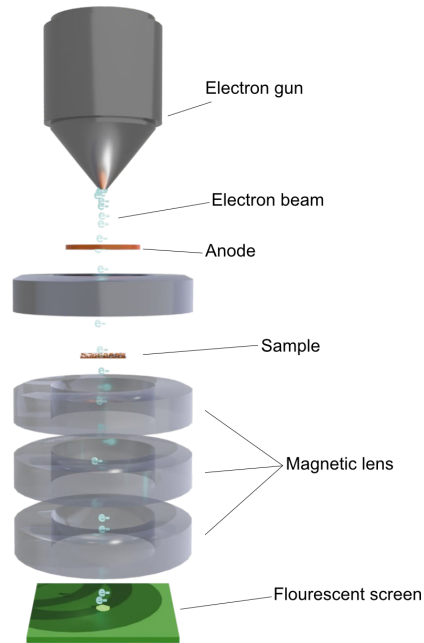


Figure 6. Make up of a transmission electron microscope.

In TEM (Fig. 6), electrons are made to pass through a thin layer of sample material, and the image detected is formed by the electron beam interacting with the electrons in the sample. The sample is often a thin sheet or a suspension on a grid. Similar to SEM, the electron beam is focused using magnetic lenses, but the image is detected by an imaging device, such as a fluorescent screen, photographic film, etc. For certain samples, TEM is preferable to SEM, as it can reach higher resolution and has higher contrast in images. However, as electrons need to pass through the sample, thicker pieces of material are not as suitable as thin films and small particles. More information on TEM can be found in Williams & Carter 1996.

1.5.4 Energy-Dispersive X-ray Spectroscopy

EDS is used for elemental analysis of a sample. If a material is made to emit X-rays, the distinct wavelengths of the radiation can be used to identify which elements are present. This is done by shooting a beam of electrons or

X-rays at the sample, which excites the electrons of lower energy in the atoms. As this creates a hole in a lower electron shell, an electron from a higher shell is sucked down to take the vacant spot, and emits an X-ray photon with a distinctive energy level in the process (Fig. 7). The number of photons and their energy can be measured, yielding information about the presence of elements and their approximate relative amounts. The peaks representing each element, or rather each energy difference between two electron shells, can be predicted by Moseley's law (equation 2), which states that the square root of the frequency (ν) of the emitted X-ray is approximately proportional to the atomic number (Z). More details can be found in Egerton 2016.

2

$$\sqrt{\nu} \propto Z$$

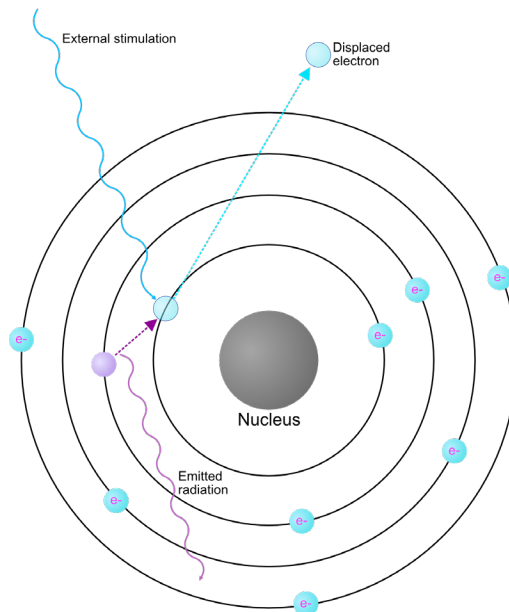


Figure 7. Scheme of EDS mechanism.

1.5.5 Atomic Force Microscopy

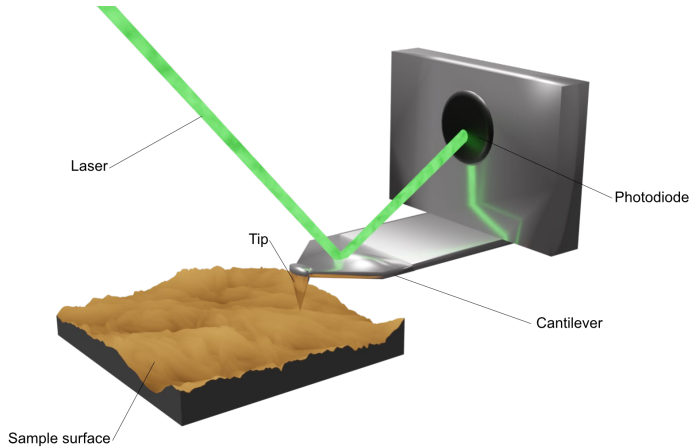


Figure 8. Make up of an atomic force microscope.

AFM works by a needle hovering above a sample, and moving back and forth across the surface. A laser is pointed at the cantilever the needle is attached to, and its reflected trajectory is tracked (Fig. 8) and used to reconstruct the surface of the sample. The needle can be either touching the sample directly (contact mode), have intermittent contact (tapping mode), or hover slightly above the surface (non contact mode). The tip of the needle can be as fine as a few nanometres, and can therefore have a very high resolution. Contact mode is more suitable for hard samples, as softer samples such as gels or biological samples can be damaged by the contact. The “stickiness” of a sample can also affect the quality of the image, as the needle sticks to the surface rather than gliding across it. In tapping and non contact mode the cantilever oscillates at or just above its resonance frequency. In tapping mode the needle “taps” the surface rather than scrape it, which makes it a more gentle method as compared to contact mode. In non contact mode the needle is affected by non-physical interactions with the sample, such as van der Waals forces or electrostatic interactions. Non contact mode does not risk damaging the needle, though it can be affected by adsorbed fluids on the sample surface, which would be penetrated in contact or tapping mode. In any mode, AFM is highly sensitive to vibrations in the environment, which

can cause distortions in the image. More information on AFM can be found in Haugstad 2012.

1.5.6 Fourier Transform Infrared Spectroscopy

FT-IR is a method for determining which wavelengths of light are absorbed by a sample. It is similar in principle to spectrophotometry, but the approach is different. Where spectrophotometry uses a series of beams with a single wavelength at a time to construct a spectrum, FT-IR uses a series of beams with a mixture of multiple wavelengths, and then computationally reconstructs the spectrum based on how much of each beam is absorbed. The raw data is processed by Fourier transformation, a mathematical operation that turns it into a graph of light intensity plotted against displacement of a mirror in an interferometer. The data obtained shows which wavelengths are absorbed, and this can be correlated to which chemical bonds are present in the sample. The sample can be in solution or suspended in a pellet, if solid. The latter method was used in the experiments described here. The dry sample is mixed with potassium bromide (KBr) and pressed into a disk using a hydraulic press, then mounted in the FT-IR instrument for data collection. Halide salts such as KBr or KI are used as they give minimal background noise; the intensity of their signals are low and their major absorption bands are not within the analysed region. As KBr is highly hygroscopic, it is important that the sample material is as dry as possible. More information can be found in Fleming & Williams 2019.

1.5.7 Mass spectrometry

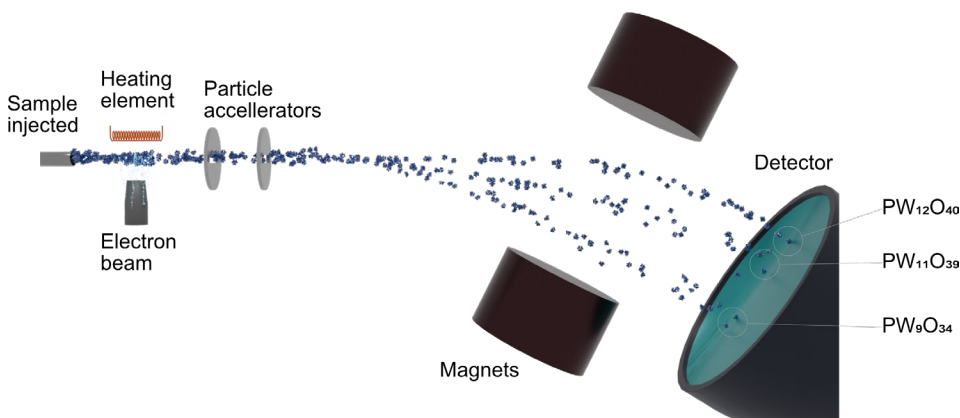


Figure 9. Make up of a mass spectrometer.

In mass spectrometry (MS), the mass to charge ratio, m/z , of molecules in a sample is measured. In many cases, the charge is +1, and so m/z is equal to the mass of the molecule. A sample solution is injected in a chamber where it is vaporized and ionized. The ions are accelerated by a magnetic field, and their path is bent by passing through a second magnetic field at an angle (Fig. 9). The degree to which the ions' path is disturbed depends on how strongly the magnetic field affects them, dependent on their charge (z), and the momentum of the particles, which depends on their mass (m). Once the ions hit the detector, the location they land in is determined by the m/z ratio, and particles with the same ratio will land in the same spot. This technique is often sensitive enough to distinguish isotopes of the same element from each other, making it useful for identifying products. A mass spectrum shows the m/z against the intensity, i.e. the number of hits over a time period. It is difficult to obtain quantitative data, but it can be done by adding a standard of known concentration. More information can be found in Fleming & Williams 2019.

1.5.8 Nuclear Magnetic Resonance

By placing a sample in a magnetic field, the nuclear magnetic moment of atoms will align with it if it has a non-zero nuclear spin, which generally occurs for isotopes with an odd atomic weight, such as 1H , ^{13}C , ^{19}F , and ^{31}P ,

all of which are commonly studied by NMR spectroscopy. However, as ^1H is common in water, it is often an unsuitable solvent for NMR experiments. Instead, deuterated solvents, such as D_2O , are used. An oscillating magnetic field is applied to the sample. At a certain frequency, called the resonant frequency, the nuclear magnetic moment begins to flip, which can be measured. Electrons near the nucleus shifts the resonant frequency. If the electrons' magnetic moment fluctuate, the nuclei will return to their starting position, a process called relaxation. The shifts in relaxation time gives information about the electrons in the sample. NMR is mainly used to analyse compounds in solution.

Different setups in an NMR experiment can give different kinds of information. For example, one can see which atoms are close to each other both physically and in terms of number of chemical bonds, giving structural information. The field of protein NMR is an advanced application of this concept. One difference between NMR and X-ray crystallography is that the latter analyses molecules in the solid state, and the former the dissolved state. NMR in two dimensions and higher can give information about distances and interactions between atoms, while X-ray gives positions of atoms, where the distance between them can imply interactions. NMR can also give information about dynamic processes; in this case one will observe overlapping structures, whose intensity corresponds to their frequency in the sample. The same principle can be applied for kinetics studies; reactants and products can be distinguished by their resonant frequencies, and their intensities will vary over time. More information can be found in Fleming & Williams 2019.

1.5.9 Thermogravimetric analysis

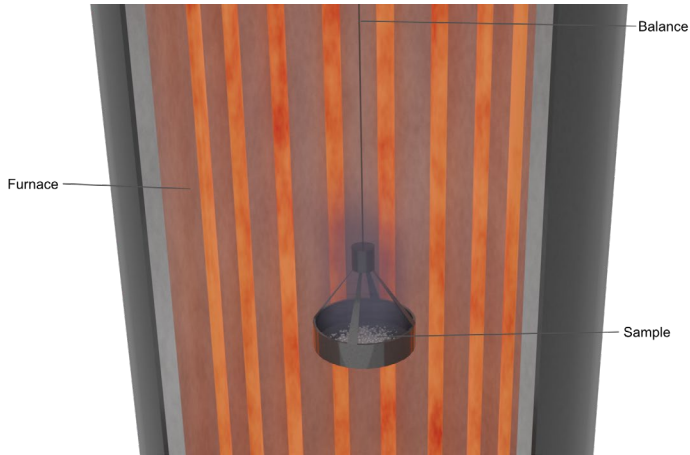


Figure 10. Make up of a thermogravimetric analyser.

TGA is a type of analysis where the mass of a sample is tracked over different temperatures using a thermobalance; a precision balance combined with a furnace where the sample is heated (Fig. 10). The speed of rising temperature can be controlled, as can the atmosphere surrounding the sample. The data takes the form of a graph where mass is plotted against temperature, and the information given concerns mainly sorption, thermal decomposition, and phase transitions (Seisenbaeva et al. 2004).

2. Methods

This section details how compounds were synthesized, characterized and tested for catalysis.

2.1 Synthesis of compounds

Complexes of peptides and POMs were made by the general procedure of adding 1 mmol POM and 3 mmol peptide to 0.1 M HCl, dissolving and allowing the solvent to evaporate. The procedure was modified as needed, for example by increasing the concentration of acid, diluting the solution in a larger volume of acid, or freezing the POM and peptide solutions separately and allowing them to mix as they thawed.

1 ((HGly₃)₃[PMo₁₂O₄₀]·5H₂O) was synthesized by mixing 0.03 mmol PMo dissolved in 1 mL 0.1 M HCl and 0.09 mmol triglycine dissolved in 1 mL 0.1 M HCl. The POM solution was added to the peptide solution and the mixture was left to evaporate.

2 ((HGly₃)₃[PW₁₂O₄₀]·8H₂O) was synthesized by mixing 0.03 mmol PW dissolved in 1 mL 0.1 M HCl and 0.09 mmol triglycine dissolved in 1 mL 0.1 M HCl. The POM solution was added to the peptide solution and the mixture was left to evaporate.

3 ((HGly₄)₂(H₃O)[PMo₁₂O₄₀]·9H₂O) was synthesized by mixing 0.03 mmol PMo dissolved in 1 mL 1 M HCl and 0.09 mmol tetraglycine dissolved in 1 mL 1 M HCl. The POM solution was added to the peptide solution and the mixture was left to evaporate.

4 ((HGly₄)_{1.33}(H₃O)_{1.67}[PW₁₂O₄₀]·H₂O) was synthesized by mixing 0.03 mmol PW dissolved in 3 mL 0.1 M HCl and 0.09 mmol tetraglycine

dissolved in 3 mL 0.1 M HCl. The POM solution was added to the peptide solution and the mixture was left to evaporate.

5 ((HGly-Gly)₃[PMo₁₂O₄₀]·4H₂O) was synthesized by mixing 0.03 mmol PMo dissolved in 0.5 mL 0.1 M HCl and 0.03 mmol diglycine dissolved in 0.5 mL 0.1 M HCl. The POM solution was added to the peptide solution and the mixture was left to evaporate.

6 ((HGly-Gly)₃[PMo₁₂O₄₀]·3H₂O) was synthesized by mixing 0.03 mmol PMo dissolved in 0.5 mL 0.1 M HCl and 0.03 mmol diglycine dissolved in 0.5 mL 0.1 M HCl. The POM solution was added to the peptide solution and the mixture was heated to >90°C, cooled to room temperature, then left to evaporate.

7 (Na(HGly-Gly)₂[PMo₁₂O₄₀]·8H₂O) was synthesized by dissolving 1.57 mmol ammonium heptamolybdate and 11 mmol sodium carbonate and boiling off the solvent and ammonia. 1 mmol iron(III) nitrate was dissolved in 2 mL 0.1 M HCl, 1 mmol sodium phosphate dibasic dihydrate was dissolved in 2 mL water, and 3 mmol diglycine was dissolved in 2.5 mL water. The phosphate solution was added to the molybdate material and concentrated HCl (12 M) was added until the solution turned yellow. The yellow solution was added to the hot iron solution slowly. The diglycine solution was added and the solution was cooled to room temperature.

8 (Na(HGly-Gly)₂[PMo₁₂O₄₀]·8H₂O) was synthesized by dissolving 11 mmol sodium molybdate and 1 mmol sodium dihydrogen phosphate in 10 mL water, 1 mmol iron nitrate nonahydrate in 5 mL 1 M HCl, and 1 mmol diglycine in 1 mL 0.1 M HCl. Concentrated HCl (12 M) was added to the molybdate/phosphate solution until yellow. The yellow solution was added to the iron solution. The diglycine solution was added and the mixture was heated to >90°C, then cooled to room temperature.

9 (Na(HGly-Gly)₂(H₃O)₃[PMo₁₂O₄₀]₂·3H₂O) was synthesized by dissolving 11 mmol sodium molybdate and 1 mmol sodium dihydrogen phosphate in 10 mL water, and 1 mmol titanium(IV) oxysulfate in 5 mL concentrated HCl, by vigorous stirring at above 80 °C. Concentrated HCl (12 M) was added to the molybdate/phosphate solution until yellow. The yellow solution was added slowly to the titanium solution. 3 mmol diglycine was added directly to the solution, and it was cooled to room temperature.

10 (Na(HGly-Gly)(H₃O)[PMo₁₂O₄₀]·3H₂O) was synthesized by dissolving 1 mmol sodium dihydrogen phosphate and 11 mmol sodium molybdate in 5 mL water, and adding concentrated HCl (12 M) until the

solution turned yellow. 1 mmol zirconyl chloride octahydrate dissolved in 5 mL water was added to the phosphomolybdate solution. White precipitate formed. 3 mmol diglycine dissolved in 2 mL 0.1 M HCl was added, and the solution was kept at $> 70^{\circ}\text{C}$ for several hours.

11 ($[\text{La}(\text{H}_2\text{O})_9](\text{H}_3\text{O})_3[\text{PW}_{12}\text{O}_{40}]_2 \cdot 19\text{H}_2\text{O}$) was synthesized by dissolving 1 mmol lanthanum nitrate in HCl at $\text{pH} < 0.1$. 1 mmol PW was added and the solution was placed in water bath at $> 90^{\circ}\text{C}$ to evaporate, without stirring. When 12 mL of the solvent remained, the solution was cooled to room temperature. Crystals were stable under mother liquor, but degraded into white powder within several hours if left in air.

12 ($(\text{H}_3\text{O})_2(\text{HPhe-Ala})_4[\text{PW}_{12}\text{O}_{40}]_2 \cdot 11\text{H}_2\text{O}$) was synthesized by dissolving 0.01 mmol PW in 5 mL 0.5 M HCl, and 0.03 mmol Phe-Ala in 5 mL 0.5 M HCl. The peptide solution was added to the PW solution and left to evaporate.

13 ($(\text{HAla-Phe})_2[\text{HPW}_{12}\text{O}_{40}] \cdot 4\text{H}_2\text{O}$) was synthesized by dissolving 0.01 mmol PW in 5 mL 0.5 M HCl, and 0.03 mmol Ala-Phe in 5 mL 0.5 M HCl. The peptide solution was added to the PW solution and a portion of the mixture was transferred to a petri dish, then left to evaporate. Crystals formed over night,

14 ($(\text{HAla-Phe})_3[\text{PW}_{12}\text{O}_{40}]$) was synthesized by dissolving 0.01 mmol PW in 5 mL 0.5 M HCl, and 0.03 mmol Ala-Phe in 5 mL 0.5 M HCl. The peptide solution was added to the PW solution and left to evaporate. Crystals formed after several months.

15 ($(\text{HTyr})_2[\text{HPW}_{12}\text{O}_{40}] \cdot 4\text{H}_2\text{O}$) was synthesized by dissolving 0.01 mmol PW in 5 mL 0.1 M HCl, and 0.03 mmol tyrosine in 5 mL 0.1 M HCl. The peptide solution was added to the PW solution and a portion of the mixture was transferred to a petri dish, then left to evaporate.

16 ($(\text{HAla-Ala})_2[\text{HPW}_{12}\text{O}_{40}] \cdot 4\text{H}_2\text{O}$) was synthesized by dissolving 0.01 mmol PW in 5 mL 0.1 M HCl, and 0.03 mmol Ala-Ala in 5 mL 0.1 M HCl. The peptide solution was added to the PW solution and left to evaporate.

17 ($(\text{HAla})\text{H}_3[\text{PW}_{12}\text{O}_{40}]_2 \cdot 4\text{H}_2\text{O}$) was synthesized by dissolving 0.01 mmol PW in 5 mL 0.5 M HCl, and 0.03 mmol trialanine in 5 mL 0.5 M HCl. The peptide solution was added to the PW solution and left to evaporate.

18 ($(\text{HGly})_3)_4[\text{SiW}_{12}\text{O}_{40}] \cdot 2\text{H}_2\text{O}$) was synthesized by dissolving 0.01 mmol SiW in 5 mL 0.1 M HCl, and 0.03 mmol triglycine in 5 mL 0.1 M HCl. The SiW solution was added to the triglycine solution, and left to evaporate.

19 ((HEPES)₃(H₃O)SiW₁₂O₄₀·H₂O) was synthesized by freezing 5 mL of HEPES buffer (100 mM, pH 7) in liquid nitrogen, then adding on top a solution of 3 mmol diglycine and 1 mmol SiW and freezing it as well. The tube was wrapped in insulation foil and left in a Dewar to thaw slowly. Crystals formed by reverse flow crystallization as the two solutions thawed and mixed.

Zirconium phosphate (ZrP) was synthesized by adding 0.03 grams of zirconium chloride octahydrate in 2 mL water. To this was added 5 mL 0.1 M phosphate buffer (pH 7.4), upon which white precipitate formed.

PW microspheres were synthesized by dissolving 1 mmol potassium titanium oxide oxalate hydrate in 30 mL 2 M HCl, then adding 1 mmol phosphotungstic acid. The solution was heated to >90°C and evaporated until 10 mL remained. The precipitate was washed via pelleting by centrifugation and replacing the supernatant with water, repeated three times. The washed precipitate was then dried in a Petri dish.

2.2 Characterization

2.2.1 Crystals

The general workflow once crystals formed was to screen them in SEM/EDS to verify crystal morphology and that the correct elements were present in approximately correct ratios. If these factors were acceptable, a crystal was selected to run X-ray diffraction, and the structure was solved. In some cases, FT-IR, NMR, TGA or MS were used to obtain complementary data.

2.2.2 Other material

Non-single-crystal material was analysed in SEM/EDS to determine morphology and elemental composition. Powder X-ray (XRPD) was used to determine the composition, and for the two products detailed here, ZrP microcrystals and PWTi microspheres, the catalytic capabilities were determined. For PWTi microspheres, AFM and TEM were performed for additional morphological data. TEM was performed by collaborators from the Department of Forest Biomaterials and Technology, Swedish University of Agricultural Sciences, Uppsala, Sweden.

2.3 Catalysis

Some of the non-crystal materials showed catalytic abilities. These powders were tested for potential applications.

2.3.1 Peptide bond degradation

To test the ability of ZrP particles to degrade peptide bonds, a mixture of 30 μL ZrP suspension (used as prepared), 30 μL phosphate buffer (0.1 M, pH 7), and 600 μL D_2O , with 6 mM DSS-d6 as a reference and 12 mM Gly-Gly to be split into Gly. In the control, the ZrP suspension was replaced with additional phosphate buffer. The samples were incubated first at 37°C for one week to determine whether peptide bond hydrolysis took place, then for 30 days to study the kinetics, with daily readings of ^1H NMR for the first week, and every other day for the remainder of the experiment.

2.3.2 Electrocatalysis

PW microspheres were tested as an electrocatalyst for the oxygen evolution reaction (OER) at pH 0 in 0.5 M H_2SO_4 , pH 3 in citric acid/sodium citrate buffer, and at pH 7 in phosphate buffer. A three-electrode setup was used; a catalyst-loaded graphite electrode, a platinum mesh as a counter electrode, and Ag/AgCl as a counter electrode. Cyclic voltammetry (CV), linear sweep voltammetry (LSV), and chronoamperometry (CA) were performed. For cyclability, 200 cycles of CV were performed, and the working electrode saturated 20-30 cycles of activation. The iR drop was directly compensated for by the potentiostat (with 82% compensation). The potentials recorded were finally calibrated in relation to the reversible hydrogen electrode (E_{RHE}) by using the equation: $E_{\text{RHE}} = E_{\text{Ag/AgCl}} + 0.059 \times \text{pH}$. To minimize the capacitive current, the scan rate for the LSV curve was 10 mV/s. The overpotential (η) of HER (hydrogen evolution reaction) was calculated by using the equation: $\eta = E_{\text{RHE}} - 1.23$, after reduction of the redox potential of oxygen, $E_{\text{O}_2/\text{O}_2^-} = 1.23$. The Tafel plots were obtained by transforming the LSV curve into $\log(j)$ vs E . The faradaic efficacy was evaluated via control of the gas evolution. The electrocatalytic studies were performed by collaborators at the Department of Materials and Environmental Chemistry, Stockholm University, Sweden.

3. Results and discussion

The main results of this project were a series of X-ray single crystal structures (**1-19**), as summarized in Table 1, as well as two powder materials with notable catalytic properties. In this section, each compound will be described in turn, including structural analysis and additional characterization where such were performed, followed by a brief comparative summary.

Table 1. An overview of the structures produced in this project.

Nr	Publication	Formula	CCDC code
1	I	(HGly ₃) ₃ [PMo ₁₂ O ₄₀]·5H ₂ O	OJIWIQ, 2031299
2	I	(HGly ₃) ₃ [PW ₁₂ O ₄₀]·8H ₂ O	OJIWUQ, 2031301
3	I	(HGly ₄) ₂ (H ₃ O)[PMo ₁₂ O ₄₀]·9H ₂ O	OJIWOW, 2031300
4	I	(HGly ₄) _{1.33} (H ₃ O) _{1.67} [PW ₁₂ O ₄₀]·H ₂ O	OJIXAJ, 2031302
5	II	(HGly-Gly) ₃ [PMo ₁₂ O ₄₀]·4H ₂ O	YEKDAX, 2151361
6	II	(HGly-Gly) ₃ [PMo ₁₂ O ₄₀]·3H ₂ O	YEKCUQ, 2151360
7	II	Na(HGly-Gly) ₂ [PMo ₁₂ O ₄₀]·8H ₂ O	YEKDOL, 2151364
8	II	Na(HGly-Gly) ₂ [PMo ₁₂ O ₄₀]·8H ₂ O	YEKDOL01, 2156667
9	II	Na(HGly-Gly) ₂ (H ₃ O) ₃ [PMo ₁₂ O ₄₀] ₂ ·3H ₂ O	YEKDIF, 2151363
10	II	Na(HGly-Gly)(H ₃ O)[PMo ₁₂ O ₄₀]·3H ₂ O	YEKDEB, 2151362
11	III	[La(H ₂ O) ₉](H ₃ O) ₃ [PW ₁₂ O ₄₀] ₂ ·19H ₂ O	2307589
12	IV	(H ₃ O) ₂ (HPhe-Ala) ₄ [PW ₁₂ O ₄₀] ₂ ·11H ₂ O	FOTZEX, 2362067
13	IV	(HAla-Phe) ₂ [HPW ₁₂ O ₄₀]·4H ₂ O	FOTZIB, 2362068
14	IV	(HAla-Phe) ₃ [PW ₁₂ O ₄₀]	FOTZOH, 2362069
15	IV	(HTyr) ₂ [HPW ₁₂ O ₄₀]·4H ₂ O	FOVBEB, 2362072
16	IV	(HAla-Ala) ₂ [HPW ₁₂ O ₄₀]·4H ₂ O	FOTZUN, 2362070
17	IV	(HAla) ₅ [PW ₁₂ O ₄₀] ₂ ·4H ₂ O	FOVBAX, 2362071
18	V	(HGly ₃) ₄ [SiW ₁₂ O ₄₀]·2H ₂ O	N/A*
19	V	(HEPES) ₃ (H ₃ O)[SiW ₁₂ O ₄₀]·H ₂ O	N/A*

*Not submitted at the time of writing

3.1 M-O bond and hydrophobicity of ligands

These structures show in what way the metal in an NP can affect how ligands bind, even if they bind the oxygen at the surface, and how the hydrophobicity of the ligand can affect the nature of the bonds.

3.1.1 Structure Nr 1 - $(\text{HGly}_3)_3[\text{PMo}_{12}\text{O}_{40}] \cdot 5\text{H}_2\text{O}$

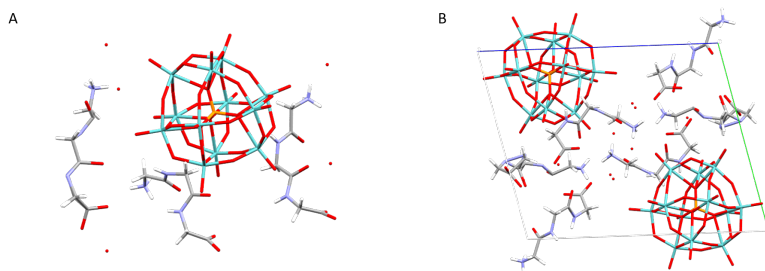


Figure 11. Structure **1** shown as molecular arrangement (A) and packing motif (B).

Structure **1** contains one PMo, three triglycine molecules and five water molecules in an asymmetric unit (Fig. 11), $Z = 2$, in a triclinic P-1 Space group (Table 2). The POMs appear to lie in a hexagonal dense packing with peptides filling the gaps. The contacts between POMs and peptides are mainly electrostatic interactions, with distances near or exceeding 3 Å between POM surface oxygen and low-charge peptide atoms.

MS of the complex at low concentration (50 μM) showed signals corresponding to singlets and doubles of triglycine, as well as PMo with various lacunary species (Fig. 12A). EDS (Fig. 12B) showed the expected elements; molybdenum, phosphorus, oxygen, carbon and nitrogen. FTIR (Fig. 12C) showed signals expected for PMo (Bamoharram 2009; Rominger et al. 2019) and diglycine (Fischer et al. 2005; M. Marsh et al. 2015). ³¹P NMR (Fig. 12D) of **1** in D₂O acidified with HCl showed that PMo was intact.

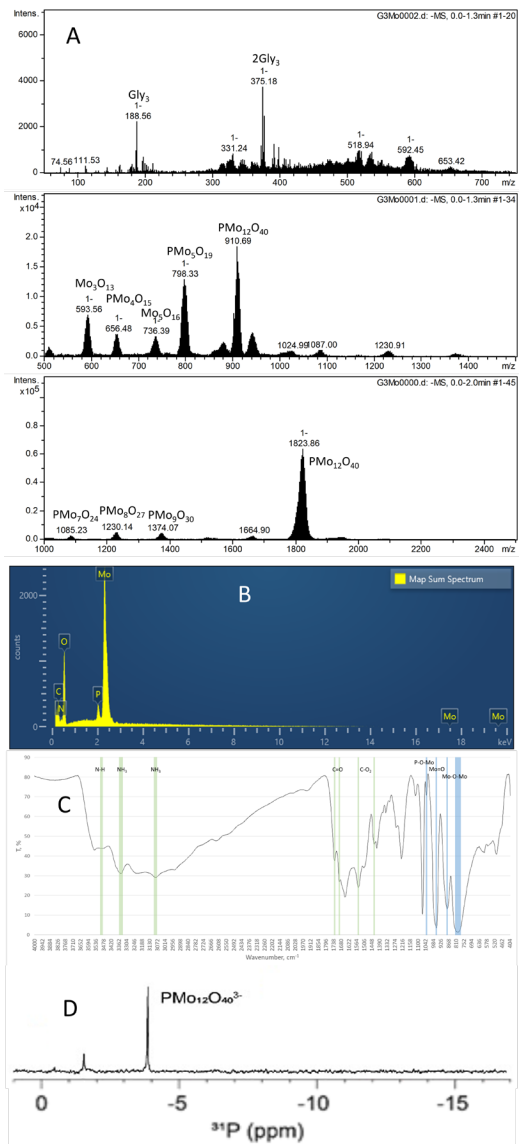


Figure 12. Data for compound 1. A: MS spectra. B: EDS spectrum. C: FT-IR spectrum. D: ³¹P NMR spectrum.

3.1.2 Structure Nr 2 - (HGly)₃[PW₁₂O₄₀] \cdot 8H₂O

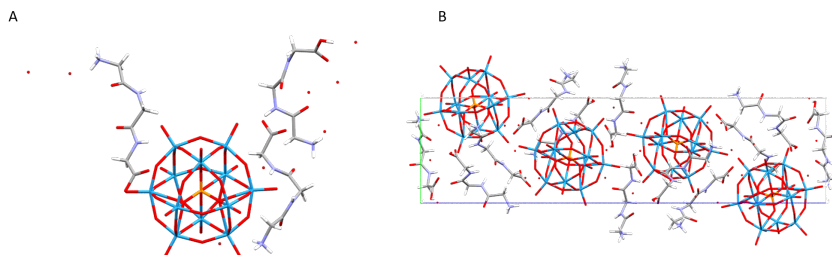


Figure 13. Structure **2** shown as molecular arrangement (A) and packing motif (B).

Structure **2** contains one PW, three triglycine molecules and eight water molecules in an asymmetric unit (Fig. 13), $Z = 4$, in a monoclinic spacegroup $P2_1/n$ (Table 3). While the arrangement of peptides resemble that in **1**, the interactions with the POM tend more toward H-bonding between POM oxygen and acid/base groups on the peptide.

MS of the complex at low concentration (50 μ M) showed signals corresponding to triglycine and aggregated pairs and triplets of triglycine, as well as PW with various lacunary species (Fig. 14A). EDS (Fig. 14B) showed the expected elements; tungsten, phosphorus, oxygen, carbon and nitrogen. FTIR (Fig. 14C) showed signals expected for PW (Bamoharram 2009; Rominger et al. 2019) and diglycine (Fischer et al. 2005; M. Marsh et al. 2015). ³¹P NMR (Fig. 14D) of **2** in D₂O acidified with HCl showed that PW was intact.

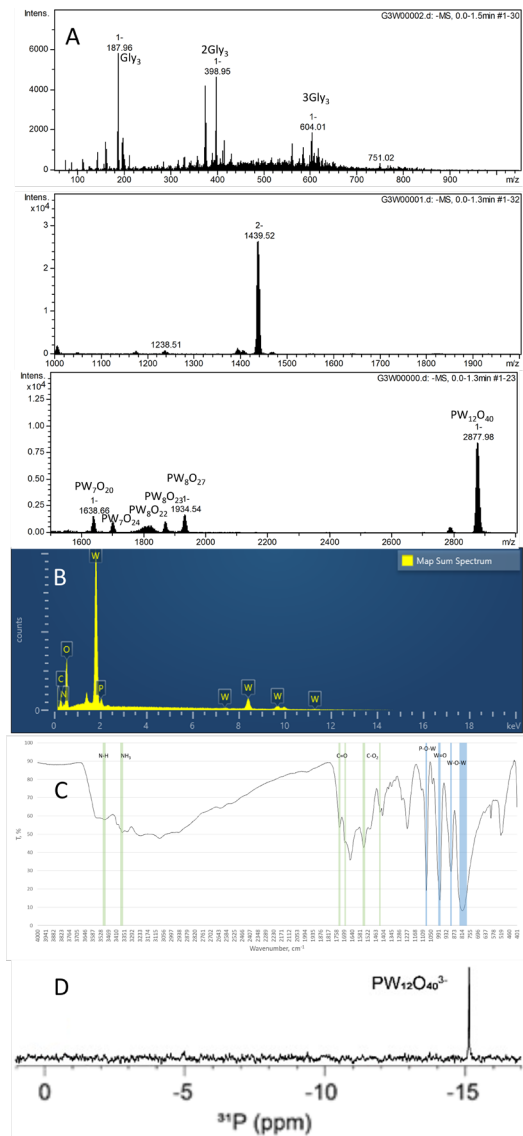


Figure 14. Data for compound **2**. A: MS spectra. B: EDS spectrum. C: FT-IR spectrum. D: ³¹P NMR spectrum.

3.1.3 Structure Nr 3 - $(\text{HGly}_4)_2(\text{H}_3\text{O})[\text{PMo}_{12}\text{O}_{40}] \cdot 9\text{H}_2\text{O}$

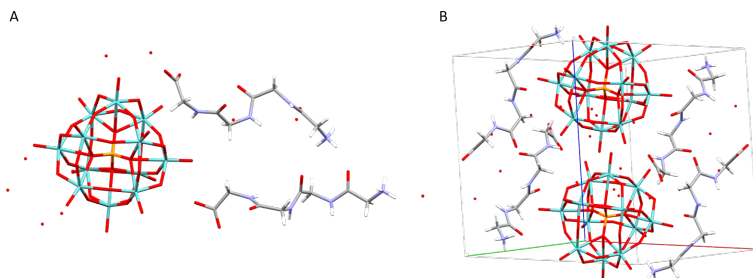


Figure 15. Structure **3** shown as molecular arrangement (A) and packing motif (B).

Structure **3** contains one PMo, two tetraglycine molecules and ten water molecules in an asymmetric unit (Fig. 15), $Z = 2$, arranged in a triclinic Space group, P-1 (Table 4). The peptides stretch out from the POM, like a tail, and make contact with POMs at both ends. Similar to **1**, there are electrostatic interactions between POM and peptide (Fig. 16).

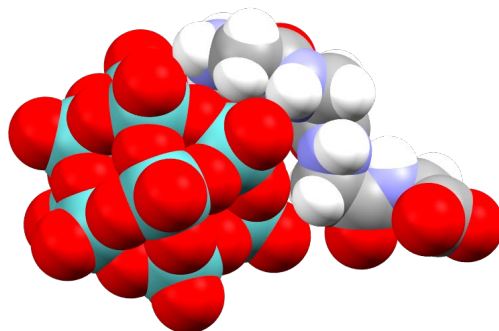


Figure 16. Part of structure **3**, showing close contacts between PMo and tetraglycine even in groups with low charge.

MS of the complex at low concentration (50 μM) showed signals corresponding to singlets and doubles of tetraglycine, as well as PMo with various lacunary species (Fig. 17A). EDS (Fig. 17B) showed the expected elements; Molybdenum, phosphorus, oxygen, carbon and nitrogen. FTIR (Fig. 17C) showed signals expected for PW (Bamoharram 2009; Rominger et al. 2019) and diglycine (Fischer et al. 2005; M. Marsh et al. 2015). ^{31}P NMR (Fig. 17D) of **3** in D_2O acidified with HCl showed that PMO was intact.

MS-spectra were taken at four time points spread over one hour (Fig. 18A). The intensity changed over time, with larger PW fragments gaining intensity, and smaller ones declining in intensity (Fig. 18B). For a control of only PMo with no tetraglycine, the corresponding signals declined uniformly (Fig. 18C). This suggests that tetraglycine has a stabilizing effect on POMs.

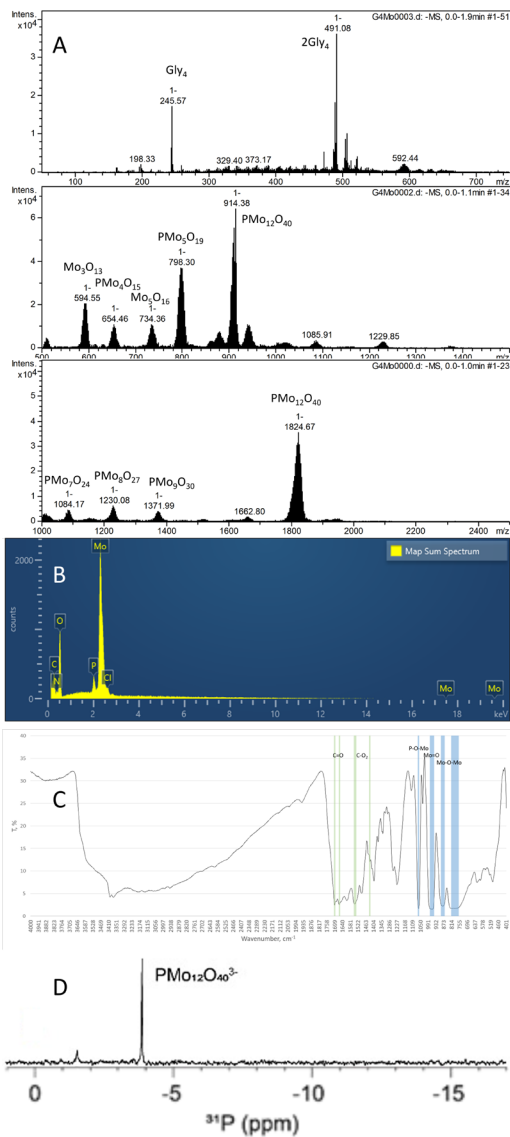


Figure 17. Data for compound **3**. A: MS spectra. B: EDS spectrum. C: FT-IR spectrum. D: ³¹P NMR spectrum.

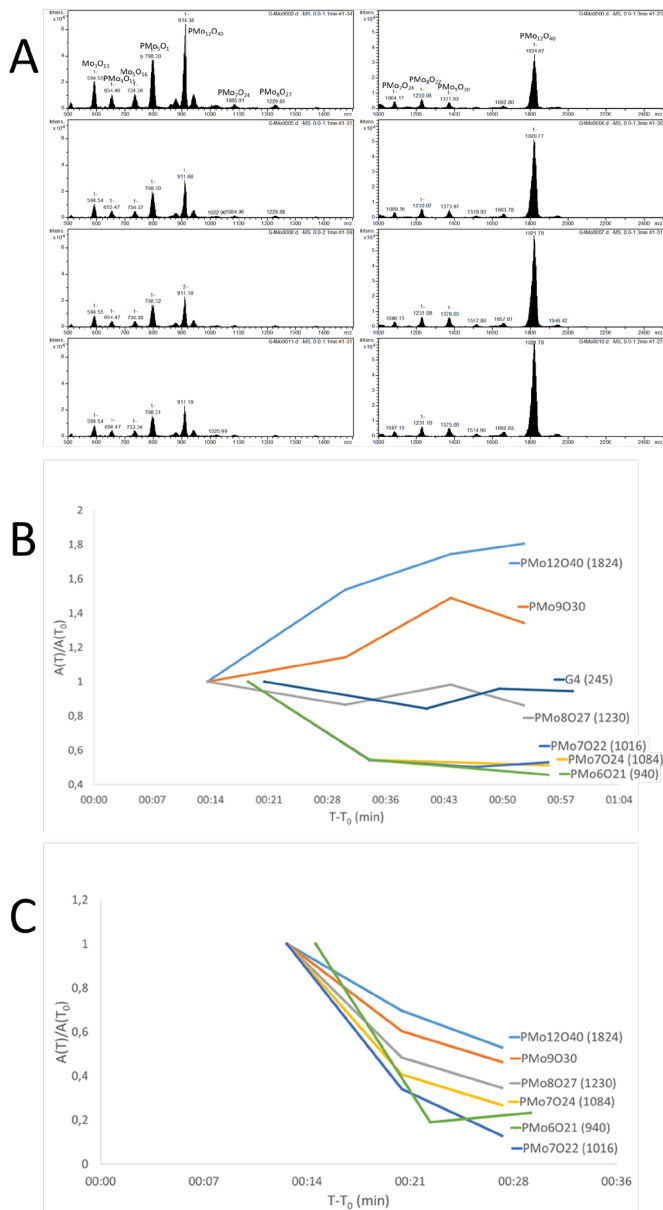


Figure 18. MS spectra of **3** at four time points after dissolution (A). Area of signals plotted against time for **3** (B) and control without peptide (C).

3.1.4 Structure Nr 4 - $(\text{HGly}_4)_{1.33}(\text{H}_3\text{O})_{1.67}[\text{PW}_{12}\text{O}_{40}] \cdot \text{H}_2\text{O}$

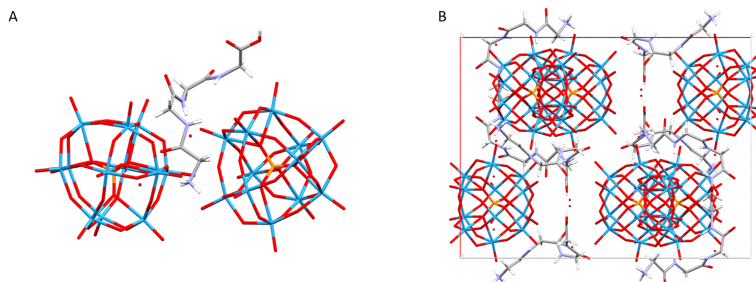


Figure 19. Structure 4 shown as molecular arrangement (A) and packing motif (B).

Structure 4 consists of tetraglycine and PW in a 4:3 ratio, three water molecule and five oxonium ions (Fig. 19), in a tetragonal Space group $P4_2/n$ (Table 5). It is somewhat denser than 3, and the peptide is wrapped around the POM rather than stretching out from it. Carbonyl groups also form double H-bonds between peptides. The arrangement of POMs resembles hexagonal close packing, with peptides filling the gaps (Fig. 20)

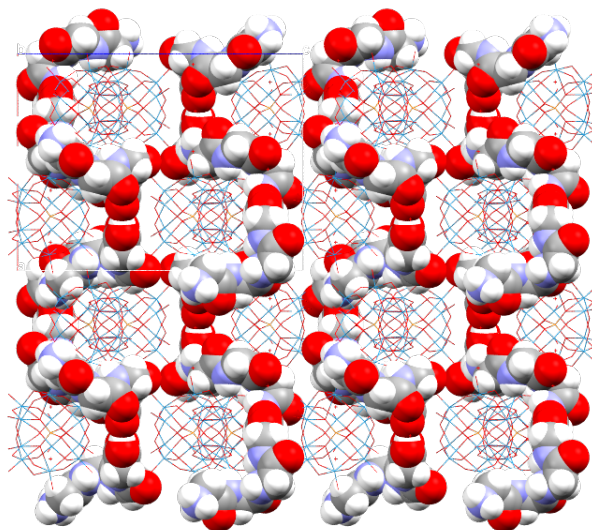


Figure 20. Expanded packing motif of 4, showing how tetraglycine surrounds PW and fills the gaps between the particles.

MS of the complex at low concentration (50 μM) showed signals corresponding to singlets and doubles of tetraglycine, as well as PW with various lacunary species (Fig. 21A). EDS (Fig. 21B) showed the expected elements; tungsten, phosphorus, oxygen, carbon and nitrogen. FTIR (Fig. 21C) showed signals expected for PW (Bamoharram 2009; Rominger et al. 2019) and diglycine (Fischer et al. 2005; M. Marsh et al. 2015). ^{31}P NMR (Fig. 21D) of **4** in D_2O acidified with HCl showed that PW was intact.

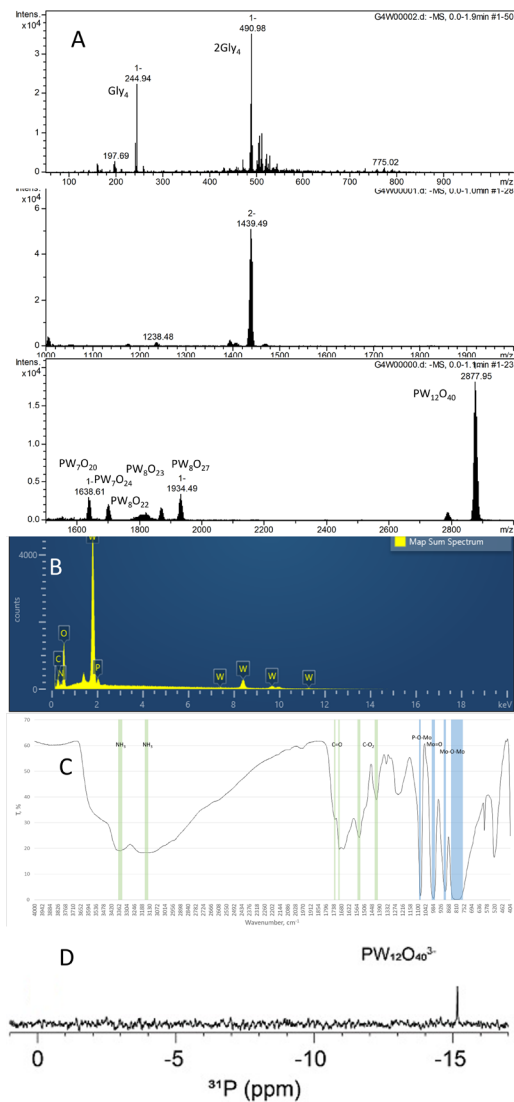


Figure 21. Data for compound 4. A: MS spectra. B: EDS spectrum. C: FT-IR spectrum. D: ³¹P NMR spectrum.

3.1.5 Discussion

Complexes of PW and PMo with triglycine and tetraglycine show the differences the metal and chain length can make. Because molybdenum is more electronegative than tungsten, the Mo-O bond will be less polar than W-O, allowing for electrostatic interactions, while the PW will favour H-bonding. The peptide chain length also affects the bonding, as the triglycine complexes look similar, while the tetraglycine complexes are very different, with differing POM/peptide ratio and arrangement of the peptide. The MS experiments were done at a low enough concentration that POM in complex with diglycine and no ligand would degrade (Rominger et al. 2019). The POM appeared somewhat stable, suggesting that longer peptide chains have a stabilizing effect on POMs.

The number of H-bonds per POM differ slightly; **1** and **3** have 18, **2** has 20, and **4** has 2.66 per POM unit (normalized through the formula $[nr\ of\ unique\ bonds\ x\ Z] / [nr\ of\ POMs\ in\ a\ unit\ cell]$). This, along with the tight wrapping of the peptide in **4**, implies that it favours electrostatic interactions more than the other structures.

3.2 pH and salinity

Changing the conditions of crystallization can affect how a crystal forms. Even if the crystal itself contains the same compounds, factors such as temperature, pH and salinity can change how they are put together

3.2.1 Structure Nr 5 - (HGly-Gly)₃[PMo₁₂O₄₀]·4H₂O

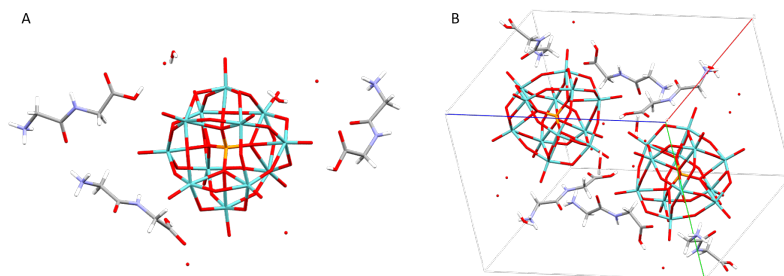


Figure 22. Structure **5** shown as molecular arrangement (A) and packing motif (B).

Structure **5** contains one PMo, three diglycine molecules and seven water molecules in an asymmetric unit (Fig. 22), $Z = 2$, contained in a triclinic Space group P-1 (Table 6). The contacts between POM and peptide are mainly H-bonding, with some electrostatic interactions visible.

MS-spectra were taken of **5** dissolved in 0.2 M HCl, water and phosphate buffer (Fig. 23). PMo was more intact in the acidic solution, and nearly completely degraded in the buffer. The stabilizing effect of oligopeptides touched on in 3.1.3 appears more potent for longer chains.

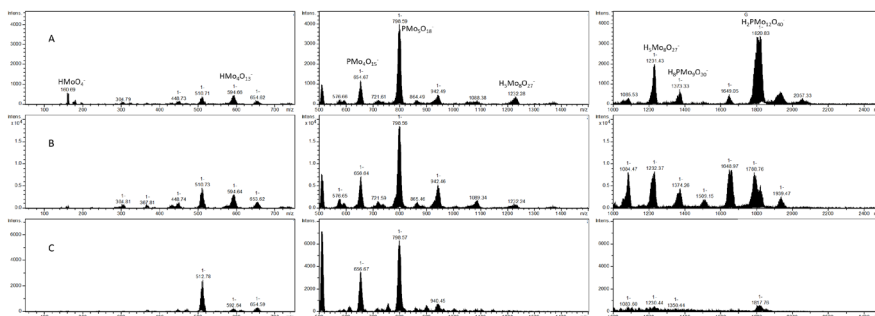


Figure 23. MS of **5** dissolved in (A) 0.2 M HCl, (B) water, and (C) 5 mM phosphate buffer, pH 6.5.

EDS (Fig. 24A) showed the expected elements; molybdenum, phosphorus, oxygen and small amounts of nitrogen. Carbon was excluded due to the carbon tape the sample was mounted on contaminating the ratios. TGA (Fig. 24B) showed a stepwise decline in mass, starting with loss of water, then a stepwise decomposition of organics, finishing at 500°C. FT-IR

(Fig. 24C) showed the typical bonds from PMo and diglycine (Fischer et al. 2005; Bamoharram 2009).

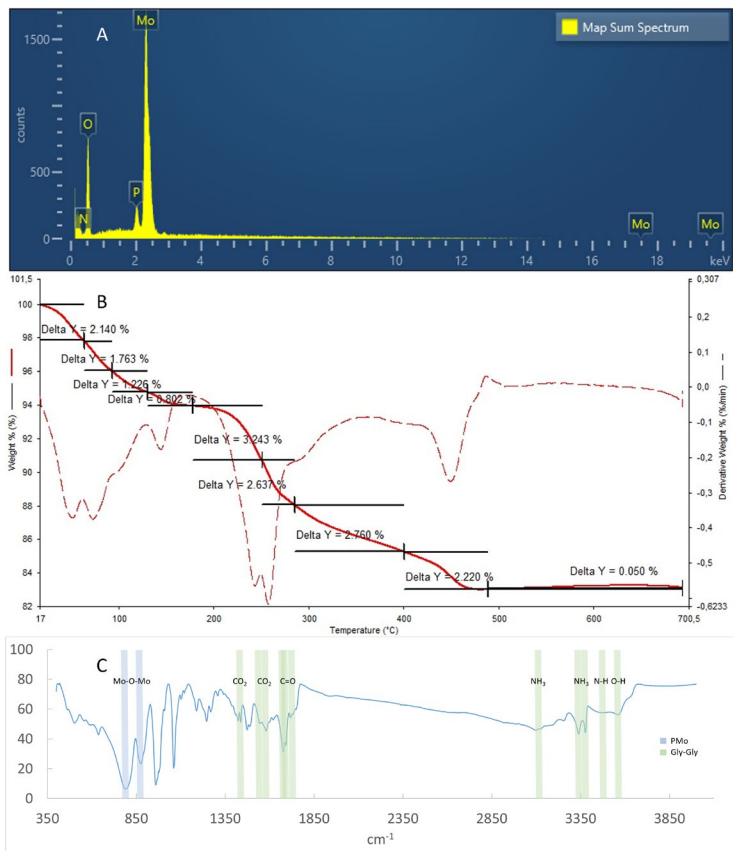


Figure 24. Data for compound 5 Displayed in A: EDS, B: TGA, C: FT-IR

3.2.2 Structure Nr 6 - (HGly-Gly)₃[PMo₁₂O₄₀] \cdot 3H₂O

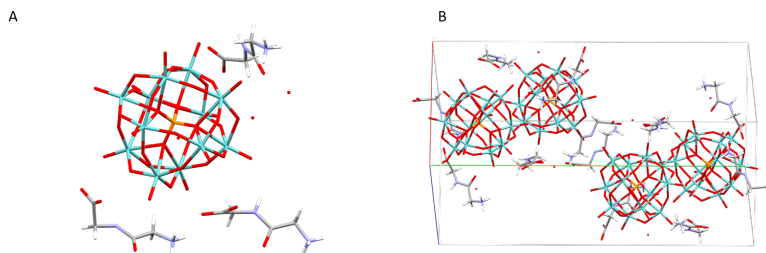


Figure 25. Structure **6** shown as molecular arrangement (A) and packing motif (B).

Structure **6** contains one PMo, three diglycine molecules and three water molecules in the asymmetric unit (Fig. 25), $Z = 4$, with a monoclinic Space group $P2_1/n$ (Table 7). It was produced similarly to **5**, but with an additional step of heating the solution prior to crystallization. The contacts between POM and peptide are also H-bonding with some electrostatic contacts, though the peptides lie more flat against the POM than in **5**. TGA (Fig. 26A) showed a stepwise decline in mass, starting with loss of water, then a stepwise decomposition of organics, finishing at 500°C. FT-IR (Fig. 26B) showed the typical bonds from PMo and diglycine (Fischer et al. 2005; Bamoharram 2009).

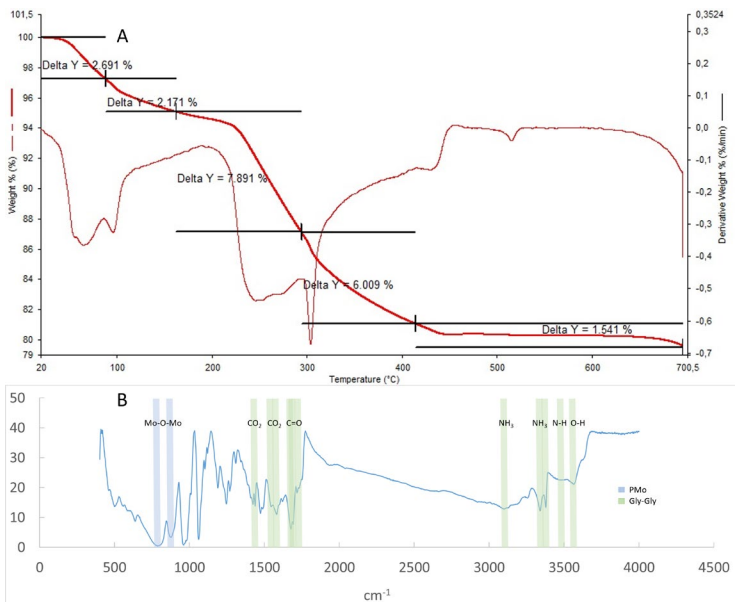


Figure 26. Data for compound **6** Displayed in A: TGA, B: FT-IR

3.2.3 Structure Nr 7 - Na(HGly-Gly)₂[PMo₁₂O₄₀]·8H₂O

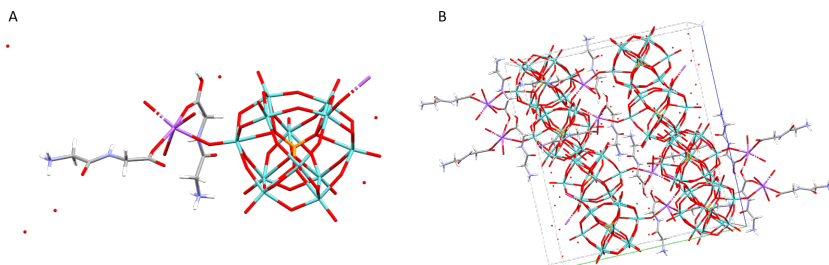


Figure 27. Structure **7** shown as molecular arrangement (A) and packing motif (B).

Structure 7 contains one PMo, two diglycine molecules, eight water molecules, and one sodium ion in an asymmetric unit (Fig. 27), $Z = 8$, with an orthorhombic Space group $Pbca$ (Table 8). The only direct contact between POM and peptide in this structure is with an amine group. The others are indirect, via either water or sodium. Sodium also bridges contacts between POM particles (Fig. 28), likely shielding the anions' charge.

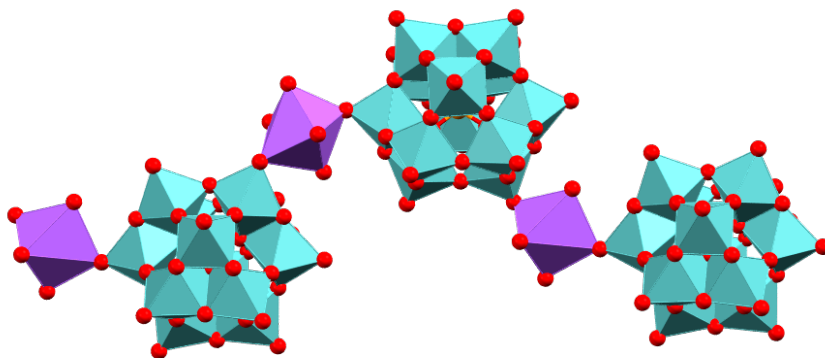


Figure 28. PMo anions/particles bridged by sodium ions.

EDS (Fig. 29A) showed the expected elements; molybdenum, phosphorus, oxygen, nitrogen and chlorine. Carbon was excluded due to the carbon tape the sample was mounted on contributing to the ratios. TGA (Fig. 29B) showed a stepwise decline in mass, starting with loss of water, then a stepwise decomposition of organics, finishing at 500°C. FT-IR (Fig. 29C) showed the typical bonds from PMo and diglycine (Fischer et al. 2005; Bamoharram 2009).

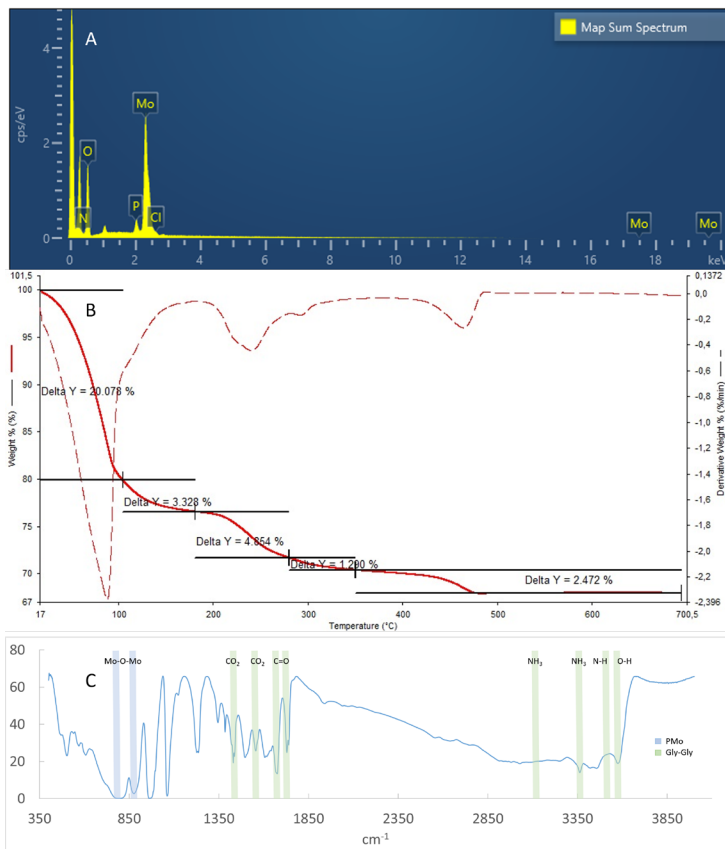


Figure 29. Data for compound 7 displayed in A: EDS, B: TGA, C: FT-IR

3.2.4 Structure Nr 8 - $\text{Na}(\text{HGly-Gly})_2[\text{PMo}_{12}\text{O}_{40}]\cdot 8\text{H}_2\text{O}$

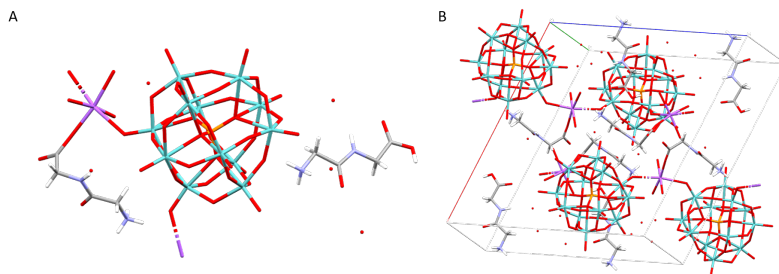


Figure 30. Structure **8** shown as molecular arrangement (A) and packing motif (B).

Structure **8** contains one PMo , two diglycine molecules, eight water molecules and one sodium ion in an asymmetric unit (Fig. 30), $Z = 4$, with a monoclinic Space group $\text{P2}_1/\text{c}$ (Table 9). Similar to **7**, it has few direct contacts between POM and peptide, instead having indirect contacts via water and sodium. Here too are sodium ions acting as bridges between POM anions. EDS (Fig. 31) showed the expected elements; molybdenum, phosphorus, oxygen, nitrogen and trace amounts of titanium. Carbon was excluded due to the carbon tape the sample was mounted on contaminating the ratios. TGA and FTIR were not run on this compound due to insufficient material.

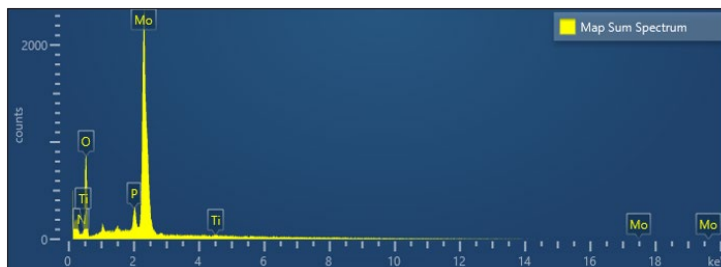


Figure 31. EDS spectrum for compound **8**.

3.2.5 Structure Nr 9 - $\text{Na}(\text{HGly-Gly})_2(\text{H}_3\text{O})_3[\text{PMo}_{12}\text{O}_{40}]_2 \cdot 3\text{H}_2\text{O}$

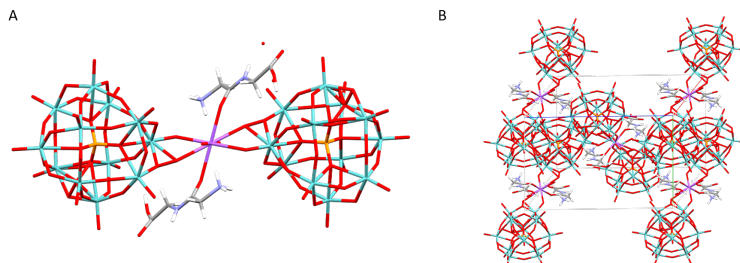


Figure 32. Structure **9** shown as molecular arrangement (A) and packing motif (B).

Structure **9** contains one PMo, one diglycine molecule, three water molecules, and one half sodium ion per asymmetric unit (Fig. 32), $Z = 4$ with a monoclinic Space group $P2_1/c$ (Table 10). The sodium ion is wedged between two PMo and two diglycine carbonyl groups, likely driving the formation of this particular arrangement. The two H-bonds between PMo and peptide, at the carboxyl and amine groups, are relatively weak at 2.83 and 2.98 Å, supporting that conclusion. TGA (Fig. 33A) showed a stepwise decline in mass, starting with loss of water, then a stepwise decomposition of organics, finishing at 500°C. FT-IR (Fig. 33B) showed the typical bonds from PMo and diglycine (Fischer et al. 2005; Bamoharram 2009), though with the signals corresponding to oxygen/nitrogen – hydrogen bonds too diffuse to make out with certainty.

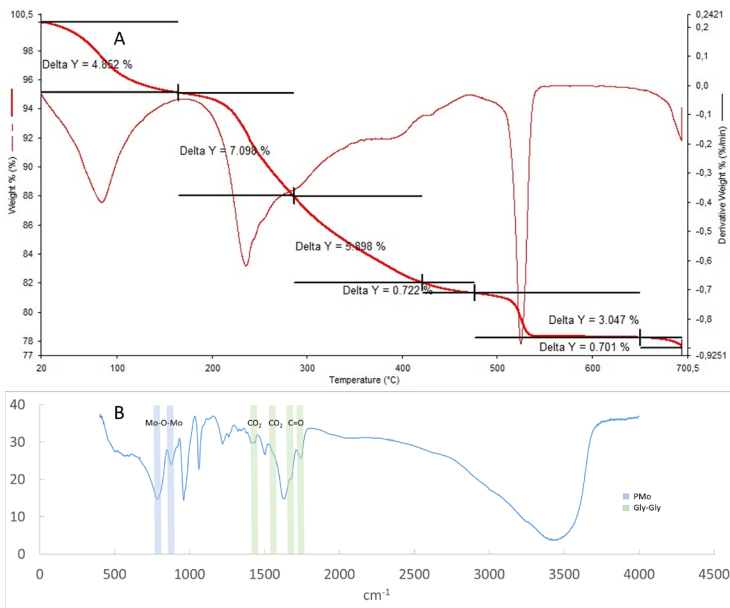


Figure 33. Data for compound **9** displayed in A: TGA, B: FT-IR

3.2.6 Structure Nr 10 - $\text{Na}(\text{HGly-Gly})_2(\text{H}_3\text{O})_3[\text{PMo}_{12}\text{O}_{40}]_2 \cdot 4\text{H}_2\text{O}$

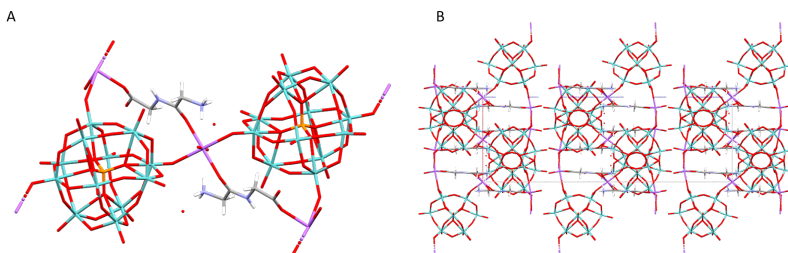


Figure 34. Structure **10** shown as molecular arrangement (A) and packing motif (B).

Structure **10** contains one PMo, one diglycine, two water molecules, one and a half oxonium ions, and one half sodium ion in an asymmetric unit (Fig. 34), $Z = 8$, with an orthorhombic Space group $Pbcn$ (Table 11). The peptide makes contact with two sodium ions, and has no direct contact between PMo and diglycine. Both **9** and **10** contained high amount of sodium in solution,

due to the precursors being sodium salts of molybdate and phosphate. The sodium in solution likely competes with diglycine for space around the POM, which is why **9** and **10** have only one peptide per POM, and to a lesser extent why **7** and **8** have two peptides per POM. EDS (Fig. 35A) showed the expected elements; molybdenum, phosphorus, oxygen and nitrogen. Carbon was excluded due to the carbon tape the sample was mounted on contaminating the ratios. TGA (Fig. 35B) showed a stepwise decline in mass, starting with loss of water, then a stepwise decomposition of organics, finishing at 500°C. FT-IR (Fig. 35C) showed the typical bonds from PMo and diglycine (Fischer et al. 2005; Bamoharram 2009).

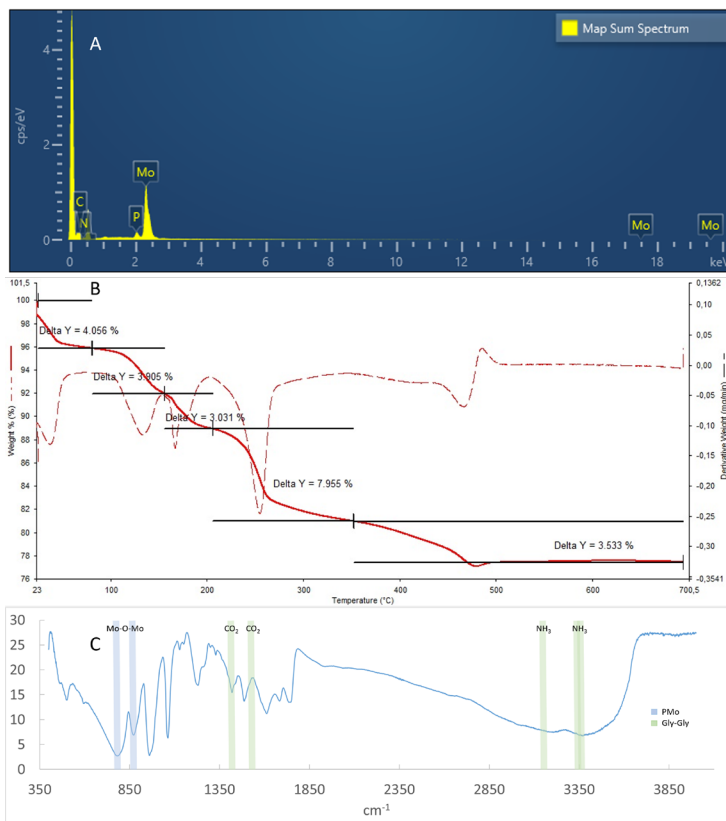


Figure 35. Data for compound **10** displayed in A: EDS, B: TGA, C: FT-IR

3.2.7 Structure Nr 11 - $[\text{La}(\text{H}_2\text{O})_9](\text{H}_3\text{O})_3[\text{PW}_{12}\text{O}_{40}]_2 \cdot 19\text{H}_2\text{O}$

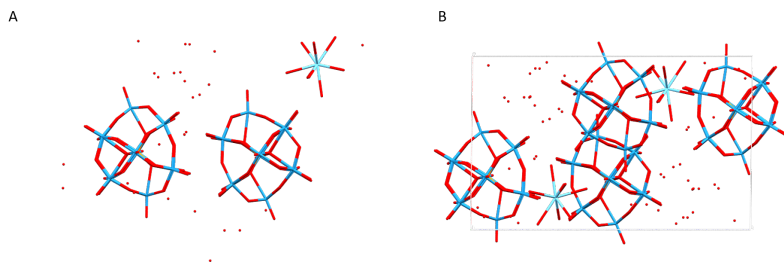


Figure 36. Structure **11** shown as molecular arrangement (A) and packing motif (B).

Structure **11** contains two PW, one lanthanum (III) ion and 31 water molecules in asymmetric unit (Fig. 36), $Z = 2$, with a triclinic Space group P-1 (Table 12). Likely, due to the acidity of the solution, the PW is protonated, and a portion of the water are oxonium ions. This would help shield the charge of the PW ions, allowing them to make close contact despite the lack of bridging metal ions. The La ion is completely hydrated, and does not make direct contact with the POM. Much of the crystal appears to be held together by H-bonded water, which might explain the low stability in air; the water evaporates and the crystal structure is compromised.

3.2.8 Discussion

The diversity of these structures is remarkable, given that the components are identical. Simply heating the solution turned **5** into **6**, with lower water content and rearranged ligands. The increasing amount of sodium and oxonium ions in solution lead to a decrease in the number of ligands binding the POM (Fig. 37). Likely, there is competition for space on the POM surface, and given increasing excess of rivals, the peptide loses hold of its spot.

The Na-containing structures, **7-10**, are interesting for another reason, as they can be used as a model for purification of proteins by salt precipitation (Duong-Ly & Gabelli 2014).

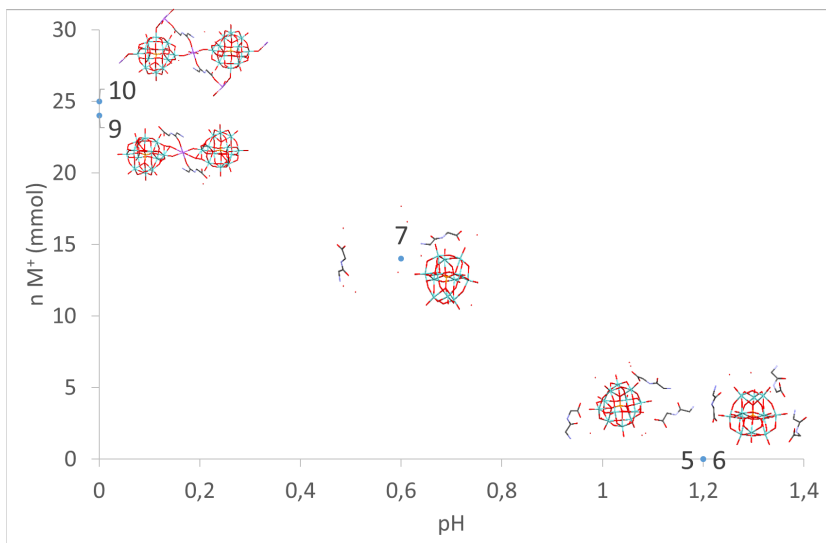


Figure 37. pH and salinity plotted for structures in publication II.

3.3 Structure determining peptides

The previous sections dealt with complexes of oligoglycines. Here, different amino acids are used, namely alanine (Ala), phenylalanine (Phe) and tyrosine (Tyr). This has shifted the driving force from the POM to the peptides, as the Tyr and Phe side chains are capable of π -stacking, the driving force behind e.g. DNA structure, and a major force behind protein folding.

3.3.1 Structure Nr 12 - $(\text{H}_3\text{O})_2(\text{HPhe-Ala})_4[\text{PW}_{12}\text{O}_{40}]_2 \cdot 11\text{H}_2\text{O}$

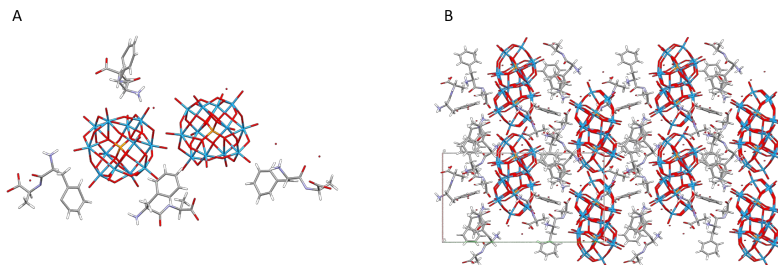


Figure 38. Structure **12** shown as molecular arrangement (A) and packing motif (B).

Structure 12 contains two PW, four Phe-Ala molecules, and twelve water molecules in an asymmetric unit (Fig. 38), $Z = 4$, with a monoclinic Space group $P2_1$ (Table 13). The POM and peptide are arranged in distinct layers, with the Phe side chains arranged in four-member π -stacked chains (Fig. 39).

EDs shows expected ratios of tungsten, phosphorus, oxygen, carbon and nitrogen (Fig. 40A). FTIR shows signals consistent with PW and protonated peptides (Fig. 40B).

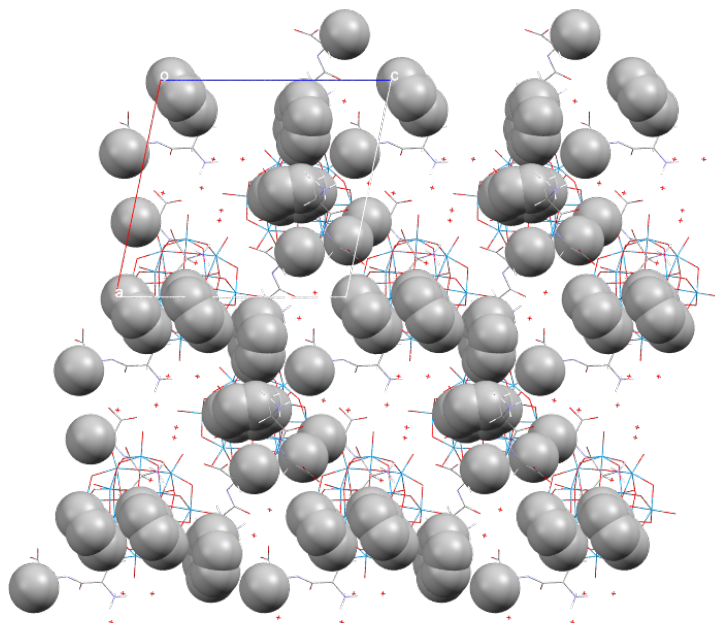


Figure 39. Structure **12** shown as packing motif with hydrophobic groups highlighted.

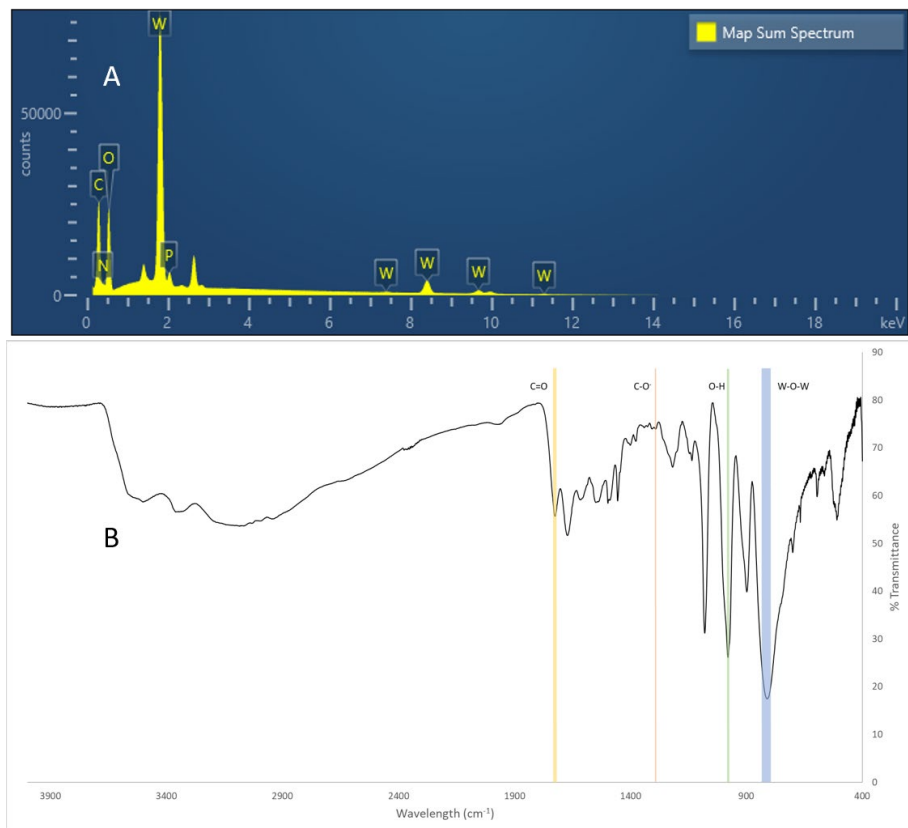


Figure 40. (A) EDS spectrum and (B) FTIR spectrum of **12**.

3.3.2 Structure Nr 13 - (HAla-Phe)₂[HPW₁₂O₄₀]·4H₂O

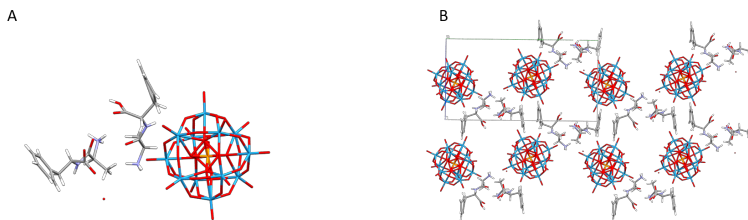


Figure 41. Structure **13** shown as molecular arrangement (A) and packing motif (B).

Structure **13** consists of one PW, two Ala-Phe molecules and four water molecules in an asymmetric unit (Fig. 41), $Z = 2$, with a monoclinic Space group $P2_1$ (Table 14). The peptides form chains of alternating π -stacking and H-bonding groups, while the POMs are arranged in columns (Fig. 42).

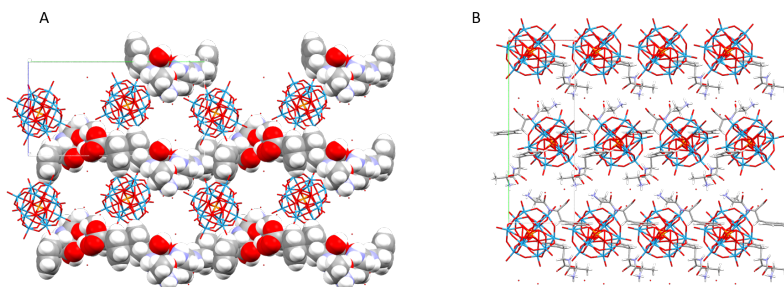


Figure 42. Structure **13** shown packing motif with highlighted (A) peptide chains and (B) POM columns.

3.3.3 Structure Nr 14 - (HAla-Phe)₃[PW₁₂O₄₀]

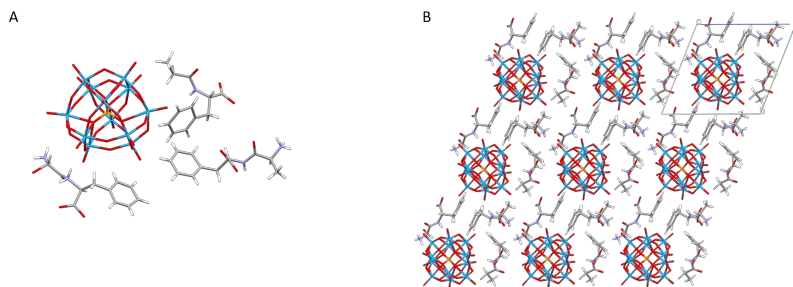


Figure 43. Structure **14** shown as molecular arrangement (A) and packing motif (B).

Structure **14** contains one PW and three Ala-Phe in an asymmetric unit (Fig. 43), $Z = 2$, with a triclinic Space group P1 (Table 15). The POMs are arranged in columns, with a matrix of peptides surrounding them. The peptides are connected by both π -stacking and H-bonding, and the structure is very dense, containing neither water nor voids. Despite containing the same components as **13**, this structure is both denser and more complex in its order. This is likely due to the different time spans used for their crystallizations, and supports the argument of section 3.2; that different conditions can yield different structures from the same components.

EDS showed expected ratios of tungsten, phosphorus, oxygen, carbon and nitrogen (Fig. 44A). FTIR showed signals consistent with protonated peptides (Fig. 44B).

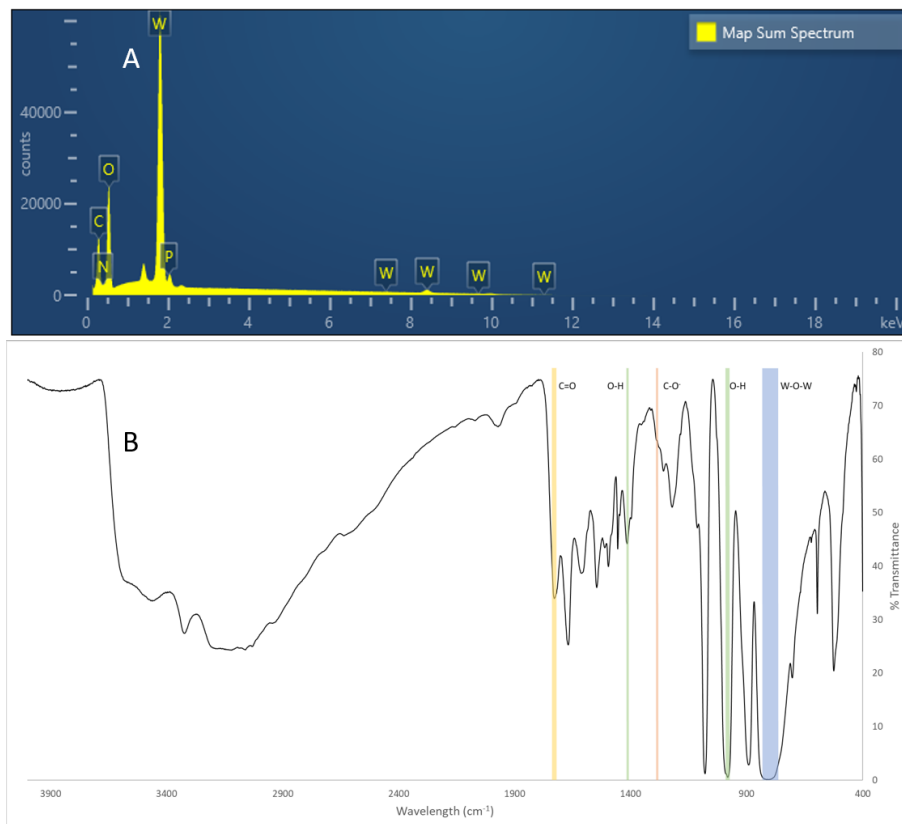


Figure 44. (A) EDS spectrum and (B) FTIR spectrum of **14**.

3.3.4 Structure Nr 15 - (HTyr)₂[HPW₁₂O₄₀] \cdot 4H₂O

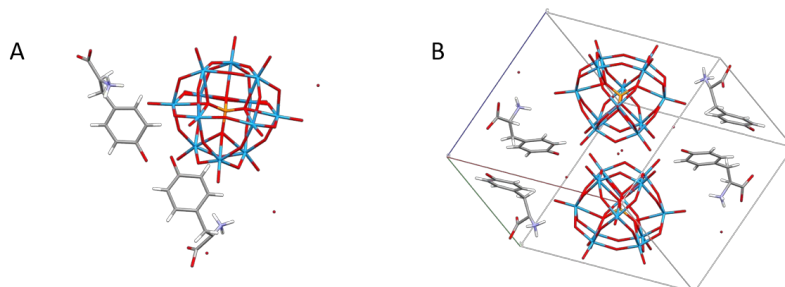


Figure 45. Structure **15** shown as molecular arrangement (A) and packing motif (B).

Structure **15** contains one PW, two tyrosine molecules, and four water molecules in an asymmetric unit (Fig. 45), $Z = 2$, with a triclinic Space group P-1 (Table 16). The amino acids are arranged in long π -stacks with distorted columns of POMs at an angle (Fig. 46). The infinite Tyr stacks are likely possible due to it being an amino acid rather than an oligopeptide, which is why the same motif is not seen in **12-14**, as the steric hindrance prevents it. It is a valuable comparison to the Phe-residues, however, as the Tyr side chain has a carbonyl group available for H-bonding, which is present and appears to stabilize the stacking by binding an adjacent amino group.

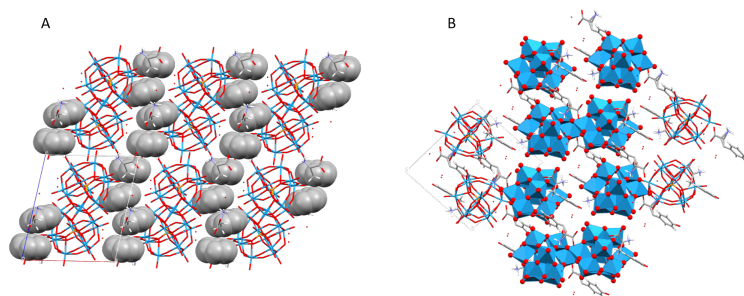


Figure 46. Structure **15** shown as packing motif with (A) stacked tyrosine and (B) PW columns highlighted.

EDS showed expected ratios of tungsten, phosphorus, oxygen, carbon and nitrogen (Fig. 47).

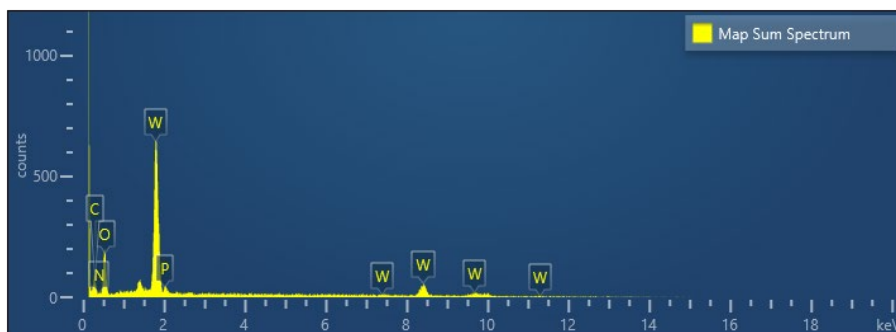


Figure 47. EDS spectrum of **15**.

3.3.5 Structure Nr 16 - $(\text{HAla-Ala})_2[\text{HPW}_{12}\text{O}_{40}]\cdot 4\text{H}_2\text{O}$

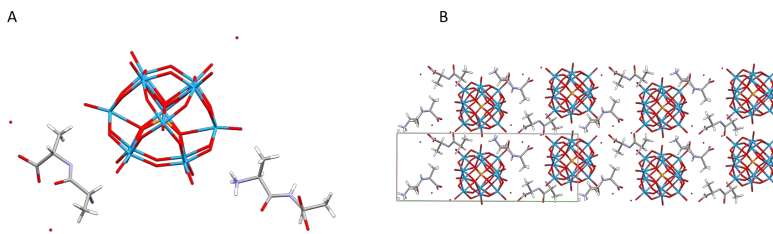


Figure 48. Structure **16** shown as molecular arrangement (A) and packing motif (B).

Structure **16** contains one PW, two Ala-Ala molecules, and four water molecules in an asymmetric unit (Fig. 48), $Z = 2$, in a monoclinic Space group $P2_1$ (Table 17). While there are contacts between Ala side chains, the main interactions are H-bonds, and it appears that the POM is the driving force behind the structure, with the dialanine filling the gaps. In all, **16** has more in common with **1-6** than with **12-15**.

EDS showed expected ratios of tungsten, phosphorus, oxygen, carbon and nitrogen (Fig. 49A). FTIR showed signals consistent with protonated peptides (Fig. 49B).

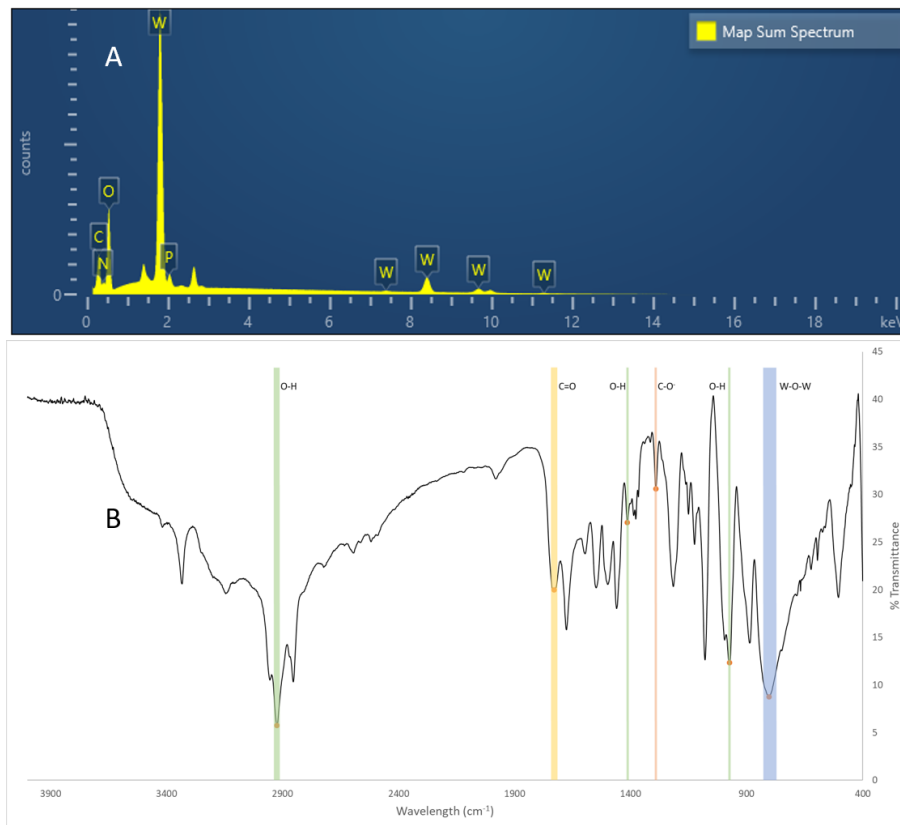


Figure 49. (A) EDS spectrum and (B) FTIR spectrum of **16**.

3.3.6 Structure Nr 17 - $(\text{HAla})\text{H}_5[\text{PW}_{12}\text{O}_{40}]_2 \cdot 4\text{H}_2\text{O}$

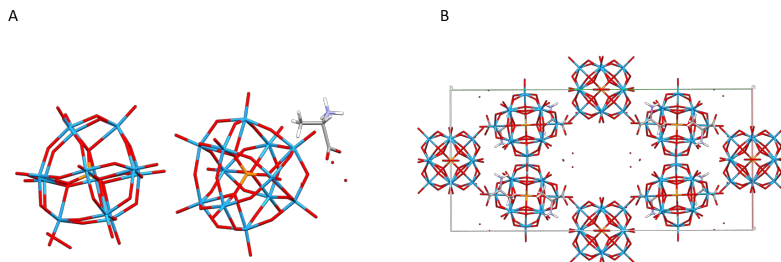


Figure 50. Structure **17** shown as molecular arrangement (A) and packing motif (B).

Structure **17** contains two PW, one alanine molecule, and four water molecules (Fig. 50), $Z = 4$, with an orthorhombic Space group $C222$ (Table 18). The structure contains a relatively small amount of alanine, but the impact is significant, as it strongly resembles a metal-organic framework, a type of porous organic/inorganic hybrid material (Furukawa et al. 2013). The alanine amino group has H-bonds to three POMs, each triad has two amino groups near the center, each POM is a member of two triads, and the alanines are arranged in pairs by hydrophobic interactions at the side chains. The result is a remarkably ordered structure with large voids, approximately 8×12 Å wide channels, shaped like a rhombus with corners at 50° and 130° .

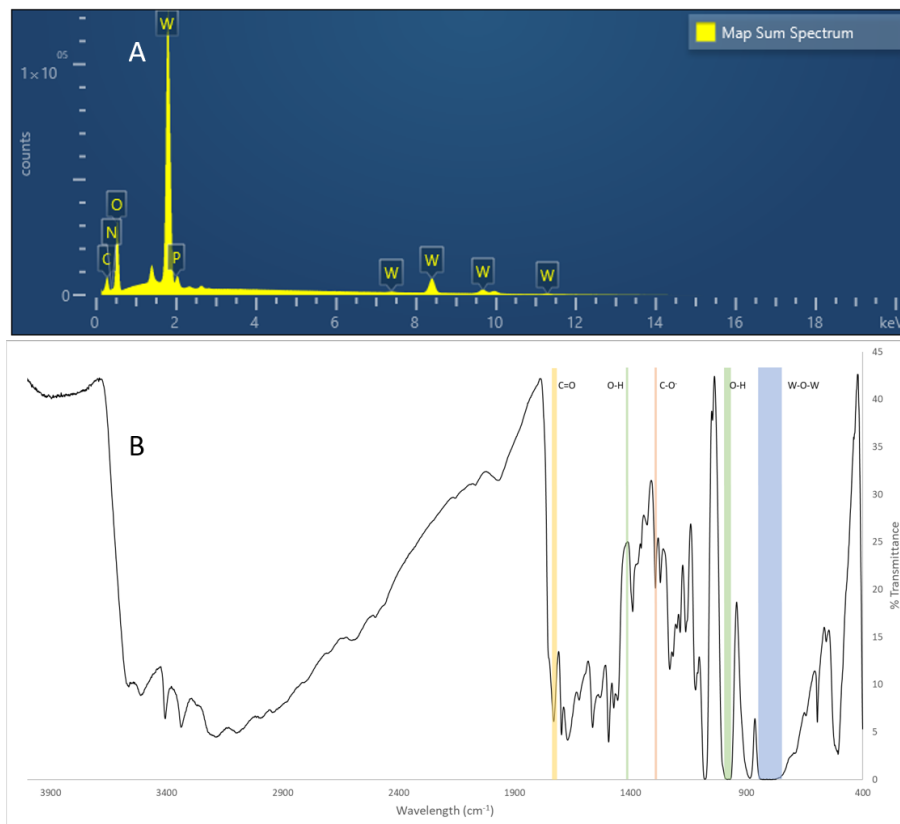


Figure 51. (A) EDS spectrum and (B) FTIR spectrum of **17**.

EDS showed expected ratios of tungsten, phosphorus, oxygen, carbon and nitrogen (Fig. 51A). FTIR showed signals consistent with protonated peptides (Fig. 51B).

3.3.7 Discussion

Structure **13** and **14** contain the same components, but have quite different structures. The reason for this is likely the time they took to form. **13** was quick to form, and is less dense and more “simple” in its structure, while **14** took longer to form and is denser and more complex, with more elaborate π -stacking and a higher dimension in the bonding network. **12** contains the

same amino acids as **13** and **14**, but in reverse order, which has made a significant difference in the structure. **12** has alternating layers of POM and peptide, and four rings involved in π -stacking. It also has far more H-bonds, with 55 unique H-bonds compared to eleven and thirteen for **13** and **14**, respectively. This might be due to the order of amino acids. In **12**, the aromatic ring is adjacent to the amino group, which is smaller than the carboxyl neighbour in **13** and **14**. This makes Phe-Ala more surfactant-like, with a hydrophobic “head” and a hydrophilic “tail,” so there is less steric hindrance for both types of interaction. Similar molecules have been grafted onto POMs to link proteins and form large assemblies (Salazar Marcano et al. 2024), a sort of protein sol-gel.

Comparing these to **15**, the Tyr amino acid lacks much steric hindrance for its ring, so it can form an infinite stack, aided by H-bonding between the carbonyl group on the ring and the amine group. Tyrosine has been shown to be important to the structure of spider silk proteins (Greco et al. 2021).

16 looks much like the structures in section 3.2, but with the addition of some hydrophobic interactions, though it is clear that these are not as powerful as the π -stacking in **12-15**. **17**, on the other hand, has a surprising structure, in that it resembles a metal-organic framework (MOF). MOFs are assemblies of organic molecules linking metal atoms (Furukawa et al. 2013).

3.4 Stabilization at higher pH via complex formation

Silicotungstic acid (SiW) is similar to PMo and PW, but has a silicon atom at the centre instead of a phosphorus atom. It is stable to a higher pH than phosphometallates, and has therefore been used as a control to compare with titanium oxide NPs for interactions with virus particles (publication V). Titanium oxide particles were investigated for their antiviral properties, and a control was needed which had oxidative potential but would not interact with the virus’ surface. The initial intention was to use HEPES buffer, but as it precipitated with SiW, MES was used instead, and the structure of a HEPES-SiW complex could be solved.

3.4.1 Structure Nr 18 - $(\text{HGly}_3)_4[\text{SiW}_{12}\text{O}_{40}] \cdot 2\text{H}_2\text{O}$

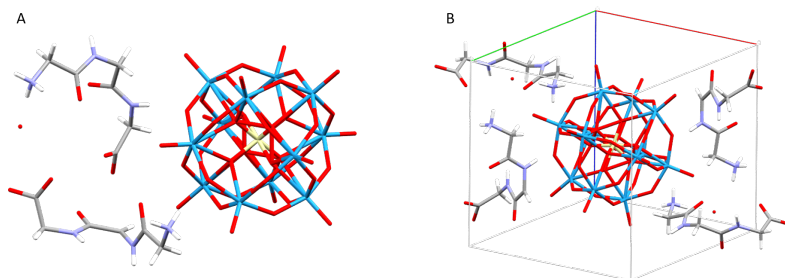


Figure 52. Structure **18** shown as molecular arrangement (A) and packing motif (B).

Structure **18** contains one SiW, four triglycine molecules and two water molecules (Fig. 52), $Z = 1$, with a triclinic Space group P-1 (Table 19). It superficially resembles **1** and **2**, though the POM heteroatom is silicon rather than phosphorus. SiW has a -4 charge while PW has -3 , so the interactions with peptide will differ slightly. Each POM corresponds to four peptides stoichiometrically, but it makes direct H-bonds with six surrounding peptides, mainly via amine groups, but also amide and carbonyl groups.

3.4.2 Structure Nr 19 - $(\text{HEPES})_3(\text{H}_3\text{O})[\text{SiW}_{12}\text{O}_{40}] \cdot \text{H}_2\text{O}$

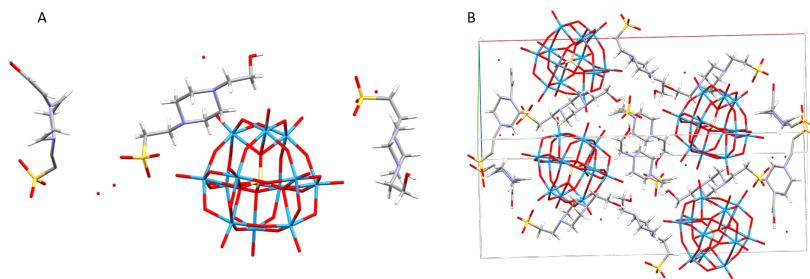


Figure 53. Structure **19** shown as molecular arrangement (A) and packing motif (B).

Structure **19** contains one SiW, three 4-(2-hydroxyethyl)-1-piperazineethanesulfonic acid (HEPES) molecules, and four water molecules in an asymmetric unit (Fig. 53), $Z = 4$, with a monoclinic Space group P $2_1/c$

(Table 20). SiW precipitated in HEPES buffer and, when crystallized carefully, yielded this structure. Notably, a similar buffer compound, MES (2-(N-morpholino)ethanesulfonic acid), did not precipitate with SiW. There was also diglycine present in solution, but it is not included in the structure, suggesting a higher affinity for HEPES towards SiW.

3.4.3 Discussion

18 resembles **1** and **2**, with H-bonding between POM and amine or amide groups, with some electrostatic interactions. **19** is displaying almost entirely electrostatic interactions. As these formed at neutral pH it is likely that the ligands lack much charge to interact with the POM. The high affinity for HEPES to bind SiW is surprising, especially as the similar MES molecule did not interact noticeably with SiW. Subtle differences can clearly have major effects, as section 3.3 showed, and the composition of the solution needs consideration when working with NPs, as was discussed in section 3.2. If an NP is intended for biological or medical use, it will likely be in a buffer, and from these results, the choice of buffer will need to consider interactions with the NP.

3.5 Sol-Gel materials

Not all materials produced were crystals. The following materials were produced as side products of the main objective, but are interesting enough to discuss in detail. They formed by the Sol-Gel process, where dissolved chemicals form a colloidal solution (the sol), which then form an integrated network as a solid (the gel).

3.5.1 ZrP

Parac-Vogt and colleagues reported a structure of Zr-substituted PW, which interacted with protein (Vandebroek et al. 2018), and degraded peptide bonds (T. Ly et al. 2013). The evidence of successful insertion of Zr is insufficient, and likely the Zr and phosphate from the buffer formed the compound described below.

During synthesis of **10**, white precipitate formed. This was analysed by SEM and EDS (Fig. 54), and showed it was likely microparticles of

zirconium phosphate (ZrP). It was synthesized in isolation and characterized with respect to morphology, composition and catalytic ability.

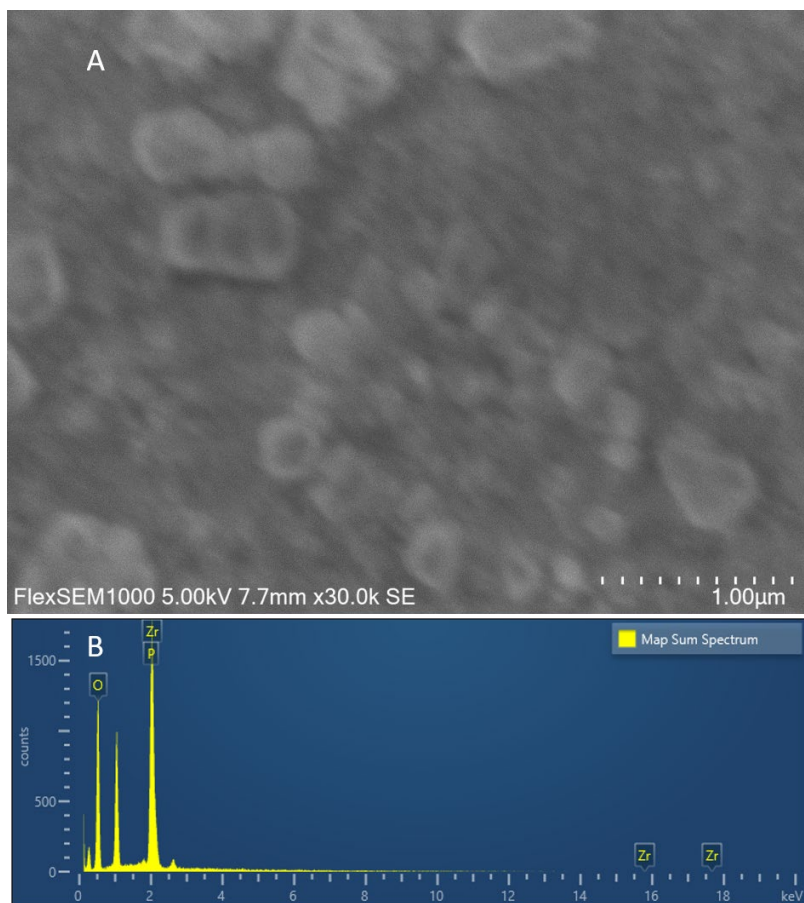


Figure 54. A: SEM image of ZrP particles at 30 000 times magnification. B: EDS spectrum of ZrP particles.

As there are reports of zirconium-substituted PW degrading peptide bonds (Vandebroek et al. 2018), the possibility of this compound being the true catalyst was present. To test this, an NMR experiment was performed, where diglycine was incubated with ZrP at 37°C for one week. The results are shown in Fig. 55. After incubation, there was a new peak, not present in

the control, at a chemical shift corresponding to glycine, indicating the hydrolysis of diglycine.

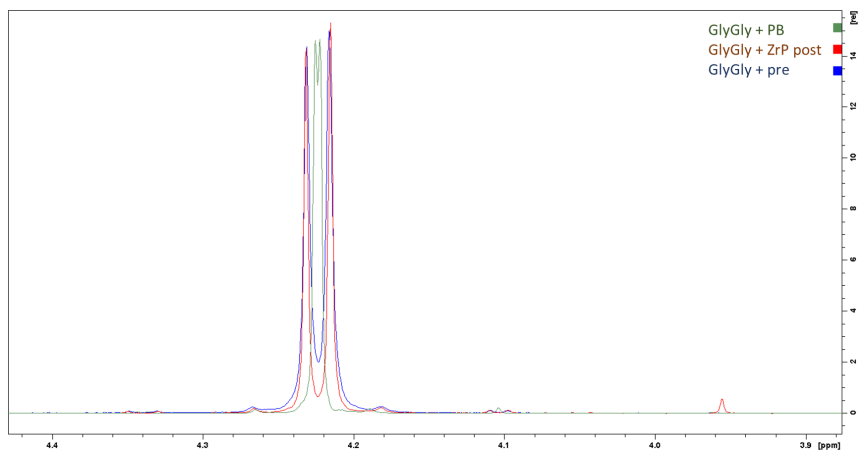


Figure 55. ¹H-NMR spectra of diglycine before incubation with ZrP (blue), after incubation (red) and a control without ZrP (green).

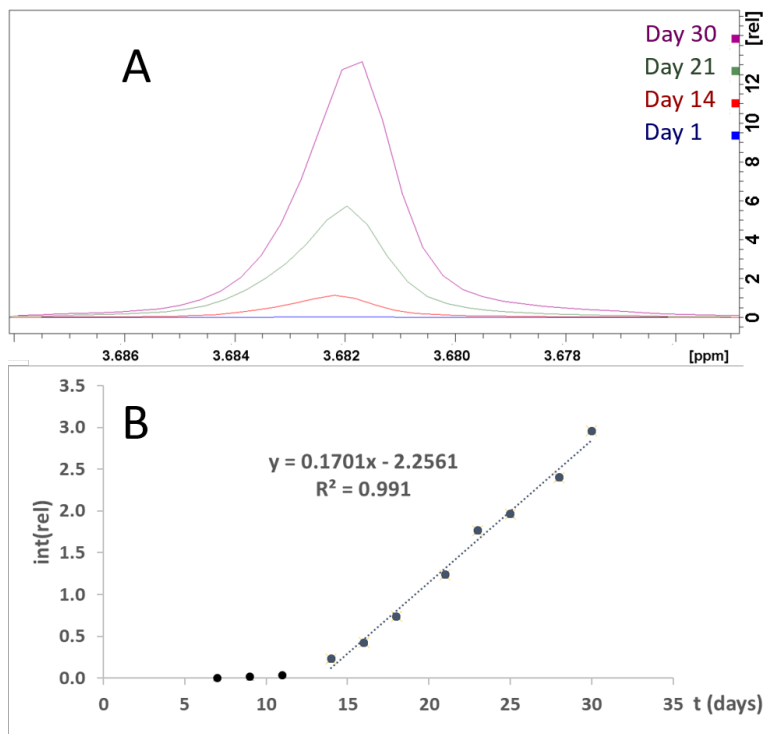


Figure 56. A: ¹H-NMR spectra focused on the Gly signal at different times of incubation (normalized against a DSS signal). B: Integral of signals plotted against time.

To further investigate this reaction, another experiment was performed, where the incubation was over one month, and regular readings were made via NMR (Fig. 56). After two weeks, a linear increase in glycine began, corresponding to a zero-order reaction, as would be expected for this type of catalyst. The lag at the beginning may be explained as the ZrP “maturing” into microcrystals, which are known to have catalytic applications (Cheng & Chuah 2020).

3.5.2 PW microspheres

When attempting to synthesize Ti substituted PW as described in Hayashi et al. 2005, precipitate formed. Under SEM this precipitate contained spherical particles, a few micrometres in diameter, and some broken spheres appeared as though they were hollow. Titration with NaOH showed them to be stable

at neutral pH, which could be beneficial, as PW has many desirable properties, but is limited in applications due to its instability at neutral and alkaline pH.

The PW microspheres were analysed by TEM, AFM (Fig. 57), SEM, XRPD, TGA, and EDS (Fig. 58). The SEM shows particles ranging from 0.8 to 2 μm in diameter, with broken spheres appearing hollow. TEM and AFM show that these are made up of smaller spheres, approximately 20 nm in diameter, which are presumably made up of PW. As the synthesis is very similar to **11**, that structure may be considered a “snapshot” of the partially assembled particles, with highly hydrated PW in contact with each other. XRPD patterns (Fig. 58B) are consistent with hydrated PW, but grows more amorphous over time. TGA showed good thermal stability, with only loss of water up to 500°C (Fig. 58D). EDS showed high amounts of tungsten and oxygen, with smaller amounts of titanium and potassium (Fig. 58E).

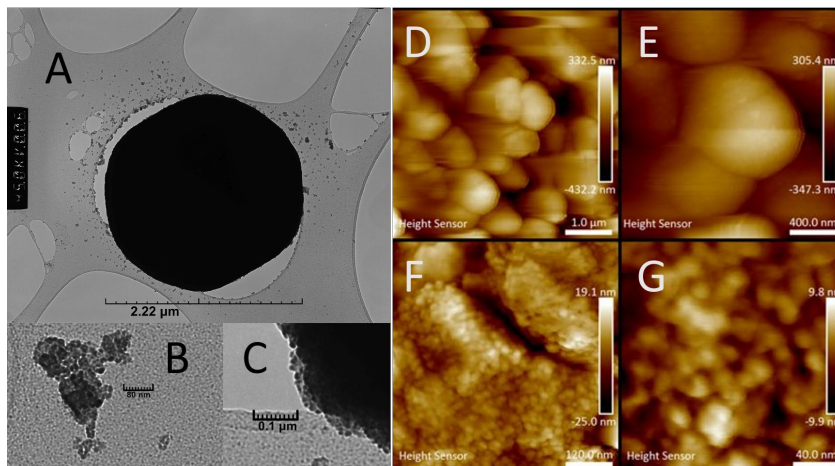


Figure 57. A-C: TEM of PW microspheres. D-G: AFM of microspheres.

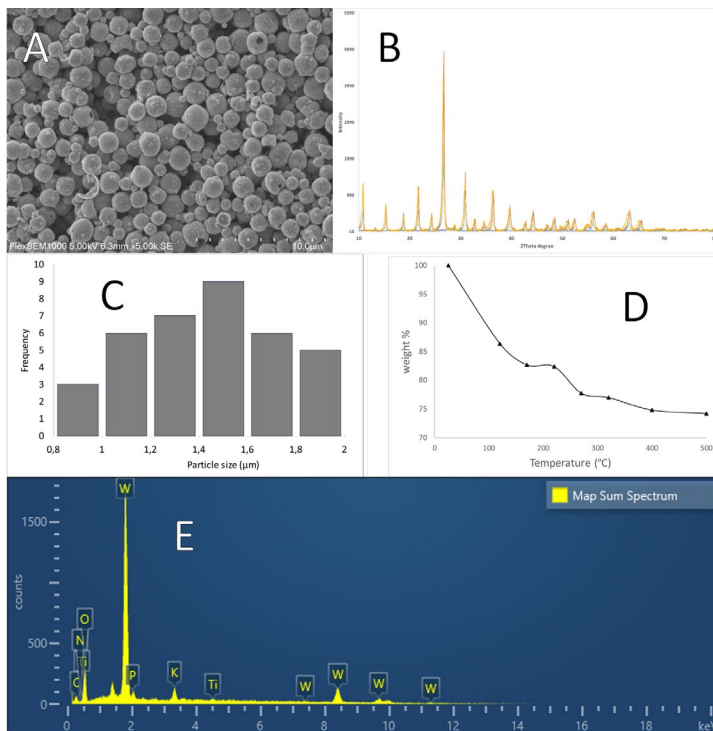


Figure 58. Analysis of PW microspheres. A: SEM image. B: XRPD. C: Size distribution. D: TGA curve. E: EDS spectrum.

The electrocatalytic experiments were performed at pH 0, 3 and 7. The overpotential was low at pH 0, at 286 mV for the OER, at pH 3 it was 308 mV and at pH 7 it was 397 mV (Fig. 59C). The cyclic voltammogram showed a redox peak at 0.72 V for pH 7 and two peaks at 0.72 V and 0.50 V (Fig. 59B), indicating W^{6+}/W^{5+} for both as well as W^{5+}/W^{4+} for the latter. The Tafel slopes calculated from LSV measurements were 83 mV/dec at pH 0, 0.86 mV/dec at pH 3, and 96 mV/dec at pH 7. The Tafel slopes at pH 0 and 7 are comparable to that of RuO_2 (Qin et al. 2022), and the latter is of particular note, as water splitting at neutral pH is highly desirable.

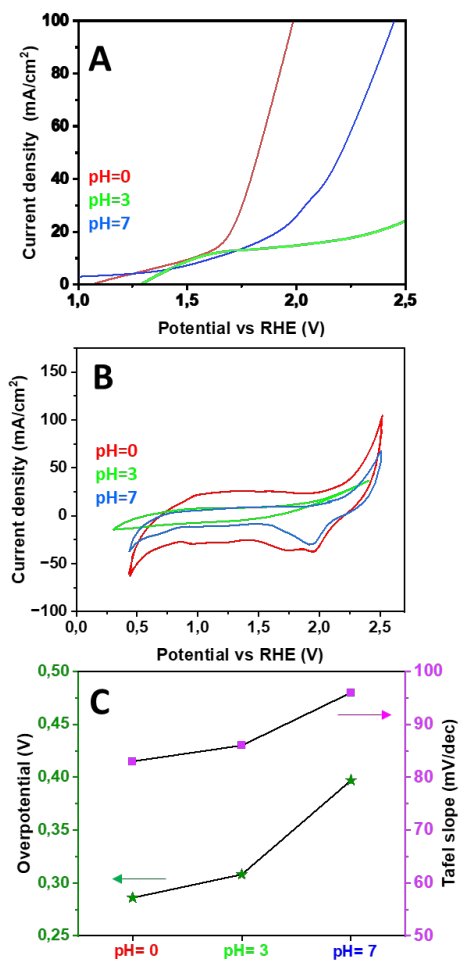


Figure 59. Electrochemical measurements at pH 0, 3, and 7. A: LSV, B: CV, C: pH dependence of the overpotential and Tafel slope.

4. Conclusions

The crystal structures presented here show a number of factors that influence how NPs interact with biomolecules. First, the nature of the NP plays a role, as the M-O bond can have varying degrees of polarity depending on the metal, and thus varying partial charge on the surface oxygen. Different heteroatoms will also affect the NP, affecting its stability under different conditions, and occasionally changing its affinity for ligands. Second, the nature of the ligand plays a role, in terms of charge, size, shape and hydrophobicity. Third, the environment plays a role, as these interactions seldom occur in isolation. Dissolved ions and organic molecules can compete with the intended ligand, and steal its spot on the NP.

In addition, two sol-gel materials were produced, and showed interesting catalytic abilities. ZrP microcrystals were able to hydrolyze the peptide bond, and PW microspheres were able to split water electrocatalytically, at a comparable efficiency to commercial catalysts.

References

- Abramov, P.A., Shmakova, A.A., Haouas, M., Fink, G., Cadot, E. & Sokolov, M.N. (2016). Self-assembly of $[\text{PNbxW}_{12-x}\text{O}_{40}]_n$ -Keggin anions – a simple way to mixed Nb–W polyoxometalates. *New Journal of Chemistry*, 41 (1), 256–262. <https://doi.org/10.1039/C6NJ02637K>
- Absillis, G. & Parac-Vogt, T.N. (2012). Peptide Bond Hydrolysis Catalyzed by the Wells–Dawson $\text{Zr}(\alpha_2\text{-P}_2\text{W}_{17}\text{O}_{61})_2$ Polyoxometalate. *Inorganic Chemistry*, 51 (18), 9902–9910. <https://doi.org/10.1021/ic301364n>
- Amiri, M., Martin, N.P., Feng, C.-L., Lovio, J.K. & Nyman, M. (2021). Deliberate Construction of Polyoxoniobates Exploiting the Carbonate Ligand. *Angewandte Chemie*, 133 (22), 12569–12574. <https://doi.org/10.1002/ange.202017367>
- Antelo, J., Arce, F. & Fiol, S. (2015). Arsenate and phosphate adsorption on ferrihydrite nanoparticles. Synergetic interaction with calcium ions. *Chemical Geology*, 410, 53–62. <https://doi.org/10.1016/j.chemgeo.2015.06.011>
- Anyushin, A.V., Sap, A., Quanten, T., Proost, P. & Parac-Vogt, T.N. (2018). Selective Hydrolysis of Ovalbumin Promoted by Hf(IV)-Substituted Wells-Dawson-Type Polyoxometalate. *Frontiers in Chemistry*, 6. <https://doi.org/10.3389/fchem.2018.00614>
- Aoto, H., Matsui, K., Sakai, Y., Kuchizi, T., Sekiya, H., Osada, H., Yoshida, T., Matsunaga, S. & Nomiya, K. (2014). Zirconium(IV)- and hafnium(IV)-containing polyoxometalates as oxidation precatalysts: Homogeneous catalytic epoxidation of cyclooctene by hydrogen peroxide. *Journal of Molecular Catalysis A: Chemical*, 394, 224–231. <https://doi.org/10.1016/j.molcata.2014.07.020>
- Bajuk-Bogdanović, D., Uskoković-Marković, S., Hercigonja, R., Popa, A. & Holclajtner-Antunović, I. (2016). Study of the decomposition pathway of 12-molybdophosphoric acid in aqueous solutions by micro Raman spectroscopy. *Spectrochimica Acta Part A: Molecular and Biomolecular Spectroscopy*, 153, 152–159. <https://doi.org/10.1016/j.saa.2015.08.029>

- Bamoharram, F.F. (2009). Vibrational Spectra Study of the Interactions Between Keggin Heteropolyanions and Amino Acids. *Molecules*, 14 (9), 3214–3221. <https://doi.org/10.3390/molecules14093214>
- Bertucci, S. & Lova, P. (2024). Exploring Solar Energy Solutions for Per- and Polyfluoroalkyl Substances Degradation: Advancements and Future Directions in Photocatalytic Processes. *Solar RRL*, 8 (9), 2400116. <https://doi.org/10.1002/solr.202400116>
- Bijelic, A. & Rompel, A. (2015). The use of polyoxometalates in protein crystallography – An attempt to widen a well-known bottleneck. *Coordination Chemistry Reviews*, 299, 22–38. <https://doi.org/10.1016/j.ccr.2015.03.018>
- Blanco, E., Shen, H. & Ferrari, M. (2015). Principles of nanoparticle design for overcoming biological barriers to drug delivery. *Nature Biotechnology*, 33 (9), 941–951. <https://doi.org/10.1038/nbt.3330>
- Brünle, S., Poppe, J., Hail, R., Demmer, U. & Ermler, U. (2018). The molybdenum storage protein — A bionanolab for creating experimentally alterable polyoxomolybdate clusters. *Journal of Inorganic Biochemistry*, 189, 172–179. <https://doi.org/10.1016/j.jinorgbio.2018.09.011>
- Buller, A.R. & Townsend, C.A. (2013). Intrinsic evolutionary constraints on protease structure, enzyme acylation, and the identity of the catalytic triad. *Proceedings of the National Academy of Sciences*, 110 (8), E653–E661. <https://doi.org/10.1073/pnas.1221050110>
- Cedervall, T., Lynch, I., Lindman, S., Berggard, T., Thulin, E., Nilsson, H., Dawson, K.A. & Linse, S. (2007). Understanding the nanoparticle-protein corona using methods to quantify exchange rates and affinities of proteins for nanoparticles. *Proceedings of the National Academy of Sciences*, 104 (7), 2050–2055. <https://doi.org/10.1073/pnas.0608582104>
- Chavali, M.S. & Nikolova, M.P. (2019). Metal oxide nanoparticles and their applications in nanotechnology. *SN Applied Sciences*, 1 (6), 607. <https://doi.org/10.1007/s42452-019-0592-3>
- Chen, S., Huang, H., Jiang, P., Yang, K., Diao, J., Gong, S., Liu, S., Huang, M., Wang, H. & Chen, Q. (2020). Mn-Doped RuO₂ Nanocrystals as Highly Active Electrocatalysts for Enhanced Oxygen Evolution in Acidic Media. *ACS Catalysis*, 10 (2), 1152–1160. <https://doi.org/10.1021/acscatal.9b04922>
- Cheng, Y. & Chuah, G.K. (2020). The synthesis and applications of α -zirconium phosphate. *Chinese Chemical Letters*, 31 (2), 307–310. <https://doi.org/10.1016/j.ccllet.2019.04.063>

- Colliard, I. & Nyman, M. (2021). CeIV70 Oxosulfate Rings, Frameworks, Supramolecular Assembly, and Redox Activity. *Angewandte Chemie*, 133 (13), 7384–7391. <https://doi.org/10.1002/ange.202016522>
- Coyle, L., S. Middleton, P., J. Murphy, C., Clegg, W., W. Harrington, R. & John Errington, R. (2012). Protonolysis of [(i PrO)TiMo 5 O 18] 3 - : access to a family of TiMo 5 Lindqvist type polyoxometalates. *Dalton Transactions*, 41 (3), 971–981. <https://doi.org/10.1039/C1DT11256B>
- Daou, T.J., Begin-Colin, S., Grenèche, J.M., Thomas, F., Derory, A., Bernharddt, P., Legaré, P. & Pourroy, G. (2007). Phosphate Adsorption Properties of Magnetite-Based Nanoparticles. *Chemistry of Materials*, 19 (18), 4494–4505. <https://doi.org/10.1021/cm071046v>
- Di, A., Schmitt, J., Silva, M.A. da, Zakir Hossain, K.M., Mahmoudi, N., John Errington, R. & J. Edler, K. (2020). Self-assembly of amphiphilic polyoxometalates for the preparation of mesoporous polyoxometalate-titania catalysts. *Nanoscale*, 12 (43), 22245–22257. <https://doi.org/10.1039/D0NR05967F>
- Duong-Ly, K.C. & Gabelli, S.B. (2014). Chapter Seven - Salting out of Proteins Using Ammonium Sulfate Precipitation. I: Lorsch, J. (red.) *Methods in Enzymology*. Academic Press. 85–94. <https://doi.org/10.1016/B978-0-12-420119-4.00007-0>
- Egerton, R.F. (2016). *Physical Principles of Electron Microscopy*. Springer International Publishing. <https://doi.org/10.1007/978-3-319-39877-8>
- Faltermann, S., Zucchi, S., Kohler, E., Blom, J.F., Pernthaler, J. & Fent, K. (2014). Molecular effects of the cyanobacterial toxin cyanopeptolin (CP1020) occurring in algal blooms: Global transcriptome analysis in zebrafish embryos. *Aquatic Toxicology*, 149, 33–39. <https://doi.org/10.1016/j.aquatox.2014.01.018>
- Farsani, M.R. & Yadollahi, B. (2014). Synthesis, characterization and catalytic performance of a Fe polyoxometalate/silica composite in the oxidation of alcohols with hydrogen peroxide. *Journal of Molecular Catalysis A: Chemical*, 392, 8–15. <https://doi.org/10.1016/j.molcata.2014.05.001>
- Fischer, G., Cao, X., Cox, N. & Francis, M. (2005). The FT-IR spectra of glycine and glycyglycine zwitterions isolated in alkali halide matrices. *Chemical Physics*, 313 (1), 39–49. <https://doi.org/10.1016/j.chemphys.2004.12.011>

- Fleming, I. & Williams, D. (2019). *Spectroscopic Methods in Organic Chemistry*. Springer International Publishing. <https://doi.org/10.1007/978-3-030-18252-6>
- Furukawa, H., Cordova, K.E., O’Keeffe, M. & Yaghi, O.M. (2013). The Chemistry and Applications of Metal-Organic Frameworks. *Science*, 341 (6149), 1230444. <https://doi.org/10.1126/science.1230444>
- Greco, G., Arndt, T., Schmuck, B., Francis, J., Bäcklund, F.G., Shilkova, O., Barth, A., Gonska, N., Seisenbaeva, G., Kessler, V., Johansson, J., Pugno, N.M. & Rising, A. (2021). Tyrosine residues mediate supercontraction in biomimetic spider silk. *Communications Materials*, 2 (1), 1–10. <https://doi.org/10.1038/s43246-021-00147-w>
- Guo, S., Zhang, S. & Sun, S. (2013). Tuning Nanoparticle Catalysis for the Oxygen Reduction Reaction. *Angewandte Chemie International Edition*, 52 (33), 8526–8544. <https://doi.org/10.1002/anie.201207186>
- Hamm, H.E. (1998). The Many Faces of G Protein Signaling *. *Journal of Biological Chemistry*, 273 (2), 669–672. <https://doi.org/10.1074/jbc.273.2.669>
- Han, Z., Wang, E., Luan, G., Li, Y., Zhang, H., Duan, Y., Hu, C. & Hu, N. (2002). Synthesis, properties and structural characterization of an intermolecular photosensitive complex: (HGly-Gly)₃ PMo₁₂ O₄₀ · 4H₂ O. *Journal of Materials Chemistry*, 12 (4), 1169–1173. <https://doi.org/10.1039/B107225K>
- Haugstad, G. (2012). *Atomic Force Microscopy: Understanding Basic Modes and Advanced Applications*. John Wiley & Sons.
- Hayashi, K., Takahashi, M. & Nomiya, K. (2005). Novel Ti–O–Ti bonding species constructed in a metal- oxide cluster. *Dalton Transactions*, 0 (23), 3751–3756. <https://doi.org/10.1039/B508738D>
- Hochella, M.F., Lower, S.K., Maurice, P.A., Penn, R.L., Sahai, N., Sparks, D.L. & Twining, B.S. (2008). Nanominerals, Mineral Nanoparticles, and Earth Systems. *Science*, 319 (5870), 1631–1635. <https://doi.org/10.1126/science.1141134>
- I. Gumerova, N. & Rompel, A. (2020). Polyoxometalates in solution: speciation under spotlight. *Chemical Society Reviews*, 49 (21), 7568–7601. <https://doi.org/10.1039/D0CS00392A>
- Johnson, H. (2015). Uncovering dynamic phosphorylation signaling using mass spectrometry. *International Journal of Mass Spectrometry*, 391, 123–138. <https://doi.org/10.1016/j.ijms.2015.08.002>
- Karlsson, H.L., Gustafsson, J., Cronholm, P. & Möller, L. (2009). Size-dependent toxicity of metal oxide particles—A comparison between

- nano- and micrometer size. *Toxicology Letters*, 188 (2), 112–118. <https://doi.org/10.1016/j.toxlet.2009.03.014>
- Keggin, J.F. & Bragg, W.L. (1934). The structure and formula of 12-phosphotungstic acid. *Proceedings of the Royal Society of London. Series A, Containing Papers of a Mathematical and Physical Character*, 144 (851), 75–100. <https://doi.org/10.1098/rspa.1934.0035>
- Kessler, V.G. & Seisenbaeva, G.A. (2023). Molecular mechanisms of the metal oxide sol-gel process and their application in approaches to thermodynamically challenging complex oxide materials. *Journal of Sol-Gel Science and Technology*, 107 (1), 190–200. <https://doi.org/10.1007/s10971-023-06120-y>
- Koppenol, W.H. (1993). The centennial of the Fenton reaction. *Free Radical Biology and Medicine*, 15 (6), 645–651. [https://doi.org/10.1016/0891-5849\(93\)90168-T](https://doi.org/10.1016/0891-5849(93)90168-T)
- Long, D.-L., Yan, J., Oliva, A.R. de la, Busche, C., N. Miras, H., John Errington, R. & Cronin, L. (2013). A redox-triggered structural rearrangement in an iodate-templated polyoxotungstate cluster cage. *Chemical Communications*, 49 (84), 9731–9733. <https://doi.org/10.1039/C3CC45659E>
- Lundqvist, M., Stigler, J., Elia, G., Lynch, I., Cedervall, T. & Dawson, K.A. (2008). Nanoparticle size and surface properties determine the protein corona with possible implications for biological impacts. *Proceedings of the National Academy of Sciences*, 105 (38), 14265–14270. <https://doi.org/10.1073/pnas.0805135105>
- McCreery, R.L. (2008). Advanced Carbon Electrode Materials for Molecular Electrochemistry. *Chemical Reviews*, 108 (7), 2646–2687. <https://doi.org/10.1021/cr068076m>
- Meinecke, B. & Meinecke-Tillmann, S. (1993). Effects of α -amanitin on nuclear maturation of porcine oocytes in vitro. *Reproduction*, 98 (1), 195–201. <https://doi.org/10.1530/jrf.0.0980195>
- M. Marsh, B., Zhou, J. & Garand, E. (2015). Vibrational spectroscopy of isolated copper(ii) complexes with deprotonated triglycine and tetraglycine peptides. *RSC Advances*, 5 (3), 1790–1795. <https://doi.org/10.1039/C4RA09655J>
- Müller, A., Krickemeyer, E., Bögge, H., Schmidtman, M., Beugholt, C., Kögerler, P. & Lu, C. (1998). Formation of a Ring-Shaped Reduced “Metal Oxide” with the Simple Composition [(MoO₃)₁₇₆(H₂O)₈₀H₃₂]. *Angewandte Chemie International Edition*, 37 (9), 1220–1223. [https://doi.org/10.1002/\(SICI\)1521-3773\(19980518\)37:9<1220::AID-ANIE1220>3.0.CO;2-G](https://doi.org/10.1002/(SICI)1521-3773(19980518)37:9<1220::AID-ANIE1220>3.0.CO;2-G)

- Müller, A., Krickemeyer, E., Meyer, J., Bögge, H., Peters, F., Plass, W., Diemann, E., Dillinger, S., Nonnenbruch, F., Randerath, M. & Menke, C. (1995). [Mo₁₅₄(NO)₁₄O₄₂₀(OH)₂₈(H₂O)₇₀](25 ± 5)⁻: A Water-Soluble Big Wheel with More than 700 Atoms and a Relative Molecular Mass of About 24000. *Angewandte Chemie International Edition in English*, 34 (19), 2122–2124. <https://doi.org/10.1002/anie.199521221>
- Qin, Y., Yu, T., Deng, S., Zhou, X.-Y., Lin, D., Zhang, Q., Jin, Z., Zhang, D., He, Y.-B., Qiu, H.-J., He, L., Kang, F., Li, K. & Zhang, T.-Y. (2022). RuO₂ electronic structure and lattice strain dual engineering for enhanced acidic oxygen evolution reaction performance. *Nature Communications*, 13 (1), 3784. <https://doi.org/10.1038/s41467-022-31468-0>
- Rietveld, H.M. (1969). A profile refinement method for nuclear and magnetic structures. *Journal of Applied Crystallography*, 2 (2), 65–71. <https://doi.org/10.1107/S0021889869006558>
- Roduner, E. (2018). Selected fundamentals of catalysis and electrocatalysis in energy conversion reactions—A tutorial. *Catalysis Today*, 309, 263–268. <https://doi.org/10.1016/j.cattod.2017.05.091>
- Rominger, K.M., Nestor, G., Eriksson, J.E., Seisenbaeva, G.A. & Kessler, V.G. (2019). Complexes of Keggin POMs [PM₁₂O₄₀]₃⁻ (M = Mo, W) with GlyGly Peptide and Arginine – Crystal Structures and Solution Reactivity. *European Journal of Inorganic Chemistry*, 2019 (39–40), 4297–4305. <https://doi.org/10.1002/ejic.201900611>
- Salazar Marcano, D.E., Lentink, S., Chen, J.-J., Anyushin, A.V., Moussawi, M.A., Bustos, J., Van Meerbeek, B., Nyman, M. & Parac-Vogt, T.N. (2024). Supramolecular Self-Assembly of Proteins Promoted by Hybrid Polyoxometalates. *Small*, 20 (25), 2312009. <https://doi.org/10.1002/smll.202312009>
- Seisenbaeva, G.A., Sundberg, M., Nygren, M., Dubrovinsky, L. & Kessler, V.G. (2004). Thermal decomposition of the methoxide complexes MoO(OMe)₄, Re₄O₆(OMe)₁₂ and (Re_{1-x}Mo_x)O₆(OMe)₁₂ (0.24 ≤ x ≤ 0.55). *Materials Chemistry and Physics*, 87 (1), 142–148. <https://doi.org/10.1016/j.matchemphys.2004.05.025>
- Sharma, V.K., Filip, J., Zboril, R. & Varma, R.S. (2015). Natural inorganic nanoparticles – formation, fate, and toxicity in the environment. *Chemical Society Reviews*, 44 (23), 8410–8423. <https://doi.org/10.1039/C5CS00236B>
- Song, X., Zhu, W., Li, K., Wang, J., Niu, H., Gao, H., Gao, W., Zhang, W., Yu, J. & Jia, M. (2016). Epoxidation of olefins with oxygen/isobutyraldehyde over transition-metal-substituted

- phosphomolybdic acid on SBA-15. *Catalysis Today*, 259, 59–65. <https://doi.org/10.1016/j.cattod.2015.04.042>
- Soria-Carrera, H., Atrián-Blasco, E., Martín-Rapún, R. & Mitchell, S.G. (2022). Polyoxometalate–peptide hybrid materials: from structure–property relationships to applications. *Chemical Science*, 14 (1), 10–28. <https://doi.org/10.1039/D2SC05105B>
- Sun, T.-L., Kan, T.-T., Yan, J.-H. & Zhang, H. (2020). Design and synthesis of rare earth organic-inorganic hybrid material based on dawson type polyoxometallate {P2Mo18}. *Inorganic Chemistry Communications*, 112, 107717. <https://doi.org/10.1016/j.inoche.2019.107717>
- Timofeev, V. & Samygina, V. (2023). Protein Crystallography: Achievements and Challenges. *Crystals*, 13 (1), 71. <https://doi.org/10.3390/cryst13010071>
- T. Ly, H.G., Absillis, G. & N. Parac-Vogt, T. (2013). Amide bond hydrolysis in peptides and cyclic peptides catalyzed by a dimeric Zr(iv)-substituted Keggin type polyoxometalate. *Dalton Transactions*, 42 (30), 10929–10938. <https://doi.org/10.1039/C3DT50705J>
- Tuteja, N. (2009). Signaling through G protein coupled receptors. *Plant Signaling & Behavior*, 4 (10), 942–947. <https://doi.org/10.4161/psb.4.10.9530>
- Vandebroek, L., Van Meervelt, L. & Parac-Vogt, T.N. (2018). Direct observation of the ZrIV inter-action with the carboxamide bond in a noncovalent complex between Hen Egg White Lysozyme and a Zr-substituted Keggin polyoxometalate. *Acta Crystallographica Section C: Structural Chemistry*, 74 (11), 1348–1354. <https://doi.org/10.1107/S2053229618010690>
- Wei, H. & Wang, E. (2013). Nanomaterials with enzyme-like characteristics (nanozymes): next-generation artificial enzymes. *Chemical Society Reviews*, 42 (14), 6060–6093. <https://doi.org/10.1039/C3CS35486E>
- Williams, D.B. & Carter, C.B. (1996). The Transmission Electron Microscope. I: Williams, D.B. & Carter, C.B. (red.) *Transmission Electron Microscopy: A Textbook for Materials Science*. Springer US. 3–17. https://doi.org/10.1007/978-1-4757-2519-3_1
- Zhou, X., He, P. & Zhang, C. (2020). Codoped Phosphotungstate as an Efficient Heterogeneous Catalyst for the Synthesis of n-Butyl Oleate. *ACS Omega*, 5 (20), 11529–11534. <https://doi.org/10.1021/acsomega.0c00693>
- Zhu, Z., Tain, R. & Rhodes, C. (2003). A study of the decomposition behaviour of 12-tungstophosphate heteropolyacid in solution.

Canadian Journal of Chemistry, 81 (10), 1044–1050.
<https://doi.org/10.1139/v03-129>

Popular science summary

Nanoparticles are tiny bits of matter, somewhere around 0.00000001 meters in diameter. They occur naturally, but can also be made artificially, and are often made for the sake of catalysis. Catalysts are materials that make a chemical reaction happen more easily, without being consumed themselves. Having nanoparticles as catalysts is often beneficial, because the reaction happens on the surface of the catalysts. Nanoparticles have much more surface area as compared to bulk material thanks to the square-cube law, which states that, as an object grows in size, its volume grows faster than its surface area. Thus, to maximize surface area, we want as small objects as possible, and the reaction can go as fast as possible.

The reactions that can be catalysed vary, but are often transforming organic molecules. For the reaction to happen, the molecule often need to sit on the surface of the catalyst. That is why it is interesting to see how molecules tend to interact with nanoparticles, which is what we were trying to find out here. We found that some of the factors that control how molecules interact with the nanoparticle are: the metals that make up the nanoparticle, the amount of salt in the solution, the amount of acid in the solution, the makeup and shape of the molecules themselves, and whether there are other molecules that can bind the nanoparticle. Some of these may seem obvious, but it is important to have evidence and not just make assumptions. And now we have evidence.

Populärvetenskaplig sammanfattning

Nanopartiklar är små bitar av material, någonstans kring 0.00000001 meter i diameter. De finns naturligt, men kan även tillverkas artificiellt, och görs ofta för användning i katalys. Katalysatorer är material som gör att en kemisk reaktion händer lättare, utan att de förbrukas själva. Att ha nanopartiklar som katalysatorer är ofta fördelaktigt, eftersom reaktionen sker på ytan av katalysatorn. Nanopartiklar har mycket större ytareal jämfört med bulkmaterial tack vare kvadrat-kubförhållandet, som säger att när ett objekt ökar i storlek, så ökar dess volym snabbare än dess ytareal. Så för att maximera ytarean, så vill man ha så små objekt som möjligt, så att reaktionen kan gå så snabbt som möjligt.

Reaktionerna som ska katalyseras kan variera, men är ofta transformering av organiska molekyler. För att reaktionen ska ske så måste molekylen ofta sitta på katalysatorns yta. Därför är det intressant att se hur molekyler tenderar att interagera med nanopartiklar, vilket är vad vi försökt ta reda på här. Vi fann att några faktorer som kontrollerar hur molekyler interagerar med nanopartiklar är: metallerna som bygger upp nanopartiklarna, mängden salt i lösning, hur själva molekylerna är uppbyggda och formade, och huruvida det finns andra molekyler som kan binda nanopartiklarna. En del av dessa kan verka uppenbara, men det är viktigt att ha bevis och inte bara göra antaganden. Och nu har vi bevis.

Acknowledgements

I want to thank these people for help, support, advice and critique they have given me.

My principal supervisor Vadim Kessler, who has helped me grow as a scientist, teacher and writer, as well as taught me a lot about crystallography and chemistry in general. My co-supervisors Mats Sandgren and Kristina Nilsson Ek Dahl, thank you as well.

Gulaim Seisenbaeva, co-professor in our group, was always there with advice and feedback, and helps everyone with all manner of instruments.

Fredric Svensson, thank you for all the help when I first came here as a biologist lost in a chemistry lab. Gustav Nestor, thank you for helping with NMR, and for teaching me how to run it. Jan Eriksson, thank you for help with MS. Thank you, Geoffrey Daniel, who helped out with making TEM images. Professor Mats Johnsson and Dr Jayeta Saha, thank you for help with electrolysis, and German Salazar helped with discussions about electrocatalysis. Thanks to Tetyana Budnyak, who helped us with surface area measurements.

Students Kayly Rominger, Timothy DeDonder: I never met you, but your work laid the foundation for mine. Wannes De Turck, Edgar Stigell and Timothe Guerrin did good work here, and I wish them luck in their future careers.

Current and former colleagues: Troy Breijaert, you'll do fine when it's your turn; Filip Kozłowski, good luck with teaching and travelling; Rasmus Björk, you left us too soon; Ani Vardanyan, eventually you will have been here longer than me; Marijana Lakić, I hope you're doing well wherever you end up; Sara Targonska, resident sunbeam; Jakob Whittaker, we don't see enough of you; Oksana Dudarko, we stand with Ukraine.

Appendix

Crystallographic data.

Table 2. Crystallographic data for structure **1**.

Compound nr 1	
Chemical formula	C ₁₈ H ₂₄ Mo ₁₂ N ₉ O ₅₂ P
Formula weight	2380.71
Temperature (K)	296(2)
Wavelength	0.71073 Å
Crystal size	0.36 × 0.21 × 0.19 mm
Crystal system	Triclinic
Space group	P-1
Unit cell dimensions	a: 11.0479(17) Å α: 102.063(2)°
	b: 15.109(2) Å β: 96.441(2)°
	c: 18.720(3) Å γ: 97.031(2)°
Volume (Å³)	3002.0(8)
Z	2
Theta data range for collection	2.16 to 23.84°
Reflections collected	26695
Independent reflections	7721
Nr. of obs. independent refl; I>2σ(I)	9173
Final R indices, observed	R1 = 0.0702, wR2 = 0.1613
Final R indices, all data	R1 = 0.0813, wR2 = 0.1653

Table 3. Crystallographic data for structure **2**

Compound nr 2	
Chemical formula	C ₁₈ H ₃₀ N ₉ O ₅₂ PW ₁₂
Formula weight	3441.68
Temperature (K)	296(2)
Wavelength	0.71073 Å
Crystal size	0.38 × 0.18 × 0.12 mm
Crystal system	Monoclinic
Space group	P2 ₁ /n
Unit cell dimensions	a: 14.448(6) Å α: 90.00 °
	b: 10.648(4) Å β: 92.187(6) °
	c: 41.167(18) Å γ: 90.00 °
Volume (Å³)	6328(5)
Z	4
Theta data range for collection	2.38 to 23.87 °
Reflections collected	42239
Independent reflections	6722
Nr. of obs. independent refl; I>2σ(I)	9763
Final R indices, observed	R1 = 0.0482, wR2 = 0.1121
Final R indices, all data	R1 = 0.0823, wR2 = 0.1270

Table 4. Crystallographic data for structure 3.

Compound nr 3	
Chemical formula	C ₂₄ H ₄₅ Mo ₁₂ N ₁₂ O ₅₅ P
Formula weight	2563.97
Temperature (K)	296(2)
Wavelength	0.71073 Å
Crystal size	0.3 × 0.27 × 0.26 mm
Crystal system	Triclinic
Space group	P-1
Unit cell dimensions	a: 14.177(2) Å α: 106.574(2)°
	b: 15.405(2) Å β: 101.890(2)°
	c: 16.209(2) Å γ: 106.216(2)°
Volume (Å³)	3097.0(8)
Z	2
Theta data range for collection	2.36 to 29.30°
Reflections collected	29698
Independent reflections	9567
Nr. of obs. independent refl; I>2σ(I)	10901
Final R indices, observed	R1 = 0.0343, wR2 = 0.1045
Final R indices, all data	R1 = 0.0400, wR2 = 0.1078

Table 5. Crystallographic data for structure 4.

Compound nr 4	
Chemical formula	C ₃₂ H ₈₈ N ₁₆ O ₁₄₈ P ₃ W ₃₆
Formula weight	9776.69
Temperature (K)	296(2)
Wavelength	0.71073 Å
Crystal size	0.34 × 0.26 × 0.22 mm
Crystal system	Tetragonal
Space group	P 4 ₂ /n
Unit cell dimensions	a: 18.991(14) Å α: 90°
	b: 18.991(14) Å β: 90°
	c: 25.049(16) Å γ: 90°
Volume (Å³)	9034(14)
Z	2
Theta data range for collection	2.40 to 20.65°
Reflections collected	79916
Independent reflections	4209
Nr. of obs. independent refl; I>2σ(I)	8120
Final R indices, observed	R1 = 0.0865, wR2 = 0.1893
Final R indices, all data	R1 = 0.1603, wR2 = 0.2130

Table 6. Crystallographic data for structure **5**.

Compound nr 5	
Chemical formula	C ₁₂ H ₄₁ Mo ₁₂ N ₆ O ₅₆ P
Formula weight	2347.76
Temperature (K)	296
Wavelength	0.71073 Å
Crystal size	0.33 × 0.31 × 0.09 mm
Crystal system	Triclinic
Space group	P-1
Unit cell dimensions	a: 12.7308(12) Å α: 97.8970(10)°
	b: 13.0510(12) Å β: 105.2180(10)°
	c: 18.0332(17) Å γ: 105.9070(10)°
Volume (Å³)	2708.77
Z	2
Theta data range for collection	2.26 to 29.27°
Reflections collected	26 853
Independent reflections	8786
Nr. of obs. independent refl; I>2σ(I)	9555
Final R indices, observed	R1 = 0.0263, wR2 = 0.0670
Final R indices, all data	R1 = 0.0296, wR2 = 0.0686

Table 7. Crystallographic data for structure 6.

Compound nr 6	
Chemical formula	C ₁₂ H ₄₃ Mo ₁₂ N ₆ O ₅₂ P
Formula weight	2285.77
Temperature (K)	296
Wavelength	0.71073 Å
Crystal size	0.24 × 0.2 × 0.08 mm
Crystal system	Monoclinic
Space group	P 2 ₁ /n
Unit cell dimensions	a: 12.788(2) Å α: 90°
	b: 31.897(5) Å β: 112.173(2)°
	c: 13.843(2) Å γ: 90°
Volume (Å³)	5228.8(15)
Z	4
Theta data range for collection	2.142 to 25.023°
Reflections collected	24390
Independent reflections	7929
Nr. of obs. independent refl; I>2σ(I)	9193
Final R indices, observed	R1 = 0.0494 , wR2 = 0.1407
Final R indices, all data	R1 = 0.0573, wR2 = 0.1448

Table 8. Crystallographic data for structure 7.

Compound nr 7	
Chemical formula	C ₈ H ₃₆ Mo ₁₂ N ₄ NaO ₅₅ P
Formula weight	2273.65
Temperature (K)	296
Wavelength	0.71073 Å
Crystal size	0.28 × 0.22 × 0.20 mm
Crystal system	Orthorhombic
Space group	Pbca
Unit cell dimensions	a: 17.3441(13) Å α: 90°
	b: 23.078(2) Å β: 90°
	c: 25.295(2) Å γ: 90°
Volume (Å³)	10124.8(14)
Z	8
Theta data range for collection	2.268 to 25.025°
Reflections collected	68807
Independent reflections	8046
Nr. of obs. independent refl; I>2σ(I)	8916
Final R indices, observed	R1 = 0.0373, wR2 = 0.1177
Final R indices, all data	R1 = 0.0419, wR2 = 0.1212

Table 9. Crystallographic data for structure 8.

Compound nr 8	
Chemical formula	C ₈ H ₃₄ Mo ₁₂ N ₄ NaO ₅₄ P
Formula weight	2255.63
Temperature (K)	296
Wavelength	0.71073 Å
Crystal size	0.22 × 0.20 × 0.14 mm
Crystal system	Monoclinic
Space group	P2 ₁ /c
Unit cell dimensions	a: 21.135(3) Å α: 90.00°
	b: 12.9339(16) Å β: 111.185(2)°
	c: 19.455(2) Å γ: 90.00°
Volume (Å³)	4958.7(11)
Z	4
Theta data range for collection	2.38 to 29.15°
Reflections collected	44715
Independent reflections	7531
Nr. of obs. independent refl; I>2σ(I)	8719
Final R indices, observed	R1 = 0.0304, wR2 = 0.1062
Final R indices, all data	R1 = 0.0355, wR2 = 0.1092

Table 10. Crystallographic data for structure **9**.

Compound nr 9	
Chemical formula	C ₄ H _{16.5} Mo ₁₂ N ₂ Na _{0.5} O ₄₆ P
Formula weight	2022.44
Temperature (K)	296
Wavelength	0.71073 Å
Crystal size	0.30 × 0.25 × 0.14 mm
Crystal system	Monoclinic
Space group	P2 ₁ /c
Unit cell dimensions	a: 19.443(8) Å α: 90°
	b: 12.745(5) Å β: 105.275(5)°
	c: 19.657(8) Å γ: 90°
Volume (Å³)	4699(3)
Z	4
Theta data range for collection	2.17 to 24.25°
Reflections collected	38785
Independent reflections	5180
Nr. of obs. independent refl; I>2σ(I)	7345
Final R indices, observed	R1 = 0.0991, wR2 = 0.2060
Final R indices, all data	R1 = 0.1333, wR2 = 0.2184

Table 11. Crystallographic data for structure **10**.

Compound nr 10	
Chemical formula	C ₄ H ₂₃ Mo ₁₂ N ₂ Na _{0.5} O ₄₇ P
Formula weight	2044.99
Temperature (K)	296
Wavelength	0.71073 Å
Crystal size	0.38 × 0.18 × 0.11 mm
Crystal system	Orthorhombic
Space group	Pbcn
Unit cell dimensions	a: 12.765(3) Å α: 90°
	b: 19.680(5) Å β: 90°
	c: 37.663(10) Å γ: 90°
Volume (Å³)	9462(4)
Z	8
Theta data range for collection	2.50 to 28.21°
Reflections collected	88347
Independent reflections	6480
Nr. of obs. independent refl; I>2σ(I)	8333
Final R indices, observed	R1 = 0.0553, wR2 = 0.1763
Final R indices, all data	R1 = 0.0703, wR2 = 0.1858

Table 12. Crystallographic data for structure **11**.

Compound nr 11	
Chemical formula	H ₆₅ LaO _{133.5} P ₂ W ₂₄
Formula weight	6494.77
Temperature (K)	163(2)
Wavelength	0.71073 Å
Crystal size	0.32 × 0.2 × 0.16 mm
Crystal system	Triclinic
Space group	P-1
Unit cell dimensions	a: 14.008(3) Å α: 88.978(5)°
	b: 15.140(3) Å β: 89.228(4)°
	c: 22.386(5) Å γ: 80.885(5)°
Volume (Å³)	4686.6(18)
Z	2
Theta data range for collection	2.26 to 35.79°
Reflections collected	57188
Independent reflections	17582
Nr. of obs. independent refl; I>2σ(I)	22324
Final R indices, observed	R1 = 0.0596 , wR2 = 0.1531
Final R indices, all data	R1 = 0.0787, wR2 = 0.1630

Table 13. Crystallographic data for structure **12**

Compound nr 12	
Chemical formula	C ₂₄ H _{31.5} N ₄ O ₅₂ PW ₁₂
Formula weight	3445.20
Temperature (K)	273(2)
Wavelength	0.71073 Å
Crystal size	0.130 × 0.180 × 0.240 mm
Crystal system	monoclinic
Space group	P 1 2 ₁ 1
Unit cell dimensions	a: 15.0118(6) Å α: 90°
	b: 26.6598(12) Å β: 101.782(2)°
	c: 15.5858(6) Å γ: 90°
Volume (Å³)	6106.2(4)
Z	4
Theta data range for collection	2.06 to 35.26°
Index ranges	-24 ≤ h ≤ 24, -42 ≤ k ≤ 42, -24 ≤ l ≤ 24
Reflections collected	103478
Independent reflections	50215
Nr. of obs. independent refl; I > 2σ(I)	42803
Final R indices, observed	R1 = 0.0402, wR2 = 0.0867
Final R indices, all data	R1 = 0.0527, wR2 = 0.0915

Table 14. Crystallographic data for structure **13**

Compound nr 13	
Chemical formula	C ₂₄ H ₄₂ N ₄ O ₅₀ PW ₁₂
Formula weight	3423.78
Temperature (K)	273(2)
Wavelength	0.71073 Å
Crystal size	0.020 × 0.080 × 0.210 mm
Crystal system	monoclinic
Space group	P 1 2 ₁ 1
Unit cell dimensions	a: 9.737(6) Å α: 90°
	b: 26.169(16) Å β: 103.931(11)°
	c: 14.337(9) Å γ: 90°
Volume (Å³)	3546.(4)
Z	2
Theta data range for collection	2.14 to 28.13°
Index ranges	12 ≤ h ≤ 12, -34 ≤ k ≤ 34, -18 ≤ l ≤ 18
Reflections collected	49681
Independent reflections	17101
Nr. of obs. independent refl; I > 2σ(I)	13023
Final R indices, observed	R1 = 0.0497, wR2 = 0.1172
Final R indices, all data	R1 = 0.0751, wR2 = 0.1289

Table 15. Crystallographic data for structure **14**

Compound nr 14	
Chemical formula	$C_{18}H_{23}N_3O_{24.5}P_{0.5}W_6$
Formula weight	1791.98
Temperature (K)	293(2)
Wavelength	0.71076 Å
Crystal size	0.300 × 0.300 × 0.800 mm
Crystal system	triclinic
Space group	P 1
Unit cell dimensions	a: 9.8759(8) Å α : 65.914(3)°
	b: 14.3510(11) Å β : 76.635(4)°
	c: 14.6921(11) Å γ : 75.416(3)°°
Volume (Å³)	1820.2(3)
Z	2
Theta data range for collection	2.44 to 34.98°
Index ranges	-15 ≤ h ≤ 15, -21 ≤ k ≤ 22, -23 ≤ l ≤ 23
Reflections collected	24187
Independent reflections	19537
Nr. of obs. independent refl; I > 2σ(I)	13164
Final R indices, observed	R1 = 0.0617, wR2 = 0.1364
Final R indices, all data	R1 = 0.1062, wR2 = 0.1564

Table 16. Crystallographic data for structure **15**

Compound nr 15	
Chemical formula	C ₁₈ H ₂₄ N ₂ O ₄₈ PW ₁₂
Formula weight	3273.56
Temperature (K)	295(2)
Wavelength	0.71073 Å
Crystal size	0.020 × 0.020 × 0.100 mm
Crystal system	triclinic
Space group	P -1
Unit cell dimensions	a: 14.516(4) Å α: 79.727(6)°
	b: 14.786(5) Å β: 75.244(7)°
	c: 15.519(5) Å γ: 65.402(6)°
Volume (Å³)	2918.8(15)
Z	2
Theta data range for collection	2.12 to 26.60°
Index ranges	-18<=h<=18, -18<=k<=18, -19<=l<=19
Reflections collected	26319
Independent reflections	11856
Nr. of obs. independent refl; I>2σ(I)	7309
Final R indices, observed	R1 = 0.0708, wR2 = 0.1789
Final R indices, all data	R1 = 0.1233, wR2 = 0.2049

Table 17. Crystallographic data for structure **16**

Compound nr 16	
Chemical formula	C ₁₂ H ₂₀ N ₄ O ₅₀ PW ₁₂
Formula weight	3257.49
Temperature (K)	273(2)
Wavelength	0.71073 Å
Crystal size	0.010 × 0.080 × 0.100 mm
Crystal system	monoclinic
Space group	P 1 21 1
Unit cell dimensions	a: 9.9033(5) Å α: 90°
	b: 26.5990(14) Å β: 90.8930(10) °
	c: 10.0515(5) Å γ: 90 °
Volume (Å³)	2647.4(2)
Z	2
Theta data range for collection	2.17 to 35.13°
Index ranges	-16<=h<=15, -42<=k<=42, -15<=l<=16
Reflections collected	49121
Independent reflections	21811
Nr. of obs. independent refl; I>2σ(I)	15898
Final R indices, observed	R1 = 0.0548, wR2 = 0.1276
Final R indices, all data	R1 = 0.0830, wR2 = 0.1469

Table 18. Crystallographic data for structure 17

Compound nr 17	
Chemical formula	C ₆ H ₁₄ N ₂ O ₇ P _{1.5} W ₁₈
Formula weight	4605.95
Temperature (K)	273(2)
Wavelength	0.71073 Å
Crystal size	0.320 × 0.340 × 0.540 mm
Crystal system	orthorhombic
Space group	C 2 2 2
Unit cell dimensions	a: 16.1458(8) Å α: 90°
	b: 34.5595(17) Å β: 90°
	c: 12.9893(6) Å γ: 90°
Volume (Å³)	7247.9(6)
Z	4
Theta data range for collection	2.52 to 35.11°
Index ranges	-25 ≤ h ≤ 23, -55 ≤ k ≤ 55, -20 ≤ l ≤ 20
Reflections collected	48469
Independent reflections	15371
Nr. of obs. independent refl; I > 2σ(I)	12863
Final R indices, observed	R1 = 0.0463, wR2 = 0.1073
Final R indices, all data	R1 = 0.0603, wR2 = 0.1131

Table 19. Crystallographic data for structure **18**

Compound nr 18	
Chemical formula	C ₂₄ H ₄₄ N ₁₂ O ₅₆ SiW ₁₂
Formula weight	3631.00
Temperature (K)	293(2)
Wavelength	0.71073 Å
Crystal size	N/A
Crystal system	triclinic
Space group	P-1
Unit cell dimensions	a: 10.8473(5) Å α: 99.7051(8)°
	b: 12.4152(5) Å β: 91.9863(9)°
	c: 13.1760(6) Å γ: 103.7460(9)°
Volume (Å³)	1693.76(13)
Z	1
Theta data range for collection	2.837 to 25.024°
Reflections collected	16418
Independent reflections	5757
Nr. of obs. independent refl; I>2σ(I)	5605
Final R indices, observed	R1 = 0.0655, wR2 = 0.1564
Final R indices, all data	R1 = 0.0666, wR2 = 0.1570

Table 20. Crystallographic data for structure 19

Compound nr 19	
Chemical formula	C ₅ H ₉ N ₅ O ₃₆ S ₃ Si ₃ W ₁₂
Formula weight	3101.82
Temperature (K)	293(2)
Wavelength	0.71073 Å
Crystal size	N/A
Crystal system	monoclinic
Space group	P 2 ₁ /c
Unit cell dimensions	a: 32.191(3) Å α : 90°
	b: 14.8183(12) Å β : 91.018(2)°
	c: 15.3532(13) Å γ : 90°
Volume (Å³)	7322.6(11)
Z	4
Theta data range for collection	2.278 to 25.242°
Index ranges	-48<= <i>h</i> <=47, -21<= <i>k</i> <=22, -23<= <i>l</i> <=22
Reflections collected	119465
Independent reflections	25909
Nr. of obs. independent refl; I>2σ(I)	17682
Final R indices, observed	R1 = 0.0744, wR2 = 0.1830
Final R indices, all data	R1 = 0.1114, wR2 = 0.1997

Complexes of Keggin POMs $[PM_{12}O_{40}]^{3-}$ ($M = Mo, W$) with GlyGlyGly and GlyGlyGlyGly Oligopeptides

Björn Greijer,^[a] Timothy De Donder,^[a] Gustav Nestor,^[a] Jan E. Eriksson,^[a]
Gulaim A. Seisenbaeva,^[a] and Vadim G. Kessler^{*[a]}

Complexes of Keggin phosphomolybdate and phosphotungstate anions with tri- and tetra-peptides, GlyGlyGly and GlyGlyGlyGly respectively, were isolated and investigated by single crystal X-ray diffraction, FTIR and SEM-EDS in the solid state and by ¹H- and ³¹P NMR and ESI-MS in solution. The trends

imposed by longer chain length and increased hydrophobicity of the peptide molecules were traced both in binding in the solid state and in effects on solution stability of POMs. Hydrolysis of peptides was observed in strongly acidic solutions at enhanced temperatures in the presence of tungsten POMs.

Introduction

Metal oxide nanoparticles have frequently been shown to have biological relevance,^[1–4] either due to their potential toxicity^[5,6] or their use for drug delivery.^[7] Polyoxometallates (POMs) are a subset of metal oxides which have highly ordered structures, often with one or more central heteroatoms surrounded by heavy metallic addenda atoms. They have garnered much interest in a number of areas, ranging from electronics to medicine (in particular, as underwater adhesives).^[8,9] Among POMs, the Keggin type $PW_{12}O_{40}^{3-}$ was the first structure solved,^[10] and has been the most extensively studied since. The Keggin type POM anion ($XM_{12}O_{40}^{n-}$, $X = P/Si$, $M = W/Mo/V$), being only 1 nm in diameter, is one of the smallest types of metal oxide nanoparticles. This molecular size and appreciable stability in both solid state and solution makes Keggin POMs an attractive model for investigating chemical interactions between metal oxide nanoparticles and molecules possessing important biological functions. There is an appreciable pool of work on how a variety of oligo and mono-peptides interact with POMs.^[11] High electric surface charge of POMs has apparent ability to influence the conformation of large biomolecules. In particular, POMs have been shown to aid in protein crystal formation by forming bridges between charged bodies and stabilizing flexible regions. These interactions vary depending on the protein side chains and can be electrostatic, hydrogen bonds or van der Waals interactions.^[12] Covalent interactions have also been observed.^[13] Due to the small size of POMs they are able to fit into cavities in the proteins and adhere to small charged patches on the protein surface. However, relatively few groups are aiming specifically at obtaining complexes between

POMs and proteins,^[14–17] and many of the POM-containing structures in the Protein Data Bank are, essentially, byproducts of unrelated projects, for example, by being used as phasing tools. Bijelic and Rempel^[12] have previously compiled the available POM-containing structures in the PDB. It is clear that POMs have a place in protein crystallography, though their behavior in contact with biomolecules is at present still relatively poorly understood

We previously reported the structures of Keggin-type phosphotungstate and phosphomolybdate in complex with glycyglycine (GlyGly) dipeptides.^[18] These findings showed that interactions with peptides differ between tungsten- and molybdenum-based POMs, and that POMs complexed with peptides were somewhat protected from degradation by hydrolysis at lower concentrations. Despite the structural and chemical similarity of phosphomolybdate (PMo) and phosphotungstate (PW), their interactions with glycyglycine differed, in that PW mainly formed H-bonds, while PMo had predominantly electrostatic interactions. Here, we intended to investigate whether longer peptide chains will provide further stabilization of POMs. There are results that would suggest that to be the case, as Seixas and colleagues reported spontaneous formation of a Keggin-type phosphomolybdate in a lysozyme crystal soaked in a metalorganic drug containing molybdenum (ALF186).^[19] By studying complexes between POMs and longer peptides, we aimed to get a more realistic model for their possible interactions with proteins. Oligopeptides become less hydrophilic as they grow longer, which may lead to different intermolecular interactions with the same particle. Increased peptide length also provides a larger number of contact points and rotamers, both of which will increase the number of possible binding modes.

Here, we aim to expand on the previous findings by reporting the structures of the industrially available Keggin tungsten and molybdenum POMs in complex with tri- (GlyGlyGly, G3) and tetraglycine (GlyGlyGlyGly, G4).

[a] B. Greijer, T. De Donder, Dr. G. Nestor, Assoc. Prof. Dr. J. E. Eriksson, Prof. Dr. G. A. Seisenbaeva, Prof. Dr. V. G. Kessler
Department of Molecular Sciences, Swedish University of Agricultural Sciences
Box 7015, 75007 Uppsala, Sweden
E-mail: vadim.kessler@slu.se
<https://www.slu.se/en/departments/molecular-sciences/>

Supporting information for this article is available on the WWW under <https://doi.org/10.1002/ejic.202000855>

Table 1. Details of structure collection and refinement for compounds 1–4.

Compound	1	2	3	4
Chemical composition	C ₁₈ H ₂₄ N ₆ O ₃₂ PMo ₁₂	C ₁₈ H ₃₀ N ₆ O ₃₂ PW ₁₂	C ₁₈ H ₂₁ N ₆ O ₆₀ PMo ₁₂	C ₃₂ H ₈₈ N ₁₆ O ₁₄₈ P ₃ W ₃₆
Formula weight	2381.37	3441.02	2497.85	9776.22
Crystal system	Triclinic	Monoclinic	Triclinic	Tetragonal
Space group	P-1	P2 ₁ /n	P-1	P4 ₃ /n
R1	0.0702	0.0482	0.0315	0.0726
wR2	0.1653	0.1270	0.0924	0.1802
a [Å]	11.0479(17)	14.448(6)	14.177(2)	18.991(14)
b [Å]	15.109(2)	10.648(4)	15.405(2)	18.991(14)
c [Å]	18.720(3)	41.167(18)	15.209(2)	25.049(16)
α [°]	102.063(2)	90.00	106.574(2)	90
β [°]	96.441(2)	92.187(6)	101.890(2)	90
γ [°]	97.031(2)	90.00	106.216(2)	90
V [Å ³]	3002(8)	6329(5)	3097(8)	9034(11)
T [K]	296	296	296	296
Z	2	4	2	4
Nr. of obs. Independent refl., I > 2σ(I)	9173	9763	10901	5529

Results and Discussion

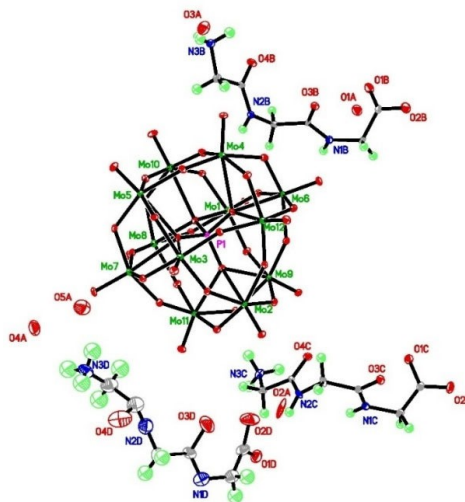
The major difference from recently reported GlyGly derivatives¹⁸ was the need in using more acidic medium (0.1 or 1 M HCl), because of low solubility of tri- and tetraglycine in water at neutral pH. Some of the compounds required different conditions, i.e. lower concentration due to low solubility for G4W (4), or a lower pH for G4Mo (3), both of which formed non-crystalline precipitate in the standard conditions. As this happened to the larger peptide complexes, one might extrapolate that issues may occur should even larger oligopeptides lacking hydrophilic side groups be used. The Mo-containing complexes, G3Mo and G4Mo, were photosensitive and would slowly turn green if not shielded from light, as might be expected based on reports of similar compounds.²⁰

Molecular and crystal structures

Comparing the formally analogous structures of Keggin Mo- and W-POMs is an exciting challenge for nanoscience insights, because these anions are identical from the point of view of colloid chemistry, featuring the same size, shape and total charge, which also results in exactly the same formal charge density on their surface. The difference thus is manifesting only the subtle effects of chemical bonding, revealing the difference in the chemical nature of the POM-forming elements. Using longer chain peptides as cations we were able to observe even more pronounced differences between Mo and W POMs, compared to earlier observations with di-peptide cations.¹⁸ For the G4 peptide even the composition of the precipitating (least soluble) complexes turned different, (HGly₄)₂(H₃O)PMo₁₂O₄₀(H₂O)₉ (3) vs (HGly₄)(H₂O)₂PW₁₂O₄₀ (4). It is worth noting that with tri-peptide cations both POMs are forming complexes with 3:1 cation-to-anion ratio, but with tetra-peptide the compositions are 2:1 (Mo) and 1:1 (W). This can be explained on one hand by the need to use higher acidity in the medium, from which the complexes are crystallizing, and, on the other hand, by the difference in charge distribution, which is more

uniform for the Mo compared to the W derivative.¹⁸ The latter favors electrostatic charge interactions for Mo and stronger network of hydrogen bonding for W compounds. The details of data collection and refinement are summarized in Table 1.

The structure of compound (HGly₃)₃PMo₁₂O₄₀(H₂O)₅ (1) (see Figure 1) is triclinic centrosymmetric, space group P-1, and contains three protonated peptide cations, one phosphomolybdate anion and five water molecules in an asymmetric unit (Figure 1, Figure 5), Z=2 (for details, please, see Table 1). The anion is an α-Keggin construction. The hydrogen bonds form a well-developed network, where the strongest are between the ammonium unit (on N3 atoms in peptide structures) to the interstitial water molecules, N(3D)-O(5A) 2.848(18), and N(3B)-

**Figure 1.** Molecular structure of the (HGly₃)₃PMo₁₂O₄₀(H₂O)₅ (1).

O(3 A) 2.913(18) Å. Next strongest appear the H-bonds between the ammonium units and carbonyl oxygen atoms of the peptides, N(3 C)-O(2D) 2.733(17), N(3B)-O(2 C) 2.843(18), N(3 C)-O(4 C) 2.890(18), N(3B)-O(4B) 2.924(18) Å, where the shortest bond goes to the oxygen atom in the carboxylic acid group. One H-bond of comparable strength per asymmetric unit is observed for a NH amide proton to a bridging oxygen atom in the POM anion, N(1B)-O(15) 2.956(18) Å. The other hydrogen bonds between peptides and the anion are relatively weak (mostly over 3.0 Å in length) and are formed between the ammonium ion unit and the bridging oxygen atoms of the

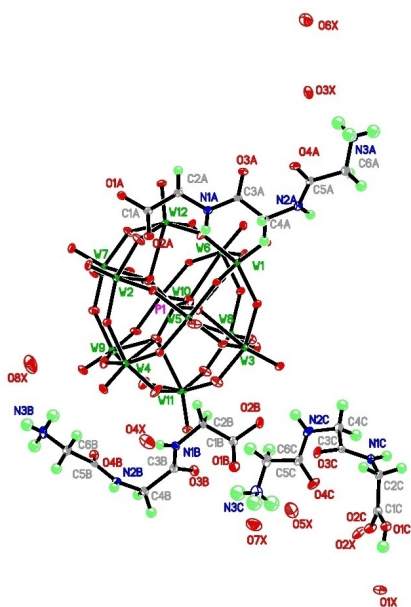


Figure 2. Molecular structure of the $(\text{HGly})_3\text{PW}_{12}\text{O}_{40}(\text{H}_2\text{O})_8$ (2).

POM, N(3 C)-O(32) 2.929(18), and between the ammonium unit and terminal oxygen atoms of the POM, N(3 C)-O(31) 3.007(18) Å, N(3D)-O(40) 3.162(18) Å. The relatively longest H-bonds are between the amide nitrogen atoms in the center of peptide cations and bridging oxygen atoms of the POM, N(2 C)-O(36) 3.068(18), N(2B)-O(17) 3.274(18) and N(2B)-O(16) 3.299(18) Å.

The structure of compound $(\text{HGly})_3\text{PW}_{12}\text{O}_{40}(\text{H}_2\text{O})_8$ (2) (see Figure 2) is centrosymmetric monoclinic, space group P2₁/n, and contains three protonated peptide cations, one phosphotungstate anion, and eight water molecules in an asymmetric unit (Figure 2, Figure 6), Z=4 (Table 1). The anion is an α -Keggin construction. The hydrogen bonding is extensive, with the strongest being between a carboxyl oxygen and an interstitial water molecule, O(1 C)-O(1X) 2.543(15) Å, followed by an ammonium group binding to water N(3 C)-O(7X) 2.734(15) Å. Next strongest are ammonium groups interacting with carbonyl oxygens N(3B)-O(2 A) 2.774(15) Å, N(2B)-O(3 A) 2.815(15) Å, N(3 A)-O(4B) 2.858(15) Å, N(3 C)-O(1 C) 2.859(15) Å or interstitial water N(2 A)-O(2X) 2.851(15) Å, N(1B)-O(4X) 2.868(15) Å, N(3B)-O(8X) 2.985(15) Å, N(3 A)-O(3X) 2.899(15) Å, N(3B)-O(8X) 2.985(15) Å. The next weakest bonds were between amide NH of the peptide and oxygen belonging to the POM anion N(2 C)-O(14) 2.920(15) Å and N(1 C)-O(7) 3.002(15) Å, where the former is a terminal oxygen and the latter is bridging. The longest bonds were between ammonium units of the peptide and terminal oxygen of the POM N(3B)-O(36) 3.023(15) Å, N(3 A)-O(18) 3.065(15) Å, N(3B)-O(11) 3.081(15) Å, N(3 C)-O(26) 3.353(15) Å.

The structure of compound $(\text{HGly})_2(\text{H}_2\text{O})\text{PMo}_{12}\text{O}_{40}(\text{H}_2\text{O})_9$ (3) (see Figure 3) is triclinic centrosymmetric, space group P-1, and contains two protonated peptide cations, one phosphomolybdate anion, and 10 water molecules in an asymmetric unit (Figure 3, Figure 7), Z=2 (Table 1). The anion is an α -Keggin construction. The shortest hydrogen bonds lie between terminal ammonium groups and interstitial water molecules N(4)-O(6 A) 2.741(5) Å or central carbonyl groups of an adjacent peptide N(4 A)-O(5B) 2.780(5) Å, N(4 A)-O(5 C) 2.714(5) Å. Slightly longer are the bonds between a terminal ammonium unit and terminal oxygen on the POM surface N(4 A)-O(31)

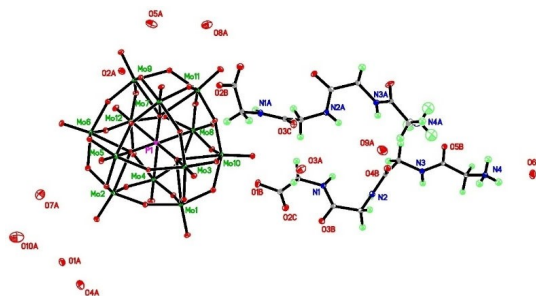


Figure 3. Molecular structure of the $(\text{HGly})_2(\text{H}_2\text{O})\text{PMo}_{12}\text{O}_{40}(\text{H}_2\text{O})_9$ (3).

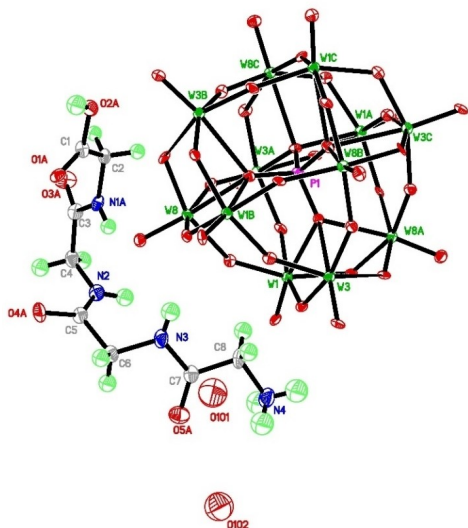
2.903(5) Å and N(4)-O(37) 2.918(5) Å, as well as between an amide NH and water N(3 A)-O(9 A) 2.928(5) Å. The bonds which are around 3 Å lie between an amide NH and water N(2 A)-O(2 A) 3.047(5) Å, and amide NH groups interacting with the POM oxygen N(4)-O(25) 3.043(5) Å, N(4)-O(7) 3.084(5) Å (terminal N, bridging O), N(2)-O(19) 3.083(5) Å, N(3)-O(4) 3.097(5) Å (internal N, terminal O). The relatively weakest interactions are also between peptide NH groups and a mix of terminal and bridging oxygens on the POM surface, N(1 A)-O(14) 3.122(5) Å, N(4)-O(23) 3.139(5) Å, N(1)-O(5) 3.144(5) Å, N(2)-O(16) 3.153(5) Å, N(3)-O(16) 3.238(5) Å, as well as between a terminal ammonium unit and a carbonyl group of an adjacent peptide N(4 A)-O(4B) 3.140(5) Å.

The structure of compound (HGly)₄(H₂O)_{1.33}PW₁₂O₄₀(H₂O) (4) (see Figure 4) is tetragonal centrosymmetric, space group P4₂/n, and contains protonated tetraglycine cations and α-Keggin phosphotungstate anions in 4:3 ratio, and eight (of which five apparently protonated) water molecules/oxonium ions in a formula unit. The asymmetric unit constitutes one fourth of the latter (Figure 4, Figure 8), Z = 2 (Table 1). By far the strongest H-bond in the structure lies between the carboxyl groups of two adjacent peptides O(2 A)-O(1 A) 2.610(40) Å. The carboxyl group is also H-bonded to the terminal ammonium group of an adjacent peptide N(4)-O(2 A) 3.065(40) Å. The remaining hydrogen bonds lie between amide NH groups and terminal surface oxygens of the anion N(4)-O(7) 2.952(40) Å, N(3)-O(8) 3.027(40) Å, N(4)-O(17) 3.044(40) Å, N(3)-O(1) 3.169(40) Å.

The arrangement of the tetraglycine in the two compounds 4 and 3 is quite different. This may be in part due to the different pH used during synthesis but is likely also caused by

the nature of the anions. In 4, the peptide wraps around the POM, while being linked via the carboxyl group to a second peptide, while in 3, it is straighter and makes contact with multiple POM units. Here too, there are contacts between peptides, but those are largely to carbonyl groups. In general, there are more H-bonds per unit cell between the peptide and POM in the structures with phosphotungstate (28 for 2, 24 for 4), than for those with phosphomolybdate (10 for 1, 22 for 3). (Table S1). While there is generally extensive H-bonding between the peptides and water, particularly in 2, there is no H-bonding between water and POM in either structure. However, there appears to be H-bonding between POM particles (ranging from 2.7 to 3 Å, not listed the .lst files), which may imply protonation of the POM.

The packing of POM species in the structures is very distinctly different between the pairs of expected analogs 1 and 2, and 3 and 4 respectively (Figure 5–Figure 8). In the structure of 1 (see Figure 5) the POM-anions are placed largely in agreement with a dense hexagonal packing with cations following the same kind of arrangement. Same principle can be followed even in the structure of 3 (Figure 7). The packing in the structure of 2 (Figure 6) leaves voids in the packing, which are filled with peptide cations, hydrogen bonded to each other and surrounding anions. This type of packing has been observed in the structures of diglycine complexes with W-POMs^[18] and even in complexes of large globular proteins with nanoparticles.^[21] The packing in the structure of 4 (Figure 8) is resembling hexagonal dense packing for the POM anions combined with tetra-peptide cations wrapped around them. The additional oxonium ions disordered together with few



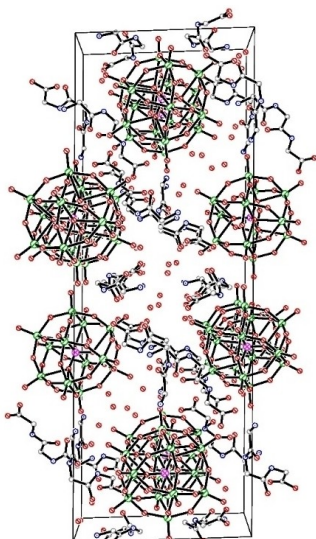


Figure 6. Packing motif in the structure of $(\text{HGly})_3\text{PW}_{12}\text{O}_{40}(\text{H}_2\text{O})_8$ (2).

strongly hydrogen bonded water molecules are expelled to the periphery of hydrophobic voids.

Mass Spectrometry

Mass spectrometry revealed the initial dissociation of complexes on strong dilution (from 50 mM to 50 μM concentration) in agreement with what we observed earlier in the case of free POM acids and also for the complexes with bis-glycine peptide.^[18] However, tri- and tetraglycine appeared to have a more pronounced stabilizing effect on POM nanoparticles

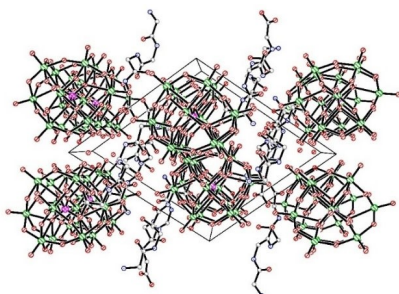


Figure 7. Packing motif in the structure of the $(\text{HGly})_2(\text{H}_2\text{O})\text{PMo}_{12}\text{O}_{40}(\text{H}_2\text{O})_9$ (3).

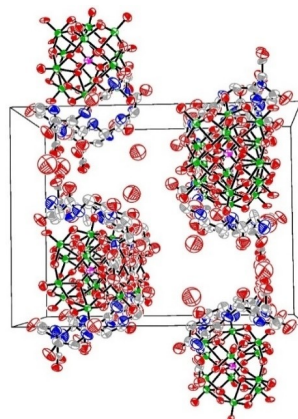


Figure 8. Packing motif in the structure of $(\text{HGly})_{133}(\text{H}_2\text{O})_{167}\text{PW}_{12}\text{O}_{40}(\text{H}_2\text{O})$ (4).

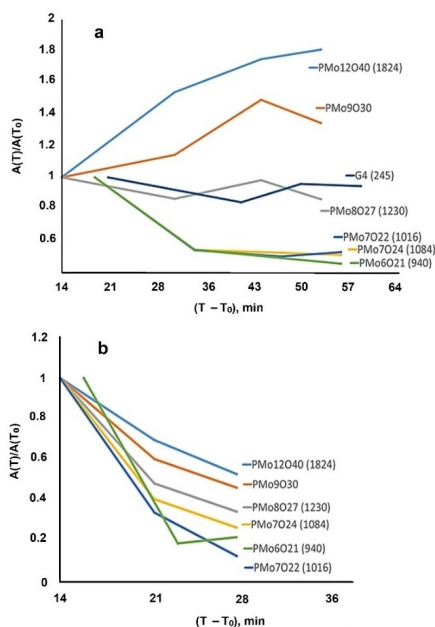


Figure 9. The change in area of selected mass spectrometry signals as a function of time from the moment, when solution was produced (T_0) for (a) Compound 3 and (b) a phosphomolybdate control without peptide. For 3 signal intensities from smaller POM fragments decrease with increasing time, while those from larger fragments increase. In the control, all signal intensities decrease as a function of time.

compared to bis-glycine, as the signal representing the $\text{PM}_{12}\text{O}_{40}^{3-}$ ion retained most of its initial intensity or increased in the course of time (Figure 9). Signals representing ions of breakdown products were observed (Figure S15), as well as ions of free peptides and their dimers and trimers (Figure S16). The decrease of signals from smaller POM fragments and the increase of larger ones as a function of time, suggest that fragments assemble into larger or complete nanosized POM species. This supposition was supported by the observations from mass spectra of a solution of peptide-free POM diluted by 1 M hydrochloric acid. In that case (see Figure 9B) the intensities of both larger and smaller POM fragments decreased with time, indicating dissociation and transformation into most probably positively charged chloride-substituted fragments no longer detectable in the negative charge mode ESI-MS.

NMR Spectroscopy

NMR analysis was performed at 80 °C on **2** and **4** due to low solubility and a drop of concentrated HCl was added to further improve solubility. ^1H spectra showed broad signals, suggesting that the peptide is bound to the complex. Over 90 minutes, signals at 4.09 and 3.92 ppm appeared and increased with time (Figure 10a and Figure S19). These were tentatively assigned to GlyGly, which could be formed by partial hydrolysis of the peptides. In the case of **4**, also signals assigned to triglycine, GlyGlyGly were formed. The same behavior was observed from a sample of tetraglycine without POM anions, which confirms acidic hydrolysis of the peptide at elevated temperature independent of the POM species. In control experiments without POMs under the same conditions the peptide hydrolysis could also be traced. This indicates that the observed hydrolysis is not caused primarily by the catalytic action of POMs but occurs due to common acidic hydrolysis. The measurements for **1** and **3** were run at 40 °C with addition of a drop of 1 M HCl for higher solubility. Also here the ^1H signals were broad, suggesting peptides in complex. No hydrolysis was

observed, but a gradual change towards higher chemical shifts. The chemical shifts of complex-bound tri- and tetraglycine did not differentiate significantly from free peptides in samples without POMs. ^{31}P NMR showed the presence of intact Keggin complexes without any significant degradation (Figure 10b), which is expected at acidic pH.

SEM and EDS

The SEM images (Figure S6) demonstrate well-shaped relatively large rod-like crystals of uniform shape for each sample. The EDS analysis reveals uniform distribution of elements with nitrogen/phosphorus/transition metal ratios corresponding to those expected for formulas of POM complexes obtained from single crystal studies (Supplementary Tables S2–S5).

Vibrational spectra

Characteristic bonding modes were revealed in the FTIR spectra of the obtained complexes (Table 2, Figure S5). All of them contain the typical M=O and M–O–M stretching bands representative of the Keggin phosphometallate anion^[18,22–25] along with a set of bands present in oligo-glycine molecules^[26,27]. The interaction of peptides with POM core species does not lead to stronger line shifts, the most apparent being only the increase in wavenumber value for the N–H band originating from ammonium cations more strongly involved into hydrogen bonds with the anions in W-derived species.

Conclusion

In this study the structure and solution stability of complexes of Keggin POMs with tri- and tetra-glycine peptides has been revealed. The longer peptide chains, compared to earlier investigated di-peptides, led to less hydrophilic molecules with enhanced interactions between the peptide chains and POMs. Even as earlier in the case of dipeptides, no direct structural analogy could be traced between complexes of analogous Mo- and W-POMs. While electrostatic interactions were dominating

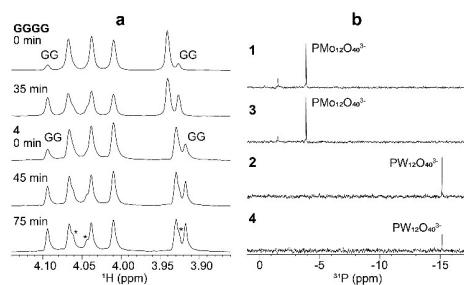


Figure 10. (a) ^1H NMR spectra of free tetraglycine (GGGG) and **4** at 80 °C, pH 0.0. The unlabeled signals correspond to tetraglycine, and the asterisks (*) denote signals tentatively assigned to triglycine after hydrolysis of tetraglycine. (b) ^{31}P NMR spectra of **1**, **3**, **2** and **4** respectively. The most abundant species are indicated.

Bond	1	2	3	4
$\nu(\text{P}=\text{O}-\text{M})$	1063	1063	1080	1080
$\nu(\text{M}=\text{O})$	958	960	979	980
$\nu(\text{M}-\text{O}-\text{M})^{[a]}$	877	879	895	892
$\nu(\text{M}-\text{O}-\text{M})^{[a]}$	795	808	808	808
$\nu(\text{C}=\text{O})$	1728, 1693	1698, 1664	1732, 1692	1726, 1693, 1677
$\nu(\text{CO}_2)_s$	1549	1545	1551	1543
$\nu(\text{CO}_2)_{as}$	1429	1431	1428	1412
$\nu(\text{O}-\text{H})$	3546	–	3556	–
$\nu(\text{N}-\text{H})$	3493	3502	3497	–
$\nu(\text{NH}_3^+)$	3345, 3084	3326, 3129	3363, 3152	3350, 3151

[a] Letter c indicates a bridging oxygen within a metallate triad, d between any two triads.

for the Mo-derivatives, the hydrogen bonding between peptide NH fragments and POMs played more pronounced role for the W-derivatives. An interesting observation was made also for rather pronounced stabilization of POMs in diluted solutions when in complex with tri- or tetra-peptides. While free POM acids are completely hydrolyzed at 50 μM concentration, and complexes with di-peptides retain only a minor fraction of Mo- and W species as POMs, the complexes with tri- and tetra-peptides appear to preserve POM anions as the major fraction.

Experimental Section

Syntheses of compounds. Phosphomolybdic acid, $\text{H}_3[\text{PMo}_{12}\text{O}_{40}] \cdot x\text{H}_2\text{O}$ (CAS, grade), phosphotungstic acid $\text{H}_3[\text{PW}_{12}\text{O}_{40}] \cdot x\text{H}_2\text{O}$ (CAS, grade), bis-glycine (CAS, grade), triglycine (CAS, grade), tetraglycine (CAS, grade) were purchased from Merck and used without further purification. In a standard procedure 0.03 mmol of POM was dissolved in 1 mL 0.1 M HCl and added to a solution of 3 equivalents of peptide dissolved in 1 mL 0.1 M HCl. In the case of G4Mo, 1 M HCl was used as solvent. In the case of 4, a total of 6 mL solvent was used. In the case of 1 and 2, crystals formed within several hours. For 3 and 4, crystals were obtained by slow evaporation of the solvent over several days. All crystals were stable when kept in solution except 1, which degraded into a white precipitate if left in the mother liquor for several days.

Analysis. Single-crystal X-ray diffraction data were recorded with a Bruker D8 SMART APEX II CCD diffractometer (graphite monochromator) with $\lambda(\text{Mo-K}\alpha) = 0.71073 \text{ \AA}$. FTIR spectrometer Perkin-Elmer Spectrum-100 was used for infrared spectroscopy studies. Crystals were milled in paraffin oil and their spectra were recorded by a total of 8–16 scans in 400–4000 cm^{-1} range. SEM-EDS measurements were carried out with Hitachi Flex-SEM-1000 scanning electron microscope.

Crystallography. Single-crystal X-ray diffraction data were recorded at room temperature with a Bruker D8 SMART APEX II CCD diffractometer (operating with graphite monochromated Mo-K α radiation, $\lambda = 0.71073 \text{ \AA}$). The structures were solved by direct methods. Metal atom coordinates were obtained from the initial solutions and the other non-hydrogen atoms by Fourier synthesis. All non-hydrogen atoms were refined first isotropically and then anisotropically in full-matrix approximation. The hydrogen atom positions were calculated geometrically and they were added into the final refinement in isotropic approximation.

NMR Spectroscopy. NMR spectra were acquired on a Bruker Avance III 600 MHz spectrometer using a 5 mm broadband observe detection SmartProbe equipped with z gradient. Samples were dissolved in D_2O with addition of 1 drop of HCl (1 M for 1 and 3, conc. for 2 and 4). Spectra were recorded at 40 °C (1 and 3) or 80 °C (2 and 4) with DSS and water as ^1H chemical shift references. Water suppression of ^1H NMR spectra was achieved with 1D NOESY presaturation. ^1H and ^{13}C resonances were assigned using ^1H , ^{13}C -HSQC and constant-time ^1H , ^{13}C -HMBC experiments. NMR spectra were processed with TopSpin 3.6 (Bruker).

Mass Spectrometry. Negative electrospray ionization mass spectra were recorded with a Bruker Esquire 3000 ion trap mass spectrometer using direct infusion at 3 $\mu\text{L}/\text{min}$. The spectrum acquisition was optimized using the built in target m/z feature together with an automated charge control value of 30000 for 1 and 3, or 15000 for 2 and 4. The spectra were analyzed with the Bruker Compass Data Analysis 4.1 software.

Supporting information (see footnote on the first page of this article): Supporting information includes images of molecular structures with indicated system of hydrogen bonds, FTIR spectra, mass-spectra and electron microscopy images of the reported complexes.

Deposition Numbers 2031299 (1), 2031300 (2), 2031301 (3), and 2031302 (4) contain the supplementary crystallographic data for this paper. These data are provided free of charge by the joint Cambridge Crystallographic Data Centre and Fachinformationszentrum Karlsruhe Access Structures service www.ccdc.cam.ac.uk/structures.

Acknowledgements

The authors express their gratitude to the Swedish Research Council (Vetenskapsrådet) for support to the project 2018–03811, *Molecular Mechanisms in Interaction between Mineral Nanoparticles and Proteins*.

Conflict of Interest

The authors declare no conflict of interest.

Keywords: Oligopeptides · Polyoxometalates · POM-peptide interactions · Tetraglycine · Triglycine




- [1] W. Youn, E. H. Ko, M.-H. Kim, M. Park, D. Hong, G. A. Seisenbaeva, V. G. Kessler, I. S. Choi, *Angew. Chem. Int. Ed.* **2017**, *56*, 10702.
- [2] B. Ekstrand-Hammarström, J. Hong, P. Davoodpour, K. Sandholm, K. N. Ekdahl, A. Bucht, B. Nilsson, *Biomaterials* **2015**, *51*, 58.
- [3] M. P. Monopoli, D. Walczyk, A. Campbell, G. Elia, I. Lynch, F. Baldelli Bombelli, K. A. Dawson, *J. Am. Chem. Soc.* **2011**, *133*, 2525.
- [4] D. Ventura, A. Calderan, C. Honisch, S. Krol, S. Serrati, M. Bonchio, M. Carraro, P. Ruzza, *Pept. Sci.* **2018**, *110*, e24047.
- [5] M. Mahmoudi, H. Hofmann, B. Rothen-Rutishauser, A. Petri-Fink, *Chem. Rev.* **2012**, *112*, 2323.
- [6] M. Mahmoudi, S. Laurent, M. A. Shokrozar, M. Hosseinkhani, *ACS Nano* **2011**, *5*, 7263.
- [7] E. Blanco, H. Shen, M. Ferrari, *Nat. Biotechnol.* **2015**, *33*, 941.
- [8] M. Ammam, *J. Mater. Chem. A* **2013**, *1*, 6291.
- [9] J. Xu, X. Li, X. Li, B. Li, L. Wu, W. Li, X. Xie, R. Xue, *Biomacromolecules* **2017**, *18*, 3524.
- [10] J. F. Keggin, W. L. Bragg, *Proceedings of the Royal Society of London. Series A, Containing Papers of a Mathematical and Physical Character* **1934**, *144*, 75.
- [11] M. Arefian, M. Mirzaei, H. Eshtiagh-Hosseini, A. Frontera, *Dalton Trans.* **2017**, *46*, 6812.
- [12] A. Bijelic, A. Rempel, *Coord. Chem. Rev.* **2015**, *299*, 22.
- [13] J. Schemberg, K. Schneider, U. Demmer, E. Warkentin, A. Müller, U. Ermler, *Angew. Chem. Int. Ed.* **2007**, *46*, 2408.
- [14] A. Bijelic, A. Dobrov, A. Roller, A. Rempel, *Inorg. Chem.* **2020**, *59*, 5243.
- [15] L. Vandebroek, L. Van Meervelt, T. N. Parac-Vogt, *Acta Crystallogr. Sect. C* **2018**, *74*, 1348.
- [16] L. Vandebroek, Y. Mampaey, S. Antonyuk, L. V. Meervelt, T. N. Parac-Vogt, *Eur. J. Inorg. Chem.* **2019**, *2019*, 506.
- [17] L. Vandebroek, E. De Zitter, H. G. T. Ly, D. Conić, T. Mihaylov, A. Sap, P. Proost, K. Pierloot, L. Van Meervelt, T. N. Parac-Vogt, *Chem. Eur. J.* **2018**, *24*, 10099.
- [18] K. M. Rominger, G. Nestor, J. E. Eriksson, G. A. Seisenbaeva, V. G. Kessler, *Eur. J. Inorg. Chem.* **2019**, *2019*, 4297.
- [19] J. D. Seixas, A. Mukhopadhyay, T. Santos-Silva, L. E. Otterbein, D. J. Gallo, S. S. Rodrigues, B. H. Guerreiro, A. M. L. Gonçalves, N. Penacho, A. R. Marques, A. C. Coelho, P. M. Reis, M. J. Romão, C. C. Romão, *Dalton Trans.* **2013**, *42*, 5985.

- [20] Z. Han, E. Wang, G. Luan, Y. Li, H. Zhang, Y. Duan, C. Hu, N. Hu, *J. Mater. Chem.* **2002**, *12*, 1169.
- [21] M. A. Kostainen, P. Hiekkataipale, A. Laiho, V. Lemieux, J. Seitsonen, J. Ruokolainen, P. Ceci, *Nat. Nanotechnol.* **2013**, *8*, 52.
- [22] E. V. Radkov, R. H. Beer, *Inorg. Chim. Acta* **2000**, *297*, 191.
- [23] F. F. Bamoharram, *Molecules* **2009**, *14*, 3214.
- [24] C. Rocchiccioli-Deltcheff, R. Thouvenot, R. Franck, *Spectrochim. Acta Part A* **1976**, *32*, 587.
- [25] E. Rafiee, M. Jashghani, F. Tork, A. Fakhri, S. Eavani, *J. Mol. Catal. A* **2008**, *283*, 1.
- [26] G. Fischer, X. Cao, N. Cox, M. Francis, *Chem. Phys.* **2005**, *313*, 39.
- [27] B. M. Marsh, J. Zhou, E. Garand, *RSC Adv.* **2015**, *5*, 1790.

Manuscript received: September 10, 2020

Revised manuscript received: October 26, 2020

Accepted manuscript online: October 28, 2020

Cite this: *Dalton Trans.*, 2022, 51,
9511Factors influencing stoichiometry and stability of
polyoxometalate – peptide complexes†Björn H. Grejjer, Gustav Nestor,  Jan E. Eriksson, Gulaim A. Seisenbaeva  and
Vadim G. Kessler *

In the pursuit of understanding the factors guiding interactions between polyoxometalates (POMs) and biomolecules, several complexes between Keggin phosphomolybdate and diglycine have been produced at different acidity and salinity conditions, leading to difference in stoichiometry and in crystal structure. Principal factors determining how the POM and dipeptide interact appear to be pH, ionic strength of the medium, and the molar ratio of POM to peptide. An important effect turned out to be even the structure-directing role of the sodium cations coordinating carbonyl functions of the peptide bond. Given the interest in applying POMs in biological systems, these factors are highly relevant to consider. In the view of recent interest in using POMs as nano catalysts in peptide hydrolysis also the potential Keggin POM transformation in phosphate buffered saline medium was investigated leading to insight that nanoparticles of zirconium phosphate (ZrP) can be actual catalysts for breakdown of the peptide bond.

Received 6th March 2022,
Accepted 7th June 2022

DOI: 10.1039/d2dt00717g

rsc.li/dalton

Introduction

Polyoxometallates (POMs) are molecular metal oxide oligomers, generally consisting of tungsten, molybdenum or vanadium oxides, commonly, in their highest oxidation state. Quite a number of different families of POMs have been reported, but in this study we have focused on the Keggin type hetero poly acid $H_n[EM_{12}O_{40}]$ ($E = P, Si$; $M = Mo, W$) involving a central phosphorus atom surrounded by molybdenum oxide triads of edge-sharing octahedra, forming a tetrahedron-shaped construction, a phosphometallate (PM_{12}). These species and their heterometallic derivatives possess spheroidal shape with a diameter of about 1.04 nm, making them attractive as potentially well structurally resolved models of metal oxide nanoparticles (NPs).

Biological activity of small NPs and POMs has recently attracted a lot of attention.^{1–5} There are numerous PDB entries which contain POM ligands,⁶ and modified phosphotungstates have shown great catalytic abilities towards proteins^{7,8} and DNA analogues,⁹ acting as catalysts in hydrolysis of peptide and phosphoester bonds, respectively. It is, therefore, of interest to structurally characterize the interactions between POMs and various biomolecules in detail, in order to identify factors

guiding formation of new structures and determining their activity. This can give insights into the factors guiding biological activity of metal oxide nanoparticles. In particular, the insights into the POMs' interaction with biomolecules has potential to contribute to understanding the phenomenon of formation of the so-called "molecular corona".

Nanoparticles typically form a protein corona,^{10,11} where protein molecules adhere to the surface of the particle. With regard to Keggin POMs, however, their small size (~1 nm diameter) permits treating them as small molecule ligands, which can be directly visualized and provide quantitative information about the chemical bonding. The high negative charge of Keggin POMs allows formation of both electrostatic and hydrogen bonds with proteins targeting positively charged domains on the protein surface. Furthermore, the small size of Keggin POMs allows for interaction limited to small patches as well as fitting into cavities within protein structures.

Because of the POM's strong negative charge, the target in their interactions are thus primarily the positively charged regions. When no such regions exist on a protein, they may be created *via* protonation by lowering the pH and thus opening for new unexpected interactions. Keggin POM $PMO_{12}O_{40}^{3-}$ anions have shown a tendency towards electrostatic interactions with oligoglycines, aside from the H-bonds one would expect.^{12,13} These electrostatic interactions may allow for contacts with uncharged or hydrophobic residues, increasing the versatility in comparison to the more studied PW_{12} species.

The Keggin POM is more stable under low pH,^{14,15} though we have previously demonstrated that oligopeptides have a stabilizing effect on the POM structure.¹² The extent of stabiliz-

Department of Molecular Sciences, Swedish University of Agricultural Sciences, Box 7015, 75007 Uppsala, Sweden. E-mail: vadim.kessler@slu.se

†Electronic supplementary information (ESI) available. CCDC 2151360–2151364 for compounds 2–4 and 6–7 respectively and 2156667 for compound 5. For ESI and crystallographic data in CIF or other electronic format see DOI: <https://doi.org/10.1039/d2dt00717g>

ation is yet undetermined. Vandebroek and colleagues¹⁶ reported a structure of a zirconium-modified Keggin phosphotungstate $[\text{Zr}(\text{PW}_{11}\text{O}_{39})]^{-4}$ in complex with Hen Egg-White (HEW) Lysozyme (HEWL) protein, which was crystallized at neutral pH. Normally, the Keggin phosphomolybdate POM would break down above pH 4–5, depending on the composition,^{14,15} so preserving the intact POM at physiological pH would be highly beneficial in regards to *in vivo* applications. The new species formed reportedly in the course of the synthesis from $(\text{Et}_2\text{NH}_2)_8\{(\alpha\text{-PW}_{11}\text{O}_{39}\text{Zr}(\mu\text{-OH})(\text{H}_2\text{O})_2)\cdot 7\text{H}_2\text{O}$ used as reactant, and was considered as the potentially active species in protein hydrolysis.¹⁶

In our previous study, we have investigated the interaction of Keggin POMs, phosphomolybdic and phosphotungstic acid with diglycine peptide in 1 : 3 ratio and demonstrated that at pH between 3 and 4 the structures differed considerably, indicating stronger electrostatic interactions with Mo-POM and relatively stronger manifested H-bonding with W-POM.¹² We noticed that heating of the reaction mixture led generally to products with lower crystal water contents. Increase in the length of the peptide to tri and tetra-glycine led to products with lower POM-peptide ratios and require lowering of pH for isolation of the products.¹³ We have demonstrated that the pH affected considerably the ability of a complex between tetraglycine and PMo_{12} to form crystals.¹³ This was hypothesized to become possible due to the protonation of the oligopeptide, which would make it stronger positively charged for better electrostatic interaction with POM. This peptide possessed also quite poor solubility under near-neutral pH conditions, which was strongly improved on lowering the pH. In order to ensure that it was fully protonated, the acid concentration was increased considerably, which yielded crystals fit for X-ray diffraction. In this study, we aimed to investigate this phenomenon further, by analyzing crystals derived from solutions with different ratios of diglycine-to-POM, acidity and also salinity.

Results and discussion

Synthesis

In our previous work,¹² where we aimed to compare Mo and W Keggin POM bonding to diglycine, the compounds were prepared by mixing the POM and peptides in a 1 : 3 ratio without addition of acids for pH regulation. This resulted in isolation of compound **1**, $(\text{HGlyGly})_3[\text{PMo}_{12}\text{O}_{40}]\cdot 4\text{H}_2\text{O}$, when the reaction was carried out at room temperature for Mo-POM. Increase in hydrophobicity of a peptide led to decrease in POM : peptide ratio in the isolated products with 1 : 2 for Mo- and just 1 : 1 for W-POM, in spite of 1 : 3 composition in the reaction mixtures.¹³ Here, we aimed to reveal the action of such factors as POM-peptide ratio, salinity and pH on the composition and structure of emerging complexes. Interestingly, changing the ratio of Mo-POM and diglycine did not affect the composition of the complex. When subjecting the solutions with $\text{GlyGly} : \text{PMo}_{12}$ in 1 : 1 and 2 : 1 ratios to crystallization on cooling or solvent evaporation, the primary product that could

be isolated at room temperature, was the earlier described $(\text{HGlyGly})_3[\text{PMo}_{12}\text{O}_{40}]\cdot 4\text{H}_2\text{O}$ (**1**).¹² When the crystals of **1** were removed from solution and the ratio of $\text{GlyGly} : \text{PMo}_{12}$ decreased to less than 0.5 : 1, a new phase appeared denoted as compound **2**, featuring the same composition, but with the structure analogous to that of earlier reported $(\text{HGlyGly})_3[\text{PW}_{12}\text{O}_{40}]\cdot 4\text{H}_2\text{O}$.¹² Heat-treatment of the reaction mixture led for 1 : 1 composition to the complex with the same peptide to POM ratio, but with a doubled unit cell and exact composition $(\text{HGlyGly})_3[\text{PMo}_{12}\text{O}_{40}]\cdot 3\text{H}_2\text{O}$ (**3**), *i.e.* containing less water per asymmetric unit. This change was in line with our earlier observations.¹²

$\text{Na}(\text{HGlyGly})_2[\text{PMo}_{12}\text{O}_{40}]\cdot 8\text{H}_2\text{O}$ (**4**) was obtained in attempt to crystallize iron-substituted POM and titanium substituted POM and can be reproduced, applying simply increased salinity. $\text{Na}(\text{HGlyGly})_2[\text{PMo}_{12}\text{O}_{40}]\cdot 8\text{H}_2\text{O}$ (**5**) was obtained from the titanium containing solution at lower pH. A different form of 1 : 1 complex, not containing any interstitial water molecules, $\text{Na}(\text{HGlyGly})(\text{H}_3\text{O})[\text{PMo}_{12}\text{O}_{40}]\cdot 3\text{H}_2\text{O}$ (**6**), was obtained from the attempt to produce a zirconium-substituted POM (Fig. 1).

The pH of **2** and **3** were approximately 1.2, for **4** pH was 0.6, and for **5** and **6** pH was approximately 0. It appears that pH is a major factor in deciding which structure forms, and how many peptide molecules are found in it. **2** and **3** are also distinct from the previously described structure of diglycine and phosphomolybdate.¹² Though the older structure does contain three peptides, their conformation differ to that of those reported here. The structure of **2**, obtained at lower pH is isomorphous to that of W-POM with more pronounced trend to H-bonding. The effect of pH may be due to the peptides being more, or less, protonated,¹⁷ or the POM being partially lacunary at certain pH.¹⁵ These equilibria may be one reason for the great diversity observed. **3**, **6** and **7** also are obtained in syntheses involving multiply charged metal ions which, while not entering the crystal structures, might contribute to their formation.

The single crystal to bulk identity of products was confirmed by unit cell determination of several randomly chosen single crystals of each compound and also by matching X-ray powder diffractogram of each material to its theoretically calculated powder pattern generated from single crystal structure determination results. The theoretical and experimental powder patterns were in good agreement for all samples.

Crystal and molecular structures

$(\text{HGlyGly})_3[\text{PMo}_{12}\text{O}_{40}]\cdot 4\text{H}_2\text{O}$ (**2**) (Fig. 2) is triclinic centrosymmetric, with the space group *P1*. It contains three protonated diglycine molecules, one phosphomolybdate Keggin anion, and five water molecules in an asymmetric unit, *Z* = 2.

The strongest H-bonds are between water and carboxyl group (2B)–O(4D) 2.717(6) Å and between waters O(1D)–O(7D) 2.705(7) Å. The next strongest bonds are between ammonium units and carbonyl groups N(2A)–O(3B) 2.776(4) Å and N(2B)–O(3C) 2.786(6) Å. Slightly weaker are the bonds between carboxyl groups and water O(1A)–O(5D) 2.795(6) Å and amino groups and water N(2B)–O(1D) 2.810(5) Å and N(2C)–O(2D) 2.861(8) Å as well as bonds between water molecules O(1D)–O

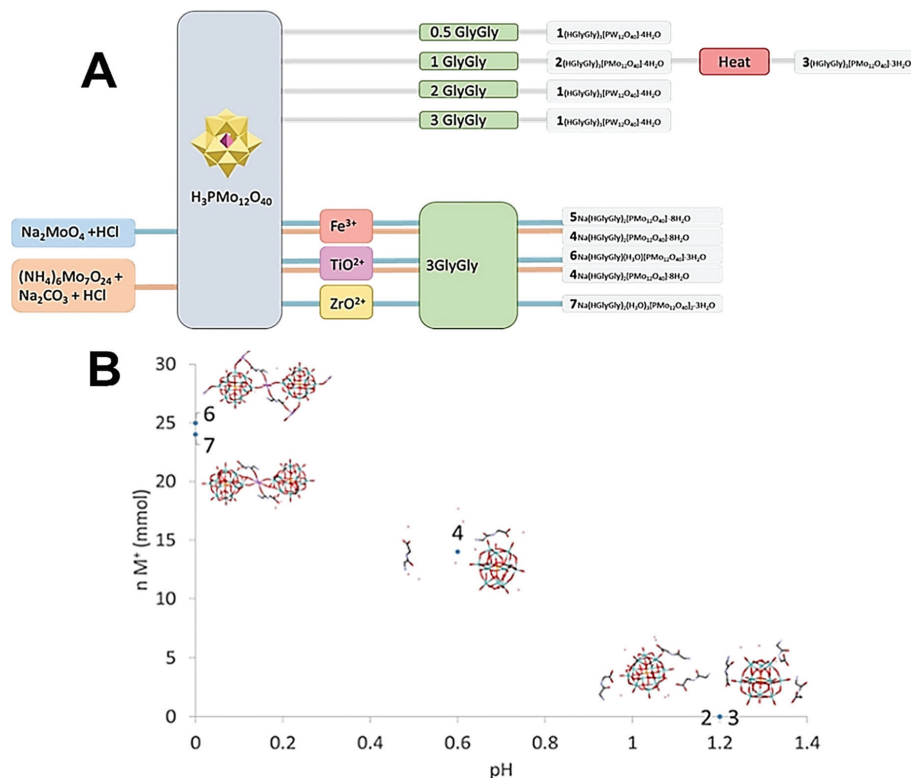


Fig. 1 (A) Scheme of how synthesis conditions yields different crystal structures. (B) Plot of ionic strength of the medium vs. pH for compounds 2–7.

(2D) 2.841(7) Å and O(2D)–O(3D) 2.832(6) Å and bridging oxygen atoms of the POM with water O(5D)–O(12) 2.836(6) Å, carboxyl oxygen O(1C)–O(10) 2.840(6) Å and an amino group N(2B)–O(38) 2.866(5) Å, and between water and carboxyl oxygen O(2D)–O(2A) 2.836(5) Å and between amino group and a carbonyl oxygen N(2A)–O(3A) 2.867(5) Å. Next comes bonds between an amide group and water N(1C)–O(5D) 2.941(7) Å, water and a carbonyl group O(7D)–O(3A) 2.929(8), bridging oxygen on the POM and a water O(7D)–O(40) 2.937(6) Å and an amino group N(2A)–O(32) 2.947(5), terminal oxygen on the POM and a carboxyl group O(1C)–O(22) 2.948(6) Å, an amino group and water molecules N(2C)–O(6D) 2.939(9) Å, and an amide group and a terminal oxygen on the POM N(1A)–O(34) 2.962(4) Å.

The weakest bonds are between water molecules O(7D)–O(4D) 3.028(9) Å, O(6D)–O(5D) 3.038(7) Å, an amino group and a bridging POM oxygen N(2C)–O(33) 3.207(5) Å and an amide group and a carboxyl group N(1B)–O(1C) 3.264(4) Å.

(HGlyGly) $_3$ [PMo $_{12}$ O $_{40}$] \cdot 3H $_2$ O (3) (Fig. 3) is monoclinic, space group $P2_1/n$, with one POM, three diglycine, and three water

molecules in an asymmetric unit, $Z = 4$. The strongest H-bond is between carboxyl and carbonyl oxygen O(2D)–O(3B) 2.571 (20) Å, a carboxyl group and water O(2B)–O(1A) 2.643(10), and corresponding amide groups N(1D)–N(1D) 2.747(30) Å. Next is amino groups with a carboxyl group N(2D)–O(1C) 2.802(30) Å or water N(2C)–O(3A) 2.849(30) Å, N(2C)–O(2A) 2.880(30) Å and between an amino group and a bridging POM oxygen N(2B)–O(16) 2.904(10) Å. Slightly weaker are a number of bonds between amino groups and terminal POM oxygen N(2D)–O(40) 2.948(30) Å, N(2C)–O(22) 3.043(20) Å, N(2B)–O(3A) 3.063(20) Å, N(2B)–O(14) 3.071(10) Å, or bridging POM oxygens N(2B)–O(1) 3.062(10) Å.

Na(HGlyGly) $_2$ [PMo $_{12}$ O $_{40}$] \cdot 8H $_2$ O (4) (Fig. 4) has an orthorhombic space group, $Pbca$, and contains one Keggin POM unit, two diglycine molecules, eight water molecules and a sodium ion in an asymmetric unit, $Z = 8$.

The shortest bonds are between oxygens and the hydrated sodium ion Na(1)–O(1C) 2.341(5) Å, Na(1)–O(1A) 2.346(5), Na(1)–O(40) 2.374(5) Å, Na(1)–O(1B) 2.395(5), Na(1)–O(35) 2.415 (5) Å, Na(1)–O(2A) 2.453(5) Å. The strongest H-bonds are

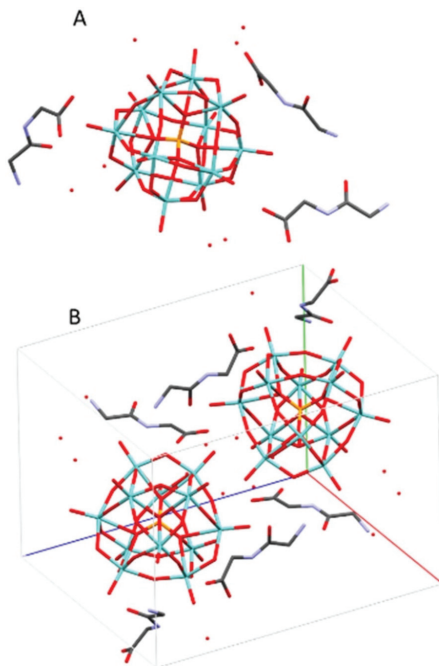


Fig. 2 The molecular (A) and crystal (B) structure of compound $(\text{HGlyGly})_3[\text{PMo}_{12}\text{O}_{40}] \cdot 4\text{H}_2\text{O}$ (2).

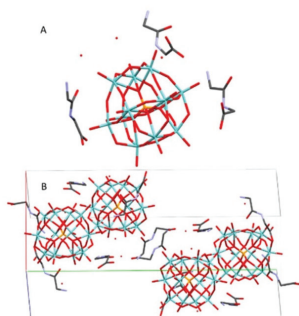


Fig. 3 The molecular (A) and crystal (B) structure of compound $(\text{HGlyGly})_3[\text{PMo}_{12}\text{O}_{40}] \cdot 3\text{H}_2\text{O}$ (3).

between a carboxyl group and water $\text{O}(2\text{C})-\text{O}(5\text{A})$ 2.634(8) Å, and between amino groups and carbonyl groups $\text{N}(2\text{C})-\text{O}(3\text{B})$ 2.729(8) Å, $\text{N}(2\text{B})-\text{O}(3\text{C})$ 2.790(7) Å, which form a ring involving four adjacent diglycine molecules (Fig. S1†). Next, come bonds between water molecules $\text{O}(5\text{A})-\text{O}(7\text{A})$ 2.796(9) Å, $\text{O}(3\text{A})-\text{O}(5\text{A})$ 2.804(8) Å, $\text{O}(4\text{A})-\text{O}(7\text{A})$ 2.833(8) Å, $\text{O}(2\text{A})-\text{O}(3\text{A})$ 2.870(8) Å, water and an amino group $\text{O}(7\text{A})-\text{N}(2\text{C})$ 2.856(8) Å, and

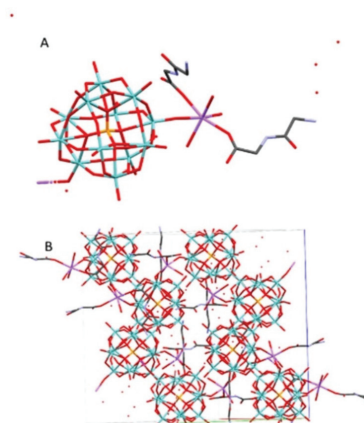


Fig. 4 The molecular (A) and crystal (B) structure of compound $\text{Na}(\text{HGlyGly})_2[\text{PMo}_{12}\text{O}_{40}] \cdot 8\text{H}_2\text{O}$ (4).

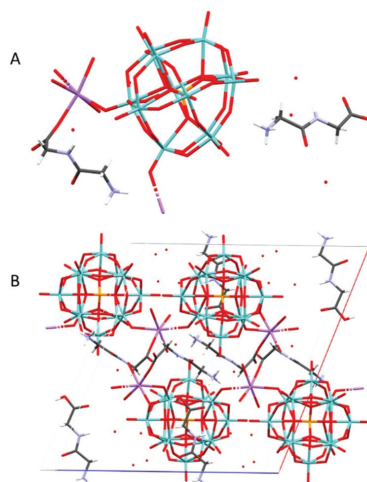


Fig. 5 The molecular (A) and crystal (B) structure of $\text{Na}(\text{HGlyGly})_2[\text{PMo}_{12}\text{O}_{40}] \cdot 8\text{H}_2\text{O}$ (5).

between water and bridging POM oxygen $\text{O}(1\text{A})-\text{O}(29)$ 2.863(6) Å, $\text{O}(3\text{A})-\text{O}(12)$ 2.892(6) Å.

The weakest H-bonds are between amino groups and water $\text{N}(2\text{B})-\text{O}(3\text{A})$ 2.910(10) Å or terminal POM oxygens $\text{N}(2\text{B})-\text{O}(31)$ 2.919(8) Å, $\text{O}(13)-\text{N}(2\text{C})$ 2.966(8) Å.

$\text{Na}(\text{HGlyGly})_2[\text{PMo}_{12}\text{O}_{40}] \cdot 8\text{H}_2\text{O}$ (5) Is monoclinic, space group $P2_1/c$. It contains one α -Keggin POM, two diglycine molecules, one sodium ion and eight water molecules, $Z = 4$ (Fig. 5).

The shortest contacts are between the sodium ion and a carboxyl oxygen $\text{Na}(1)-\text{O}(1\text{C})$ 2.267(6) Å, water $\text{Na}(1)-\text{O}(1\text{A})$

2.337(4) Å, Na(1)–O(4A) 2.344(5) Å, Na(1)–O(2A) 2.418(4) Å, or terminal POM oxygen Na(1)–O(27) 2.535(4) Å, Na(1)–O(14) 2.612(4) Å, and between carboxyl oxygen and water O(2C)–O(8A) 2.636(8), O(2C)–O(2A) 2.689(6) Å. Next are H-bonds between waters O(2A)–O(5A) 2.712(6) Å, O(3A)–O(5A) 2.820(6) Å, carboxyl and amino group O(1B)–N(2C) 2.731(8), bridging POM oxygen and water O(23)–O(1A) 2.797(5) Å, carbonyl oxygen and water O(3B)–O(3A) 2.823(6) Å, and amino and water N(2B)–O(7A) 2.827(6) Å. Slightly weaker H-bonds are between a bridging POM oxygen and water O(11)–O(4A) 2.906(5) Å, amino and water N(2B)–O(3A) 2.918(6) Å, N(2C)–O(1A) 2.938(7) Å, two water molecules O(6A)–O(4A) 2.918(6) Å, bridging POM oxygen and water O(36)–O(2A) 2.935(5) Å, bridging and terminal POM oxygen O(19)–O(10) 2.940(5) Å, terminal POM oxygen and water O(40)–O(5A) 2.988(5), and between carbonyl oxygen and water O(3C)–O(1A) 2.990(5) Å. The weakest H-bonds are between an amino group and a bridging POM oxygen N(2B)–O(12) 3.014(5) Å, amino and carbonyl groups N(2C)–O(3C), Carboxyl group and water O(2C)–O(1A) 3.015(6), bridging and terminal POM oxygen O(30)–O(33) 3.017(5) Å, two terminal POM oxygen O(19)–O(34) 3.021(4) Å, O(40)–O(28) 3.026(6) Å, terminal POM oxygen and water O(14)–O(4A) 3.031(5) Å, and between an amide group and water N(1C)–O(8A) 3.056(6) Å.

Na(HGlyGly)(H₃O)[PMO₁₂O₄₀]₂·3H₂O (6) (Fig. 6) is orthorhombic, space group *Pbcn*, and contains one α -Keggin POM, one diglycine, four water molecules (two of which should actually oxonium ions) and one half sodium ion per asymmetric unit, *Z* = 8.

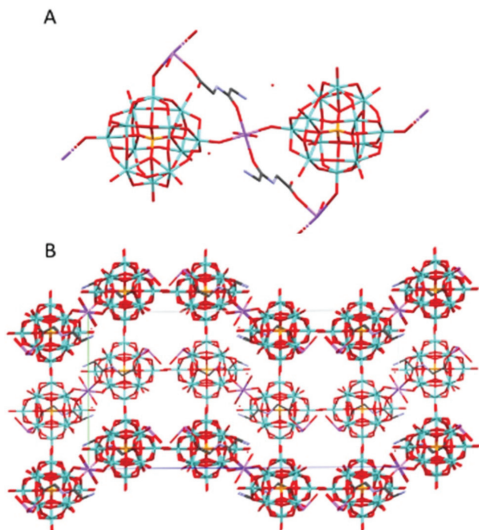


Fig. 6 The molecular (A) and crystal (B) structure of compound Na(HGlyGly)(H₃O)[PMO₁₂O₄₀]₂·3H₂O (6).

The shortest bonds are between a sodium ion and a carboxyl group Na(2)–O(2A) 2.164(20) Å, a carbonyl group Na(1)–O(3A) 2.35(20) Å, water Na(2)–O(4C) 2.41(30) Å, Na(1)–O(2C) 2.33(20) Å, and terminal POM oxygen Na(1)–O(26) 2.319(0) Å, Na(2)–O(38) 2.69(20) Å, Na(2)–O(35) 2.74(20) Å. Next come contacts between an amino group and water N(2A)–O(1C) 2.780(20) Å, N(2A)–O(2C) 2.920(20) Å, two equivalent water molecules O(4C)–O(4C) 2.870(20) Å, water and a bridging POM oxygen O(36)–O(4C) 2.980(20) Å, and water and an amide group O(3C)–N(1A) 2.99(20) Å. The weakest H-bonds are between terminal and bridging POM oxygen O(18)–O(27) 3.01(19) Å, water and a terminal POM oxygen O(1C)–O(30) 3.02(10), water and carboxyl group O(4C)–O(1A) 3.02(20), two terminal POM oxygen O(27)–O(35) 3.03(10) Å, O(31)–O(39) 3.04(10), and a terminal POM oxygen and water O(40)–O(3C) 3.03(20). The dipeptide lies flat against the POM, making contact *via* the sodium ions. The shortest distance between the two is greater than 3 Å, so there does not seem to be any direct interaction in this complex.

Na(HGlyGly)₂(H₃O)₃[PMO₁₂O₄₀]₂·3H₂O (7) (Fig. 7) is monoclinic, space group *P2₁/c*. It contains one α -Keggin POM, one diglycine molecule, one half of sodium ion and three water molecules half of which statistically should be oxonium ions, *Z* = 4.

The strongest H-bonds are between the amino group and water molecules N(2B)–O(2A) 2.795(30) Å and N(2B)–O(1A) 2.899(30) Å. The weaker bonds are around the sodium ion, and connect to a terminal POM oxygen Na(1)–O(20) 2.27 Å, water

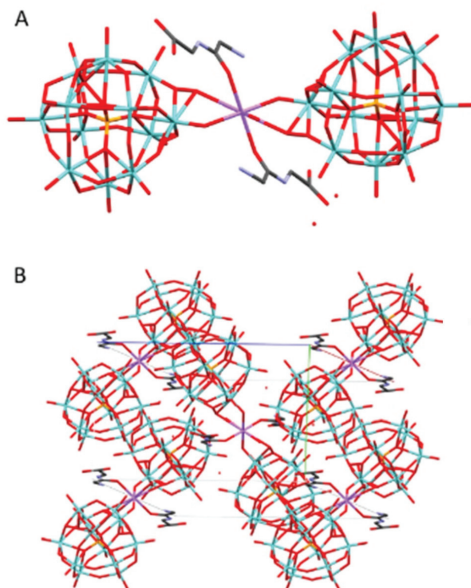


Fig. 7 The molecular (A) and crystal (B) structure of compound Na(HGlyGly)₂(H₃O)₃[PMO₁₂O₄₀]₂·3H₂O (7).

Na(1)–O(1C) 2.37 Å, and a carbonyl group Na(1)–O(3B) 2.38 Å. Next come H-bonds between the amino group and water N(2B)–O(5C) 2.79(30) Å, N(2B)–O(1C) 2.82(30) Å and between the carboxyl group and a terminal POM oxygen O(4)–O(2B) 2.82(30) Å. Then come bonds between the amide group and water N(1B)–O(3C) 2.96(6) Å, amino group and terminal POM oxygen O(20)–N(2B) 2.98(3) Å, a terminal and a bridging POM oxygen O(11)–O(14) 2.99(2) Å, and a terminal POM oxygen and water O(5C)–O(19) 2.99(3) Å. The weakest H-bonds are between the amino group and a terminal POM oxygen N(2B)–O(25) 3.01(30) Å, two terminal POM oxygen O(11)–O(5) 3.01(20) Å and between terminal and bridging PM oxygen O(33)–O(18) 3.02(20) Å, O(35)–O(29) 3.02(29) Å and O(33)–O(36) 3.03(20) Å. The extensive POM–POM contact may imply protonation of the anion. It is worth noting that despite the similarity to 4, it is distinct on a few points. Here we see direct contact between the peptide and POM, as well as less sodium in the structure.

Compound 3–7 were synthesized using sodium salts of molybdenum oxides, and this shows up in the structures. 3 and 4 had relatively less sodium present, and are nearly identical to one another. 6 and 7 contained more sodium, and, while not identical, do appear very similar in the asymmetric unit. 5 appears to be an outlier, as it has a high amount of sodium, but a low amount of peptide in solution, yet resembles 4 more than 6 or 7. As both 4 and 5 involved iron cations in the synthesis, it might also have been a factor that together with the presence of nitrate influences polarity of the media. Nevertheless, the overall trend appear to be that more sodium in the solution means less peptide in the structure. While only diglycine is treated here, and the effect of the various side chains of other amino acids remain to be investigated, it is clear that the presence of sodium ions will interfere with POM-peptide interactions. This is significant, as the presence of sodium is nearly universal in biological systems. Compared to the other structures, the peptides of 3 and 7 appear more disordered (Fig. S4–S9†), though no obvious pattern can be gleaned from this.

Solution behavior

In order to determine whether diglycine has a stabilizing effect on the POM at higher pH, a mixture of PMO₁₂ and diglycine was prepared and brought to pH 6, at which point the solution had

become blue. The main signal in the ³¹P NMR spectra at 2.50–2.52 ppm (Fig. 10G and H) is probably from a lacunary Keggin species on the formula H_xP₂Mo₅O₂₃^{(6–x)–}, which is formed at higher pH (Pettersson *et al.* 1986).²⁴ The blue color may be due to reduced forms of Keggin type POM, which are present in very low concentrations and not observed in the NMR spectrum.

Compound 7 was formed during an attempt to produce Zr-substituted PMo, as has been done with Keggin type phosphotungstate.¹⁸ The zirconium tended to form a precipitate with aggregates of particles 1–5 μm in size (Fig. S15†), which was identified as zirconium phosphate *via* EDS (Fig. S19 and Table S5†). Vanderbroek *et al.*¹⁶ reported a structure of Zr-substituted PW in complex with hen egg white lysozyme (HEWL), however our results imply that under these conditions zirconium may be removed from complexes forming a separate phosphate phase, which in diluted solution was going to be present in nano form. Close analysis of the rather disordered structure published by Vanderbroek *et al.*¹⁶ reveals coordination of the site, interpreted as that of Zr(IV), very unusual for this cation with coordination number 5 and involving the carbonyl oxygen of the protein. The arrangement of Zr(IV) in its complexes in aqueous medium is usually following the Archimedes anti-prism with coordination number 8¹⁹ and in complexes with chelating organic ligands can in some cases feature mono-²⁰ or tricapped²¹ trigonal prism with coordination numbers 7 and 9 respectively. The coordination number 5 is unprecedented in unequivocally determined molecular structures of Zr(IV) in contact with O- and N-donor ligands. In the view that, on one hand, the complexation with peptides appears to enhance stability of Keggin POMs, and, on the other hand, Zr(IV) seems to be removed in the presence of phosphate, it would be plausible to consider a different interpretation of the structure reported by Vanderbroek *et al.*¹⁶ The POM site could rather be occupied by statistically disordered PW₁₂O₄₀^{3–} ions and the lacunary PW₁₁O₃₉^{7–14} ion with predominance of the latter, resulting in a decreased “shady” population of the elusive 12th W-site approximately instead of the electron density of Zr, atomic number 40, instead of W, atomic number 74.

The same group has reported the same ZrPW₁₂ nanoparticles as catalyzing the peptide bond in horse heart myoglo-

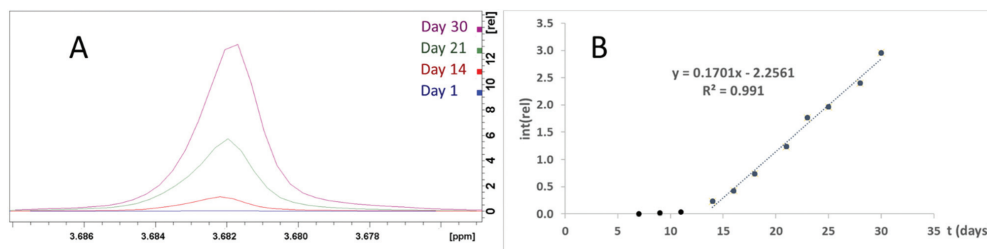


Fig. 8 (A) The glycine signal in NMR spectra of ZrP and GlyGly incubated at 37 °C for 0, 14, 21, and 30 days. (B) Plot of the glycine signal integer normalized to the DSS signal.

bin,²² transferrin,⁸ and dipeptides.²³ Should these catalytic properties be attributed to the Zr–P portion of the ZrPW particle, a pure zirconium phosphate (ZrP) material may display similar abilities. Therefore, we have investigated the catalytic properties of these ZrP particles. Formation of Gly was observed when ZrP was incubated with GlyGly at 37 °C for one week (Fig. S20†), though this was not observed for a similar experiment with tetraglycine. A second experiment was performed where diglycine was incubated with ZrP for 30 days at 37 °C with regular NMR spectra taken (Fig. 8A). Detectable quantities of glycine formed after seven days, and after 14 days, a linear increase in glycine formation was observed (Fig. 8B), implying a zero order reaction with a significant lag phase at the beginning. A control with identical conditions, excluding presence of ZrP, showed no detectable glycine formation.

Thermal analysis

The TGA curves for compounds 1–4, 6, 7 (ESI Fig. S21–S26†) are resembling each other and contain rather distinct steps, corresponding to the loss of interstitial water (below 100 °C), then of water, resulting from condensation of bis-glycine and coordinated to Na⁺-cations (100–200 °C). Then the decomposition of organics occurs in several steps, finishing at about 500 °C. The residue, consisting of MoO₃ and combination of MoO₃ and Na₂MoO₄ volatilizes essentially completely at temperatures over 700 °C.

FTIR

FTIR showed that the characteristic bonds from Keggin phosphomolybdate and diglycine were present in the spectra of the samples (Table 1 and Fig. 9). In the spectra of 6 and 7 only one broad signal was observed for oxygen/nitrogen-proton bonds, which may result from facile proton exchange caused by formation of extensive network of hydrogen bonding as seen in the structures.

Mass spectrometry

2–3 mg of 2 was dissolved in 1 mL water, 0.2 M HCl, or 5 mM phosphate buffer, pH 6.5 and mass spectra were obtained (Fig. 10A–C). In water, the signals corresponding to heavier

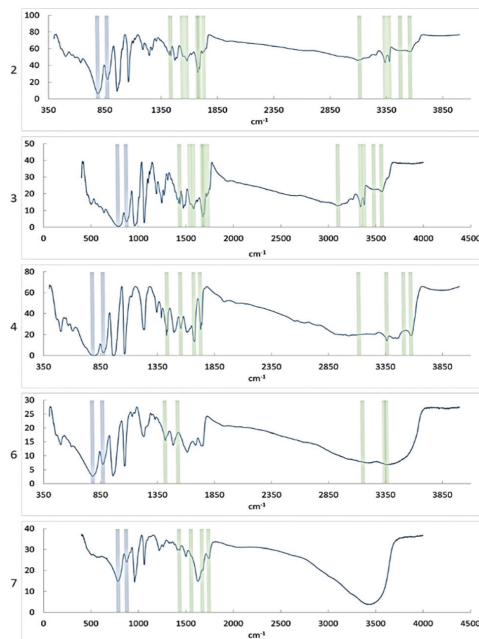


Fig. 9 FT-IR spectra of compounds 2, 3, 4, 6, and 7. Signals corresponding to bonds in the PMo particle are indicated in blue, signals corresponding to diglycine bonds are indicated in green.

compounds are roughly even in intensity, implying a variety of breakdown products in solution. In the sample dissolved in HCl, the signal at 1822 *m/z*, corresponding to the Keggin phosphomolybdate, is dominant, and there appears to be some amount of free molybdate (MoO₄²⁻, 160 *m/z*). In the phosphate buffered sample, the extremes appear subdued, with the most prominent signals appearing between 500 and 1000 *m/z*. This may be due to the high pH destabilizing the heavier forms, while the lighter fragments aggregate onto the phosphate in

Table 1 Selected signals from FTIR analyses of complexes 1–4 and 6–7 (cm⁻¹)

Bond	2	3	4	6	7
$\nu(\text{P-O-M})$	1060	1060	1061	1063	1062
$\nu(\text{M=O})$	968	959	968	960	960
$\nu(\text{M-O}_d\text{-M})$	875	875	876	872	876
$\nu(\text{M-O}_t\text{-M})$	790	787	797	782	786
$\nu(\text{C=O})$	1676, 1691, 1731	1731, 1691, 1676	1675, 1729	1738, 1684	1744, 1676
$\nu(\text{CO}_2)_s$	1544, 1580	1543, 1580	1555	1532	1560
$\nu(\text{CO}_2)_{as}$	1437	1437	1437	1419	1437
$\nu(\text{O-H})$	3560	3561	3574	—	—
$\nu(\text{N-H})$	3477	3482	3511	—	—
$\nu(\text{NH}_3^+)$	3116, 3340, 3377	3370, 3340, 3102	3118, 3362	3361, 3342, 3152	—

(–) indicates absent or poorly resolved peak (s).

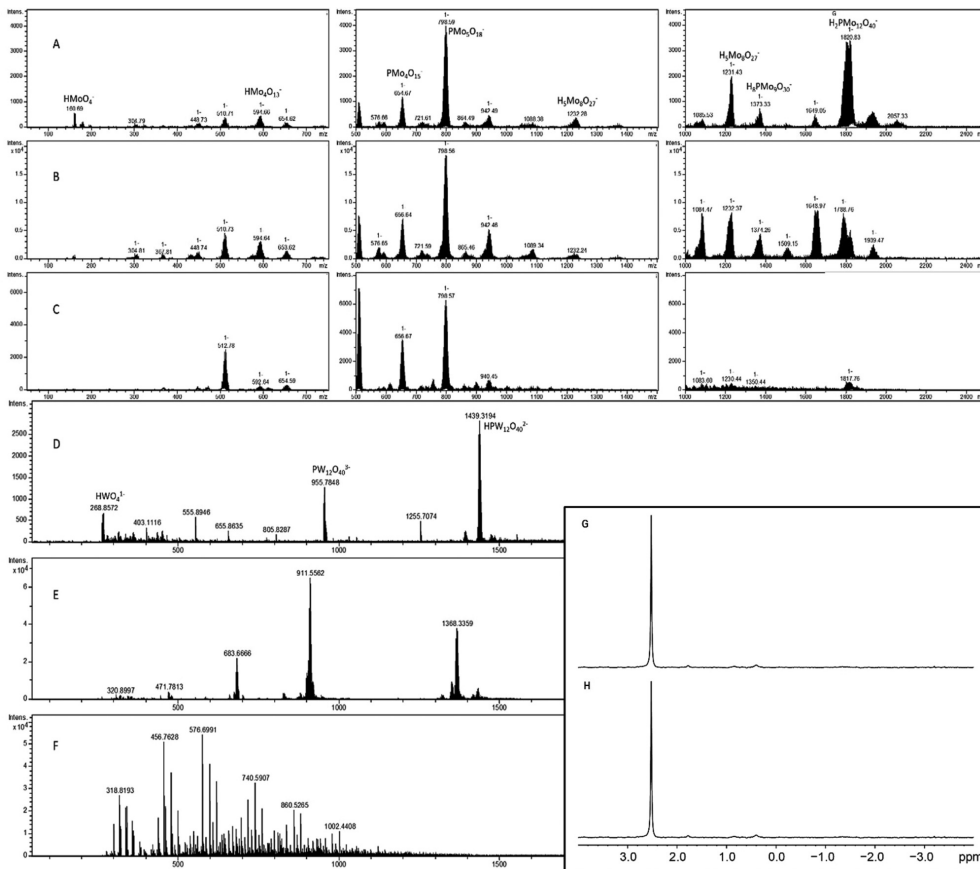


Fig. 10 Mass and NMR spectra of POM-diglycine complexes dissolved in different media. Diglycine-PMo complex (2 : 1) (1.5 mM) **2** was dissolved in (A) 0.2 M HCl, (B) water, and (C) phosphate buffer (5 mM, pH 6.5). Diglycine-PW complex (3 : 1) (14 μ M) dissolved in (D) 0.2 M HCl, (E) water, and (F) phosphate buffer (5 mM, pH 6.5). (G) and (H) ³¹P NMR spectra of phoshomolybdate at pH 6 with diglycine (compound **2**) and without diglycine respectively.

the buffer, which results in mid-weight fragments being more prevalent.

3–5 mg of phosphotungstate – diglycine complex was dissolved in 1 mL water, 0.2 M HCl, or 5 mM phosphate buffer, then diluted one hundred times before collecting mass spectra (Fig. 10D–F). The sample in water shows some amount of double- and triple charged PW anions (1433 and 911 m/z , respectively), as well as the lacunary species [$PW_{11}O_{39}$] (1368 m/z). The sample in acid showed clear signals at 2879 m/z and 1439 m/z corresponding to the complete POM, as well as signals at 955 m/z ($W_4O_{14}^{-2}$) and 268 m/z (WO_4^{-2}). The sample in phosphate buffer displayed no isotope patterns identifiable as W_xO_y species, implying complete hydrolysis of the POM at this high pH and very low concentration.

SEM-EDS

Crystals of complexes were placed on carbon tape fixed on aluminium holders and investigated with Hitachi Flex-SEM 1000 II. Elemental distribution maps were obtained to confirm the chemical homogeneity. The ratio of elements was in all cases matching well the chemical composition obtained from single crystal structure models.

Experimental

Synthesis

All chemicals were analytical grade and used as received from Sigma Aldrich.

Table 2 Details of data collection and refinement for compounds 2–7

Compound	2	3	4	5	6	7
Chemical composition	$C_{13}H_{11}Mo_3N_6O_{16}P$	$C_{13}H_{13}Mo_3N_6O_{16}P$	$C_{13}H_{13}Mo_3N_4NaO_{15}P$	$C_{13}H_{13}Mo_3N_4NaO_{15}P$	$C_{13}H_{13}Mo_3N_2NaO_7P$	$C_7H_5Mo_3N_{12}Na_{0.5}O_{16}P$
Formula weight	2347.76	2365.77	2250.66	2255.63	2065.49	2083.51
Crystal system	Triclinic	Monoclinic	Orthorhombic	Monoclinic	Orthorhombic	Monoclinic
Space group	$P1(2)$	$P2_1/n(14)$	$Pbca(61)$	$P2_1/c(14)$	$Pbcn(60)$	$P2_1/c(14)$
R1	0.0263	0.0494	0.0474	0.0304	0.0544	0.1018
wR2	0.0656	0.1406	0.1377	0.1062	0.1733	0.2341
$\sigma(A)$	12.7308(12)	12.788(2)	17.3441(13)	21.135(3)	12.765(3)	19.443(8)
$b(A)$	13.0510(12)	31.897(5)	23.078(2)	12.9339(16)	19.680(5)	12.745(5)
$c(A)$	18.0332(17)	13.843(2)	25.295(2)	19.455(2)	37.663(10)	19.657(8)
$\alpha(^{\circ})$	97.8970(10)	90.00	90.00	90.00	90.00	90.00
$\beta(^{\circ})$	105.2180(10)	112.173(2)	111.185(2)	105.275(5)	90.00	105.275(5)
$\gamma(^{\circ})$	105.9070(10)	90.00	90.00	90.00	90.00	90.00
$V(A^3)$	2708.8(4)	5228.8(15)	10 124.8(14)	4958.7(11)	9462(4)	4699(3)
$T(K)$	296(2)	296(2)	296(2)	296(2)	296(2)	296(2)
Z	2	4	8	4	8	4
Nr. of obs. independent refl., $I > 2\sigma(I)$	9555	9193	13 401	8333	8333	7421
Residual electron density max	1.086	2.190	1.115	0.754	2.700	0.686

2 was prepared by dissolving 0.03 mmol phosphomolybdic acid hydrate and 0.03 mmol diglycine in 0.5 mL 0.1 M HCl each. The POM solution was added dropwise to the peptide solution, after which it was mixed by inversion. The test tube was left open to let crystals form *via* solvent evaporation. 3 was prepared in a similar manner, but was heated in a water bath after mixing.

4 was prepared by dissolving 1.57 mmol ammonium heptamolybdate and 11 mmol sodium carbonate, which was boiled to remove the ammonia. 1 mmol iron(III) nitrate was dissolved in 2 mL 0.1 M HCl, 1 mmol sodium phosphate dibasic hydrate was dissolved in 2 mL water, and 3 mmol Gly-Gly was dissolved in 2.5 mL water. The phosphate solution was added to the molybdate and concentrated HCl was added until it turned yellow. The resulting phosphomolybdate solution was added to the hot Fe(III) solution dropwise. The Gly-Gly was added, and the solution was allowed to cool slowly. Crystals appeared within hours.

5 was prepared by dissolving 11 mmol sodium molybdate and 1 mmol sodium dihydrogen phosphate in 10 mL water, 1 mmol iron nitrate nonahydrate in 5 mL 1 M HCl, and 1 mmol diglycine in 1 mL 0.1 M HCl. Acid was added to the phosphate and molybdate solution until it became yellow, at which point it was added dropwise to the Fe solution, which turned reddish brown. The diglycine solution was then added and the solution was evaporated by heating in a water bath. Crystals formed upon slow cooling.

6 was prepared by dissolving 11 mmol sodium molybdate and 1 mmol sodium dihydrogen phosphate in 10 mL water, and 1 mmol titanium(IV) oxysulfate in 5 mL concentrated HCl, by vigorous stirring at above 80 °C. HCl was added to the phosphate and molybdate solution until it became yellow (pH 4.8), at which point it was added dropwise to the titanium solution. A white precipitate was formed. Diglycine was added after the PMo, and the solution was slowly cooled to room temperature. Yellow crystals formed after several days, while the solution had become green.

7 was prepared by dissolving 1 mmol sodium dihydrogen phosphate and 11 mmol sodium molybdate in 5 mL water, and adding concentrated HCl until the solution turned yellow. 1 mmol zirconyl chloride octahydrate dissolved in 5 mL water was added to the phosphomolybdate solution, dropwise. A white precipitate was formed. 3 mmol diglycine dissolved in 2 mL 0.1 M HCl was added, and the solution was kept at 70–75 °C for several hours, until it was greenish blue. Blue crystals had formed after several weeks at room temperature.

Analysis

FTIR spectrometer Perkin-Elmer Spectrum-100 was used for infrared spectroscopy studies. Crystals were milled in paraffin oil and their spectra were recorded by a total of 8–16 scans in 400–4000 cm^{-1} range. SEM-EDS studies were performed with Hitach FlexSEM 1000 II instrument supplied by Oxford Instruments EDS analysis system operated by Aztec software.

NMR spectroscopy

NMR spectra were acquired on a Bruker Avance III 600 MHz spectrometer using a 5 mm broadband observe detection SmartProbe. Samples were dissolved in D₂O with DSS as ¹H chemical shift reference and spectra were recorded at 37 °C.

X-ray crystallography

Single-crystal X-ray diffraction data were recorded at room temperature with a Bruker D8 SMART APEX II CCD diffractometer (operating with graphite monochromated Mo-K α radiation, $\lambda = 0.71073$ Å). The structures were solved by direct methods. Metal atom coordinates were obtained from the initial solutions and the other non-hydrogen atoms by Fourier synthesis. All non-hydrogen atoms were refined first isotropically and then anisotropically in full-matrix approximation. The hydrogen atom positions were calculated geometrically and they were added into the final refinement in isotropic approximation. For details, please, see Table 2. Powder X-ray diffraction patterns were registered on Bruker Discover diffractometer with theta-theta Bragg-Brentano geometry using CuK α radiation ($\lambda = 1.54056$ Å) and imaged using CCDC DASH software. Theoretical powder patterns were generated using CCDC Mercury software from the produced cif-files. Good matching between the experimental and theoretical X-ray powder patterns confirmed the identity of the bulk materials with the identified single crystal structures (see Figs. S27†).

Mass spectrometry

Negative electrospray ionization mass spectra were recorded with a Bruker Esquire 3000 ion trap mass spectrometer using direct infusion at 3 $\mu\text{L min}^{-1}$. The spectrum acquisition was optimized using the built in target m/z feature together with an automated charge control value of 30 000 for 1 and 3, or 15 000 for 2 and 4. Negative electrospray ionization mass spectra of PW were recorded with a Bruker maXis impact TOF mass spectrometer under the same electrospray conditions as was the case for 2. The spectra were analyzed with the Bruker Compass Data Analysis 4.1 software.

Conclusion

In the absence of competing cations the PMo₁₂ POM is forming a 1 : 3 complexes with the GlyGly peptide independently of the solution composition. The crystal structure of the products is, however, dependent on the acidity of the applied media, offering a form with enhanced hydrogen bonding isostructural to the earlier described PW₁₂ analog in highly acidic medium. As in the case of earlier described complexes isolated from less acidic media, the intermediate heating is leading to a phase with lower water content. Increased salinity results in incorporation of sodium cations that have a structure-directing role *via* unexpectedly strong coordination of carbonyl oxygen atoms of protonated peptide molecules. This observation is important in the view of abundance of Na⁺ in biological media. Increase in pH to near-neutral values leads to

dissociation of POMs partly stabilized by complexation with peptide. Zirconium cations form under these conditions, in a phosphate buffer, the nanosized zirconium hydrogen phosphate. The latter acts as (micro) heterogeneous catalyst of peptide hydrolysis.

Author contributions

BG performed synthesis of all compounds, contributed actively to structure solution and refinement and produced draft of the manuscript. GN helped with NMR investigation and JE – with MS studies. GS helped with SEM-EDS and FTIR investigation. VK proposed the project, finalized the X-ray structure determinations and supervised the whole study. All authors contributed actively to discussion of the results and editing the final manuscript.

Conflicts of interest

There are no conflicts to declare.

Acknowledgements

The authors are grateful to the Swedish Research Council Vetenskapsrådet for support to the project 2018-03811 Molecular mechanisms in nanoparticle-protein interactions. We express our sincerest gratitude to Dr Fredric Svensson for the aid in registering powder diffraction data.

Notes and references

- 1 W. Youn, E. H. Ko, M.-H. Kim, M. Park, D. Hong, G. A. Seisenbaeva, V. G. Kessler and I. S. Choi, *Angew. Chem., Int. Ed.*, 2017, **56**, 10702–10706.
- 2 B. Ekstrand-Hammarström, J. Hong, P. Davoodpour, K. Sandholm, K. N. Ekdahl, A. Bucht and B. Nilsson, *Biomaterials*, 2015, **51**, 58–68.
- 3 M. P. Monopoli, D. Walczyk, A. Campbell, G. Elia, I. Lynch, F. Baldelli Bombelli and K. A. Dawson, *J. Am. Chem. Soc.*, 2011, **133**, 2525–2534.
- 4 N. I. Gumerova and A. Rompel, *Inorg. Chem.*, 2021, **60**(9), 6109–6114, DOI: [10.1021/acs.inorgchem.1c00125](https://doi.org/10.1021/acs.inorgchem.1c00125).
- 5 L. S. V. Rompuy and T. N. Parac-Vogt, *Chem. Commun.*, 2017, **53**, 10600–10603.
- 6 A. Bijelic and A. Rompel, *Coord. Chem. Rev.*, 2015, **299**, 22–38.
- 7 G. Absillis and T. N. Parac-Vogt, *Inorg. Chem.*, 2012, **51**, 9902–9910.
- 8 L. S. Van Rompuy, N. D. Savić, A. Rodriguez and T. N. Parac-Vogt, *Molecules*, 2020, **25**, 3472.
- 9 S. Vanhaecht, G. Absillis and T. N. Parac-Vogt, *Dalton Trans.*, 2012, **41**, 10028–10034.

- 10 T. Cedervall, I. Lynch, S. Lindman, T. Berggard, E. Thulin, H. Nilsson, K. A. Dawson and S. Linse, *Proc. Natl. Acad. Sci. U. S. A.*, 2007, **104**, 2050–2055.
- 11 M. Lundqvist, J. Stigler, G. Elia, I. Lynch, T. Cedervall and K. A. Dawson, *Proc. Natl. Acad. Sci. U. S. A.*, 2008, **105**, 14265–14270.
- 12 K. M. Rominger, G. Nestor, J. E. Eriksson, G. A. Seisenbaeva and V. G. Kessler, *Eur. J. Inorg. Chem.*, 2019, **2019**, 4297–4305.
- 13 B. Greijer, T. D. Donder, G. Nestor, J. E. Eriksson, G. A. Seisenbaeva and V. G. Kessler, *Eur. J. Inorg. Chem.*, 2021, 54–61, DOI: [10.1002/ejic.202000855](https://doi.org/10.1002/ejic.202000855).
- 14 Z. Zhu, R. Tain and C. Rhodes, *Can. J. Chem.*, 2003, **81**, 1044–1050.
- 15 D. Bajuk-Bogdanović, S. Uskoković-Marković, R. Hercigonja, A. Popa and I. Holclajtner-Antunović, *Spectrochim. Acta, Part A*, 2016, **153**, 152–159.
- 16 L. Vandebroek, L. Van Meervelt and T. N. Parac-Vogt, *Acta Crystallogr., Sect. C: Struct. Chem.*, 2018, **74**, 1348–1354.
- 17 K. Niwa, S. Toda, K. Fuwa and H. Haraguchi, *Agric. Biol. Chem.*, 1977, **41**, 1287–1294.
- 18 M. N. Sokolov, E. V. Chubarova, E. V. Peresyphkina, A. V. Virovets and V. P. Fedin, *Russ. Chem. Bull.*, 2007, **56**, 220–224.
- 19 C. Hagfeldt, V. Kessler and I. Persson, *Dalton Trans.*, 2004, 2142–2151.
- 20 V. G. Kessler, G. I. Spijksma, G. A. Seisenbaeva, S. Håkansson, D. H. A. Blank and H. J. M. Bouwmeester, *J. Sol-Gel Sci. Technol.*, 2006, **40**, 163–179.
- 21 G. I. Spijksma, L. Kloof, H. J. M. Bouwmeester, D. H. A. Blank and V. G. Kessler, *Inorg. Chim. Acta*, 2007, **360**, 2045–2055.
- 22 H. G. T. Ly and T. N. Parac-Vogt, *ChemPhysChem*, 2017, **18**, 2451–2458.
- 23 H. G. T. Ly, G. Absillis and T. N. Parac-Vogt, *Dalton Trans.*, 2013, **42**, 10929–10938.
- 24 L. Pettersson, I. Andersson and L. O. Öhman, *Inorganic Chemistry*, 1986, **25**, 4726–4733.

Functional Nanostructures from Sol–Gel Synthesis Using Keggin Polyoxometallate Phosphotungstic Acid as a Precursor

Björn Greijer, Wannes De Turck, Geoffrey Daniel, Jayeeta Saha, Mats Johnsson, Gulaim A. Seisenbaeva, and Vadim Kessler*

Cite This: *Inorg. Chem.* 2024, 63, 3428–3435

Read Online

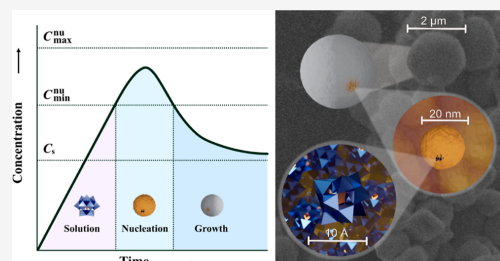
ACCESS |

Metrics & More

Article Recommendations

Supporting Information

ABSTRACT: Subjecting phosphotungstic acid solutions to low pH in combination with introduction of polyvalent cations led to the formation of nanostructured microspheres of approximately 2 μm in size, as shown by scanning electron microscopy, which were almost insoluble and resistant to degradation at neutral and high pH. These microspheres were composed of secondary nanospheres with diameters around 20 nm as revealed by transmission electron microscopy and atomic force microscopy. Investigations of the crystal structure of a potential intermediate of this process, namely, acidic lanthanum phosphotungstate, $[\text{La}(\text{H}_2\text{O})_9] \cdot (\text{H}_3\text{O})_3[\text{PW}_{12}\text{O}_{40}]_2(\text{H}_2\text{O})_{19}$, showed a tight network of hydrogen bonding, permitting closer packing of phosphotungstic acid anions, thereby confirming the mechanism of the observed self-assembly process. The new material demonstrated promising electrochemical properties in oxygen evolution reactions with the high stability of the obtained electrode material.



INTRODUCTION

The internationally recognized goal to reduce evolution of greenhouse gases has set focus on the development of efficient fossil-free technologies for energy production.¹ The main source of usable energy for the earth is solar light and thus solar energy conversion is one of the most addressed topics in modern research in designing and producing new materials.^{2,3} An attractive alternative to fossil fuel-based processes is hydrogen energy, primarily the production of electricity with the aid of fuel cells,⁴ but also the use of hydrogen in reduction reactions such as the recently proclaimed HYBRIT technology for “green synthesis” of steel from iron ore.⁵ A common feature of hydrogen energy technologies is the need for high-purity hydrogen gas required in large volumes. Its production is possible either via costly purification of hydrogen obtained via the water–gas shift reaction from natural gas or biogas⁶ or via highly energy-demanding electrolytic water splitting.⁷ An attractive alternative to electrolysis is the use of photocatalytic or electrocatalytic water decomposition. In these approaches, the energy costs for hydrogen gas can be significantly reduced while not compromising its quality. The challenge, however, lies in the need for expensive components used in the making of such catalysts. Typical photocatalysts for water splitting are nanoparticles (NPs) of semiconductor oxides or chalcogenides in combination with noble metals.⁸ The efficient electrocatalysts applied so far also commonly contain platinum group metal-based NPs either as oxides (RuO_2^9 or IrO_2^{10}) or

together with platinum NPs.¹¹ The development of noble metal free photo- and, especially, electrocatalysts is an important and highly addressed research target.¹

An attractive candidate for the photo- and electrocatalyst in water splitting [i.e., oxygen evolution reaction (OER)] is pure^{12–16} and chemically doped^{17–19} tungsten oxide along with closely related nanocomposite heterostructures.^{20–23} The challenge in the creation of such related nanostructures is the relatively high reactivity and solubility of WO_3 and its derivatives in both acidic and basic media.^{24,25} Here, in particular, phosphotungstic acid has attracted attention as a possible photocatalyst^{26,27} and potentially electrocatalyst²¹. However, this compound in its hydrated form is highly soluble in water, which hinders its application.

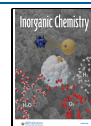
Phosphotungstic acid is a well-studied representative of the polyoxometallate (POM) family of compounds. It is of the Keggin type, the smallest metal oxide nanoparticle of approximately 1 nm in diameter, which has a highly ordered structure consisting of a central heteroatom inside a cage of 12 transition metal atoms in their highest oxidation state, all

Received: November 21, 2023

Revised: January 18, 2024

Accepted: January 23, 2024

Published: February 7, 2024



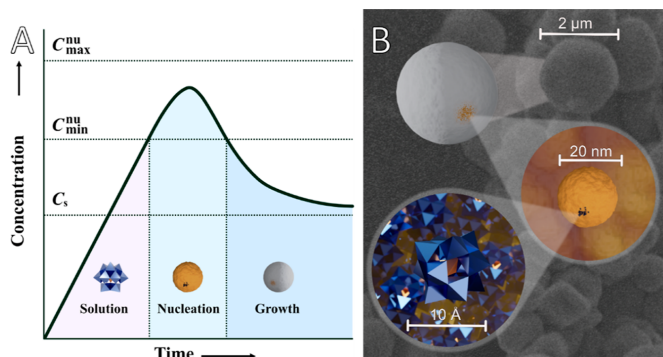


Figure 1. Hierarchical assembly of phosphotungstate spheres by the sol–gel process, illustrated in relation to the La Mer concept graphically (A) and structurally (B). Individual POMs aggregate to form nanoparticles approximately 20 nm in diameter, which in turn assemble into ternary particles of up to approximately 2 μm in diameter.

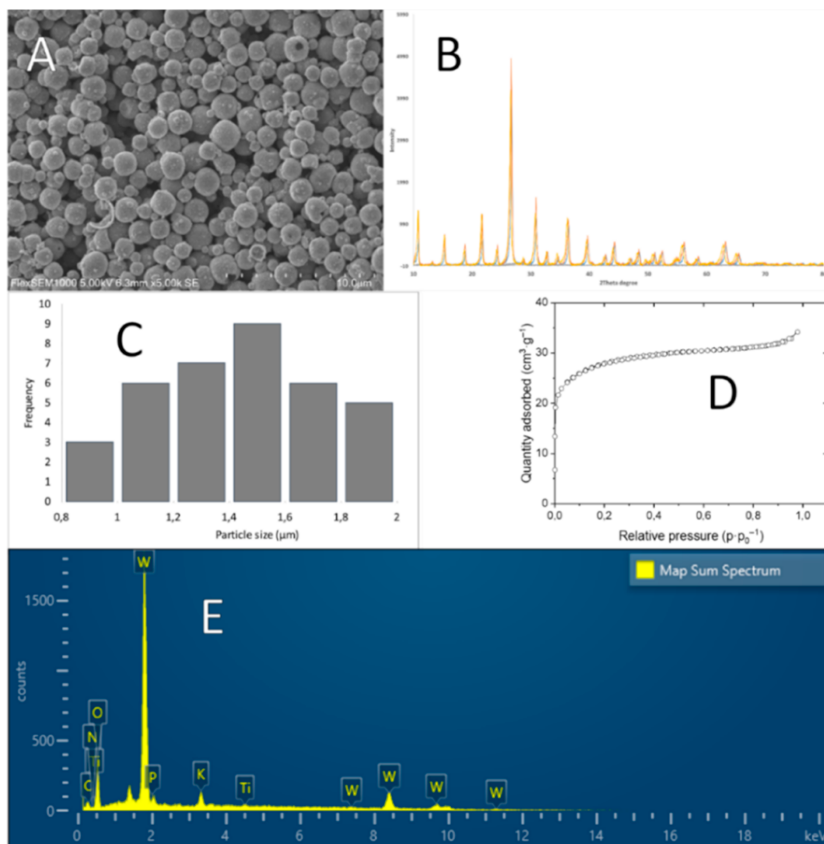


Figure 2. (A) SEM image of the Ti-derived spheres at 5000× magnification. (B) XRPD pattern of the spheres. (C) Size distribution of the particles in A ranges from 0.8 to 2 μm, with an average of 1.4 μm. (D) Nitrogen adsorption/desorption isotherms for PW NPs. (E) EDS spectrum of the spheres. Tungsten and oxygen were the most abundant, while traces of potassium and titanium were also detected.

connected by oxygen bridges, giving the general formula $\text{XM}_{12}\text{O}_{40}^{z-}$ ($X = \text{P, Si, Ge, As, Sb}$; $M = \text{W, Mo}$; $z = 3$ or 4).

We have previously reported complexes of Keggin POMs and oligopeptides, in an effort to model the interactions between NPs and proteins at the nanoscale.^{28,29} Some of these complexes displayed POM–POM contacts, approximately 3 Å in length, likely resulting from hydrogen bonds. As these were observed at very low pH, protonation of the POM likely shielded the charge, allowing for direct interactions. Acidic conditions are necessary when working with Keggin POMs, as one drawback of phosphotungstic acid, in particular, is its instability at neutral and alkaline pH.^{24,25} Thus, retaining POM intact at a higher pH could potentially strongly expand its suitability as a catalyst.

In the present study, we utilized the Keggin POM as a precursor in a sol–gel process. The sol–gel is a process where separation of a solid phase, usually metal oxide, from solution occurs via nucleation in the form of NP species resembling POMs. This creates a colloid solution (i.e., sol), allowing subsequent aggregation without growth, forming a colloid solid – gel.³⁰ The Keggin POM species appear to act as such NPs and self-assemble into secondary particles, analogous to self-assembled particles formed by a sol–gel. The process can be described through a La Mer diagram,³¹ illustrated by a graph in Figure 1A. The conditions required for their formation in this case appear to be highly acidic media, heat, and the presence of polyvalent cationic species in addition to the POM opening for neutralization of the POM charge and subsequent aggregation. Using this approach, we were even able to isolate and characterize a chemically individual intermediate in this self-assembly process—a lanthanum salt of POM. The produced hierarchical self-assembled POM structures were extremely poorly soluble under acidic and neutral conditions and demonstrated exceptional stable activity in electrochemical water splitting.

RESULTS AND DISCUSSION

In a recent study, we found that increasing acidity and ionic strength (cation concentration) in solutions of Keggin POMs together with peptides resulted in the formation of compounds with lower peptide-to-POM ratios, where metal cations and, most importantly, oxonium ions became incorporated into the resulting structures.³² Highly charged cations facilitated formation of “acidic” POM derivatives that are usually included in the composition of the product. In the present study, we attempted to use extremely acidic conditions with $\text{pH} < 0$ and relatively high concentrations of highly charged cations such as Ti(IV) , Zr(IV) , Ce(IV) , and La(III) on heating with continuous stirring. As expected, this approach resulted in all cases in hierarchical self-assembly of POMs with formation of spherical aggregates several micrometers in size. The analysis of the particles showed a hierarchical structure with three levels of organization (Figure 1). First, the POM “nuclei” make contact at similar distances via hydrogen bonds. Second, nanospheres made from POMs of approximately 20 nm in diameter are formed. Third, assemblies of these nanospheres form ternary particles of up to 2 μm in diameter.

Scanning electron microscopy (SEM) images revealed spherical particles ranging from 500 nm to 2 μm in diameter (Figure 2A). A typical size distribution for Ti(IV) -derived material (i.e., nanospheres/particles) is shown in Figure 2C. Debris of broken spheres were present in the unwashed samples. EDS analysis showed mainly tungsten, with traces of

the metal cations present during synthesis, such as titanium and potassium (Figure 2E and Table TS1).

X-ray powder diffraction (XRPD) of freshly obtained materials was consistent with the known pattern of hydrated Keggin-type phosphotungstic acid $\text{H}_3\text{PW}_{12}\text{O}_{40}\cdot 21\text{H}_2\text{O}$ (Figure 2B).³³ Drying of the samples resulted in broadening of the peaks and weakening of the peak intensity, with a fully X-ray amorphous product on longer storage. These transformations were likely caused by the loss of water molecules from the material that became amorphous while preserving the overall morphology at all levels.

The nitrogen adsorption/desorption isotherms for the PW NP sample are shown in Figure 2D. The shape of the isotherms corresponds to characteristic type I, typical of microporous solids having relatively small external surfaces, the limiting uptake being governed by the accessible micropore volume rather than by the internal surface area.³⁴ The Brunauer–Emmett–Teller specific surface area (S_{BET}) was found as 100.6 $\text{m}^2\cdot\text{g}^{-1}$ and the Langmuir surface area was found as 125.9 $\text{m}^2\cdot\text{g}^{-1}$ for the PW NP sample. The Barrett–Joyner–Halenda desorption cumulative surface area and volume of pores between 1.7 and 300 nm were 23.0 $\text{m}^2\cdot\text{g}^{-1}$ and 0.019 $\text{cm}^3\cdot\text{g}^{-1}$ (corresponding to 8.75 vol % of pores), respectively.

Atomic force microscopy (AFM) investigations showed that the spheres were made up of fairly uniform secondary particles (Figure 3), although larger than individual POMs, which are

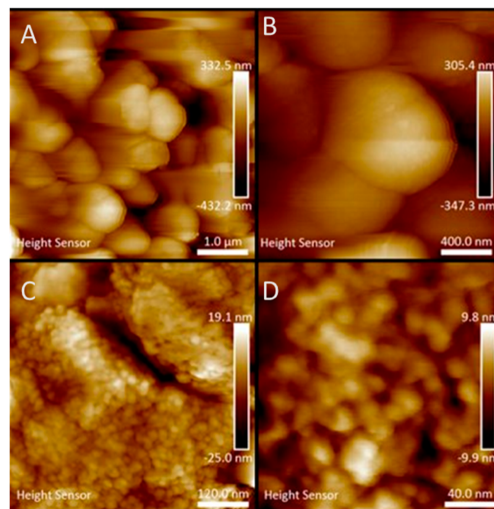


Figure 3. AFM images of the spheres. Particles in the micrometer range (A,B) can be seen at low magnification and their nanosized composition at high magnification (C,D).

primary ones in this sol–gel process, analogues of what in metal–organic sol–gel are called micelles templated by the self-assembly of ligands (MTSALS).^{35,36} This implies, at the first step, aggregation of the Keggin POMs in the tens of nm size, which then form a tertiary aggregate in the μm range. The secondary particles, as shown from the X-ray diffraction (XRD) data, were originally formed as crystallites of the $\text{H}_3\text{PW}_{12}\text{O}_{40}\cdot 21\text{H}_2\text{O}$ phase. Their growth, however, is appa-

rently impeded by adsorption of highly charged cations on their surface, which drastically decreases solubility of the material and permits aggregation of these secondary particles.

The hierarchical composition of the spheres was also observed under transmission electron microscopy (TEM), where tertiary spheres of approximately $2 \mu\text{m}$ across (Figure 4A) are made up of secondary spheres in the tens of nanometers in diameter (Figure 4B,C) that are presumably composed of individual units of hydrated phosphotungstic acid.

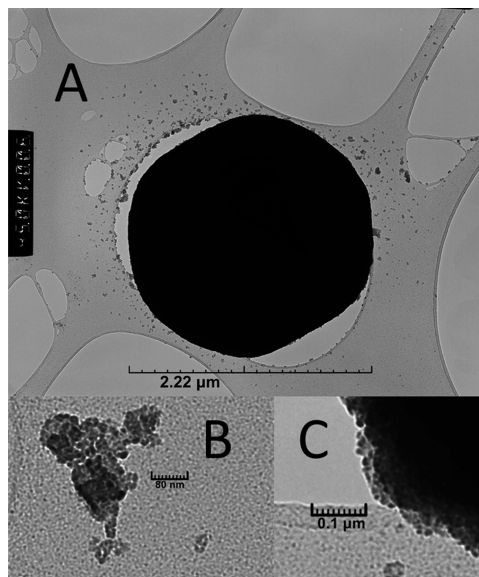


Figure 4. TEM image of the spheres. The large tertiary particle (A) is made up of secondary particles of nanosize (B,C).

Similar structures, made of potassium phosphotungstate, have been reported by Yan et al.,^{26,37} although these were produced by simple coprecipitation through dropwise addition of KCl solution to a POM solution. The latter were significantly smaller and singular in composition and structure rather than the hierarchical structure observed in this work. It can be speculated that they were formed by the action of analogous driving forces with their ground in charge compensation of the POM structural units. The cation content and the solubility, crucial for the application as stable electrocatalysts, are, however, drastically lower in the new material reported here.

The thermal stability of the produced material was investigated via both thermogravimetric analysis (TGA) (Figure S1) and by preparative experiments. The weight loss occurred in several steps in the interval $120\text{--}500\text{ }^\circ\text{C}$, being associated initially with the loss of the different forms of water content. Elemental analysis of the residues showed that the ratio of W to P did not vary significantly in the samples taken at different temperatures ($\sigma = 0.78$), and thus, no loss of the phosphorus content could be observed.

For dynamic light scattering (DLS) and zeta potential, three measurements were taken using distilled water as a medium,

and the mean and standard deviation are shown in Supporting Information Table TS2. As the particles were fairly large, the standard deviation of the zeta potential was near 5 in all cases.

Single-Crystal X-ray Structure of the Isolated Intermediate. Crystals isolated from the synthesis using La(III) nitrate were triclinic centrosymmetric with a $P\bar{1}$ space group, containing two phosphotungstate anions, one lanthanum ion, and 31 water molecules in an asymmetric unit, $Z = 2$ (Figure 5,

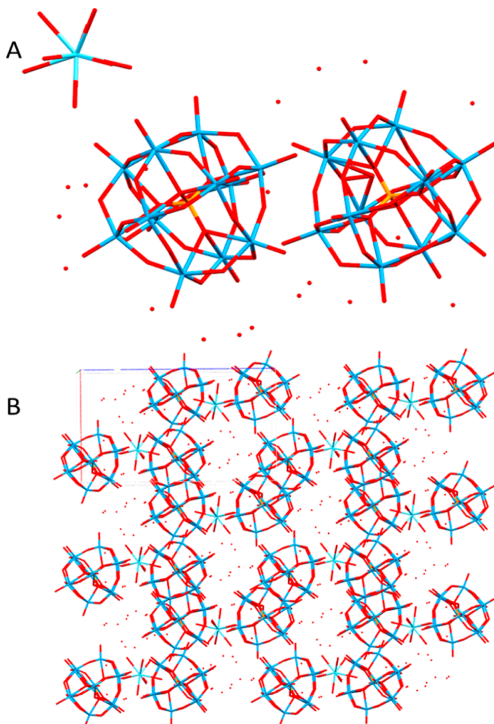


Figure 5. Asymmetric unit (A) and packing (B) of the phosphotungstic acid crystals of acidic lanthanum phosphotungstate, $[\text{La}(\text{H}_2\text{O})_9](\text{H}_3\text{O})_3[\text{PW}_{12}\text{O}_{40}]_2(\text{H}_2\text{O})_{19}$. Numerous cavities filled with water molecules are seen as well as close contacts between POMs.

Table 1). The composition of the material can thus be formulated as $[\text{La}(\text{H}_2\text{O})_9](\text{H}_3\text{O})_3[\text{PW}_{12}\text{O}_{40}]_2(\text{H}_2\text{O})_{19}$. The large amount of water forms an extensive hydrogen bonding network throughout the crystal. The shortest contacts lie between water at 2.16 and 2.7 Å. At a bond length of 2.7–2.8 Å, contacts exist between both water molecules and water to bridge POM oxygen. Between 2.8 and 2.9 Å, there are a number of bonds mainly between water and between water and terminal POM oxygen. In this range, there are also contacts between water and bridging POM oxygen, as well as POM–POM contacts. The longest contacts above 2.9 Å lie between water, POM oxygen and water, or two adjacent POMs.

The extensive contacts between POMs suggest that they are protonated at this pH (Figure S2), allowing for hydrogen

Table 1. Details of Data Collection and Refinement for the Phosphotungstate–Lanthanum Structure⁴

chemical formula	H ₆₃ LaO _{113.50} P ₂ W ₂₄
formula weight	6494.77 g/mol
temperature	163(2) K
wavelength	0.71073 Å
crystal size	0.160 × 0.200 × 0.320 mm
crystal system	triclinic
space group	P $\bar{1}$
unit cell dimensions	$a = 14.008(3)$ Å $\alpha = 88.978(5)^\circ$ $b = 15.140(3)$ Å $\beta = 89.228(4)^\circ$ $c = 22.386(5)$ Å $\gamma = 80.885(5)^\circ$
volume	4686.7(18) Å ³
Z	2
theta range for data collection	2.26 to 28.00°
index ranges	$-18 \leq h \leq 18$, $-19 \leq k \leq 19$, $-29 \leq l \leq 29$
reflections collected	57 188
Independent reflections	22 324 [R(int) = 0.0652]
No. of observed independent reflections; $I > 2\sigma(I)$	17 582
final R indices, observed	R1 = 0.0596, wR2 = 0.1531
final R indices, all data	R1 = 0.0787, wR2 = 0.1630

⁴Details of data collection and refinement can be obtained free of charge from the Cambridge Crystal Structure Database at <https://www.ccdc.cam.ac.uk/structures/citing>, deposition no. CSD-2307589.

bonding between the POMs. Though the protons are not visible in the structure, the bond distances are consistent with H-bonds. Similar phenomena have been observed with phosphomolybdic acid previously.²⁹ The water molecules participate mostly in four hydrogen bonds per molecule, which is typical for the structure of liquid water. We can observe two POMs per La ion, necessitating the need for other cations (e.g., protons) to contribute to charge neutralization. This structure can be seen as a “snapshot” of an intermediate in the process by which the spheres form, the next step being the accumulation of a larger number of POM units and transfer of the cations to the surface of the hydrated phosphotungstic acid crystallites.

Electrochemistry. Phosphotungstic acid has been used as an electrocatalyst at different pH values from 0 to 7 for the OER in water splitting. The catalyst is highly dependent on the pH of the electrolyte and LSV measurements give the lowest overpotential at acidic conditions, see Figure 6. At pH 0 (0.5 M H₂SO₄), the overpotential was as low as 286 mV for the formation of O₂(g) bubbles (OER). At pH 3 (citric acid/sodium citrate buffer), the overpotential was 308 mV and at pH 7 (phosphate buffer), the catalyst showed an overpotential of 397 mV. The formation of oxygen bubbles becomes more and more pronounced with increasing potential. The determined faradaic efficiency was quite high, exceeding 90% and slightly increasing in time (see Supporting Information Table TS3–5).

From the cyclic voltammograms obtained at pH = 7, a redox peak was observed at 0.72 V, confirming the W⁶⁺/W⁵⁺ redox state, while at pH = 0, two redox peaks were observed at 0.72 and 0.50 V, confirming both W⁶⁺/W⁵⁺ and W⁵⁺/W⁴⁺ redox states, respectively.¹⁵ The shift in the redox peak confirms the influence of phosphorus on the redox potential of tungsten, as phosphorus incorporation enhanced the acidity.¹⁹

The Tafel slopes calculated from the linear sweep voltammetry (LSV) measurements showed the efficiency of

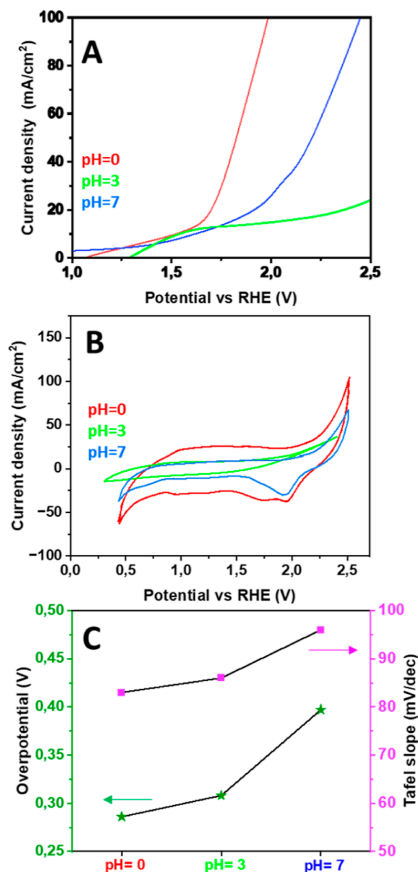


Figure 6. Electrochemical measurements at pH 0, 3, and 7, where phosphotungstic acid has been evaluated as an electrocatalyst for the OER in water splitting. (A) LSV. (B) CV curves obtained after initial stabilization. (C) pH dependence of the overpotential and Tafel slope.

an electrode to produce current in response to a change in the applied potential. The Tafel slope increases with pH in the tested range: 83 mV/dec at pH 0, 86 mV/dec at pH 3, and 96 mV/dec at pH 7. Chronoamperometry (CA) was performed to evaluate the stability of the catalyst over time. The current density was observed during 24 h and found to be stable at an applied potential of 0.4 V (vs RHE) (Figures S3–S5 and Table S3).

CONCLUSIONS

Exploiting the factors leading to a decrease in the potential surface charge of phosphotungstic acid nanocrystals allowed the development of nanostructured microspheres of this material by simple sol–gel synthesis. Determination of the crystal structure of the potential intermediate product—an acidic salt of La(III) cations—provided additional clues to how the self-assembly process occurs. Sol–gel-produced water-insoluble phosphotungstic acid was demonstrated as a

potential candidate for an electrocatalyst for the OER process at acidic conditions showing a very low overpotential in 0.5 M H₂SO₄ (pH = 0) electrolyte with great stability.

Experimental Section. All chemicals were purchased from Sigma-Aldrich and used without further purification. The particles were produced by the general procedure of using 30 mL of a solution containing 1 mM of the cation Ti(IV) from potassium titanium oxide oxalate hydrate, or La(III) from lanthanum nitrate with pH near 0 (<0.1). To this was added 1 mM of phosphotungstic acid, upon which a precipitate formed. The precipitate was filtered either immediately or after the solution was evaporated to a near volume of 10 mL in a water bath held above 90 °C. The precipitate was washed with Milli-Q water and collected by centrifugation. Crystals of La and phosphotungstic acid were prepared by dissolving 0.4 g of lanthanum nitrate in 30 mL 2 M HCl and heating the solution in a > 95 °C water bath. To this was added 3 g of phosphotungstic acid and the solution was evaporated to approximately 12 mL, without stirring, at which point large cube-shaped crystals formed. Upon cooling, small X-ray quality crystals formed. The crystals were stable under the mother liquor, but upon drying, they degraded into a white powder. **Safety concern:** using relatively concentrated acidic solutions at near boiling water temperature is associated with a risk of stench of highly corrosive and irritating liquid—the use of gloves and safety goggles is compulsory on operation.

SEM and energy-dispersive X-ray spectroscopy (EDS) samples were immobilized on carbon tape and characterized using a Hitachi FlexSEM-1000 II. EDS spectra were analyzed using an Oxford Instruments EDS analysis system operated by the Aztec software.

For TEM observations, dispersions of the sol–gel were deposited on holey carbon grids (PELCO 50 mesh grids: pitch 508 μm; hole width 425 μm; bar width 83 μm; transmission 70%) and observed using a Philips CM/12 microscope (Thermo Fisher Inc.) fitted with a LaB₆ gun and operated at 100 kV. Negative TEM films were scanned using an Epson Perfection Pro 750 film scanner.

BET specific surface area and pore volume were determined from nitrogen adsorption/desorption isotherms at −196 °C (Micromeritics ASAP 2020 surface area and porosity analyzer). The samples were degassed at 120 °C for 12 h before measurements.

DLS and zeta potential were done by suspending spheres in distilled water and analyzing them on a Malvern Analytical Zetasizer Nano analyzer, equipped with a red (362.8 nm) laser. Data was processed using the Zetasizer Ver. 7.12 software.

For AFM, samples were characterized using a Bruker Dimension FastScan atomic force microscope with a NanoScope V controller in the ScanAsyst mode using a FastScan-B AFM probe (silicon tip, f_r : 400 kHz, k: 4 N/m, tip radius: 5 nm nominally) and a scan rate of 1–3 Hz. Data was processed using Bruker NanoScope Analysis.

Preparative TGA was performed using a Notherm LE/6/11/P300 furnace and an FA2204B electronic balance. Approximately 160 mg of PW spheres was placed in two crucibles and heated to 120, 170, 220, 270, 320, 400, and 500 °C. At each point, the weight of one crucible was recorded, and from the other, a sample was taken for the EDS analysis.

Single-crystal XRD data was collected on a Bruker D8 QUEST ECO instrument and processed using the Apex4 software. A total of 2424 frames were collected. The total exposure time was 2.02 h. The frames were integrated with the

Bruker SAINT software package using a narrow-frame algorithm. The integration of the data using a triclinic unit cell yielded a total of 57 188 reflections to a maximum θ angle of 28.00° (0.76 Å resolution), of which 22 324 were independent (average redundancy 2.562, completeness = 98.7%, $R_{\text{int}} = 6.52\%$, $R_{\text{sig}} = 8.17\%$) and 17 582 (78.76%) were greater than $2\sigma(F^2)$. The final cell constants of $a = 14.008(3)$ Å, $b = 15.140(3)$ Å, $c = 22.386(5)$ Å, $\alpha = 88.978(5)^\circ$, $\beta = 89.228(4)^\circ$, $\gamma = 80.885(5)^\circ$, and volume = 4686.7(18) Å³ are based upon the refinement of the XYZ-centroids of 9879 reflections above $20\sigma(I)$ with $4.512 < 2\theta < 71.58$. Data were corrected for absorption effects using the multiscan method (SADABS). The ratio of minimum to maximum apparent transmission was 0.307. The calculated minimum and maximum transmission coefficients (based on the crystal size) were 0.0370 and 0.0870. The structure was solved and refined using the Bruker SHELXTL software package, using space group $P\bar{1}$, with $Z = 2$ for the formula unit, H₆₅LaO_{113.50}P₂W₂₄. The structure loses water extremely easily, which likely creates multiple defects reflected in low precision in determination of the electron density, in spite of using low-temperature data collection. This generated a B-alert for large residual electron density. The B-alerts for isolated oxygen atoms are actually misleading because these atoms are actually water molecules invoked into a network of hydrogen bonding. The location of hydrogen atoms was impossible to discern because of the challenges in obtaining the correct electron density map. The final anisotropic full-matrix least-squares refinement on F^2 with 1268 variables converged at $R1 = 5.96\%$ for the observed data and $wR2 = 16.30\%$ for all data. The goodness-of-fit was 0.990. The largest peak in the final difference electron density synthesis was 9.579 e[−]/Å³ and the largest hole was −6.835 e[−]/Å³ with an RMS deviation of 0.749 e[−]/Å³. On the basis of the final model, the calculated density was 4.588 g/cm³ and $F(000)$, 5631 e[−]. The full list of bond distances and angles is available in Supporting Information Tables S7–S9.

All electrochemical experiments were performed at room temperature. The experiments were performed in a three-electrode system using an SP-50 potentiostat (Biologic). The phosphotungstic material was tested as an electrocatalyst at different pH from pH 0–7 for the OER in water splitting. The catalyst was then mixed with carbon black to enhance the conductivity and subsequently deposited on the graphite felt (loading = 0.2 mg/cm²). A three-electrode setup was used to perform the electrocatalytic experiments; a catalyst-loaded graphite working electrode, Pt-mesh as a counter electrode, and Ag/AgCl as a reference electrode. CV, LSV, and CA were performed. OER tests were carried out in a single-compartment electrolytic cell with different electrolytes of 0.5 M H₂SO₄ (pH = 0), citric acid/sodium citrate buffer (pH = 3), and phosphate buffer (pH = 7). For cyclability, 200 cycles of CV were performed, and the working electrode saturated after 20–30 cycles of activation. The iR drop was directly compensated for by the potentiostat (with 82% compensation). The potentials recorded were finally calibrated in relation to the reversible hydrogen electrode (E_{RHE}) by using the equation: $E_{\text{RHE}} = E_{\text{Ag/AgCl}} + 0.059 \times \text{pH}$. To minimize the capacitive current, the scan rate for the LSV curve was 10 mV/s. The overpotential (η) of HER was calculated by using the equation: $\eta = E_{\text{RHE}} - 1.23$, after reduction of the redox potential of oxygen, $E_{\text{O}_2/\text{O}_2^-} = 1.23$. The Tafel plots were obtained by transforming the LSV curve into $\log(j)$ vs E . All

experiments were performed twice to check reproducibility. The faradaic efficiency was evaluated via control of the gas evolution. The instrumental setup and procedure details are reported in the [Supporting Information](#) (Figure S7 and Tables S3–S5).

■ ASSOCIATED CONTENT

Supporting Information

The Supporting Information is available free of charge at <https://pubs.acs.org/doi/10.1021/acs.inorgchem.3c04122>.

Additional experimental data; graphs and tables for TGA, EDS, DLS, and electrochemical measurements; and crystallographic data (PDF)

Accession Codes

CCDC 2307589 contains the supplementary crystallographic data for this paper. These data can be obtained free of charge via www.ccdc.cam.ac.uk/data_request/cif, or by emailing data_request@ccdc.cam.ac.uk, or by contacting The Cambridge Crystallographic Data Centre, 12 Union Road, Cambridge CB2 1EZ, UK; fax: +44 1223 336033.

■ AUTHOR INFORMATION

Corresponding Author

Vadim Kessler – Department of Molecular Sciences, Swedish University of Agricultural Sciences, Uppsala 75007, Sweden; orcid.org/0000-0001-7570-2814; Email: vadim.kessler@slu.se

Authors

Björn Greijer – Department of Molecular Sciences, Swedish University of Agricultural Sciences, Uppsala 75007, Sweden

Wannes De Turck – Department of Molecular Sciences, Swedish University of Agricultural Sciences, Uppsala 75007, Sweden

Geoffrey Daniel – Department of Forest Biomaterials and Technology, Swedish University of Agricultural Sciences, Uppsala 75007, Sweden

Jayeeta Saha – Department of Materials and Environmental Chemistry, Arrhenius Lab, Stockholm University, Stockholm 106 91, Sweden

Mats Johansson – Department of Materials and Environmental Chemistry, Arrhenius Lab, Stockholm University, Stockholm 106 91, Sweden; orcid.org/0000-0003-4319-1540

Gulaim A. Seisenbaeva – Department of Molecular Sciences, Swedish University of Agricultural Sciences, Uppsala 75007, Sweden; orcid.org/0000-0003-0072-6082

Complete contact information is available at: <https://pubs.acs.org/doi/10.1021/acs.inorgchem.3c04122>

Notes

The authors declare no competing financial interest.

■ ACKNOWLEDGMENTS

We thank Dr. Fredric Svensson of Uppsala University for his help with XRPD measurements, Troy Breijaert for his help with DLS and zeta potential measurements, Tetyana Budnyak of Uppsala University for help with BET, and German Salazar Alvarez for fruitful discussion about the electrochemical characteristics of produced materials. The Swedish Research Council is gratefully acknowledged for the financial support to the grant 2018-03811_VR.

■ REFERENCES

- (1) You, B.; Sun, Y. Innovative Strategies for Electrocatalytic Water Splitting. *Acc. Chem. Res.* **2018**, *51* (7), 1571–1580.
- (2) Li, W.; Jiang, N.; Hu, B.; Liu, X.; Song, F.; Han, G.; Jordan, T. J.; Hanson, T. B.; Liu, T. L.; Sun, Y. Electrolyzer Design for Flexible Decoupled Water Splitting and Organic Upgrading with Electron Reservoirs. *Chem* **2018**, *4* (3), 637–649.
- (3) Han, G.; Jin, Y.-H.; Burgess, R. A.; Dickenson, N. E.; Cao, X.-M.; Sun, Y. Visible-Light-Driven Valorization of Biomass Intermediates Integrated with H₂ Production Catalyzed by Ultrathin Ni/CdS Nanosheets. *J. Am. Chem. Soc.* **2017**, *139* (44), 15584–15587.
- (4) Winter, M.; Brodd, R. J. What Are Batteries, Fuel Cells, and Supercapacitors? *Chem. Rev.* **2004**, *104* (10), 4245–4270.
- (5) Pei, M.; Petäjäniemi, M.; Regnell, A.; Wijk, O. Toward a Fossil Free Future with HYBRIT: Development of Iron and Steelmaking Technology in Sweden and Finland. *Metals* **2020**, *10* (7), 972.
- (6) Baraj, E.; Ciahotný, K.; Hlinčík, T. The Water Gas Shift Reaction: Catalysts and Reaction Mechanism. *Fuel* **2021**, *288*, 119817.
- (7) Jiao, Y.; Zheng, Y.; Jaroniec, M.; Qiao, S. Z. Design of Electrocatalysts for Oxygen- and Hydrogen-Involving Energy Conversion Reactions. *Chem. Soc. Rev.* **2015**, *44* (8), 2060–2086.
- (8) Chen, S.; Huang, H.; Jiang, P.; Yang, K.; Diao, J.; Gong, S.; Liu, S.; Huang, M.; Wang, H.; Chen, Q. Mn-Doped RuO₂ Nanocrystals as Highly Active Electrocatalysts for Enhanced Oxygen Evolution in Acidic Media. *ACS Catal.* **2020**, *10* (2), 1152–1160.
- (9) Park, H.-S.; Yang, J.; Cho, M. K.; Lee, Y.; Cho, S.; Yim, S.-D.; Kim, B.-S.; Jang, J. H.; Song, H.-K. RuO₂ Nanocluster as a 4-in-1 Electrocatalyst for Hydrogen and Oxygen Electrochemistry. *Nano Energy* **2019**, *55*, 49–58.
- (10) Li, G.; Li, S.; Ge, J.; Liu, C.; Xing, W. Discontinuously Covered IrO₂-RuO₂@Ru Electrocatalysts for the Oxygen Evolution Reaction: How High Activity and Long-Term Durability Can Be Simultaneously Realized in the Synergistic and Hybrid Nano-Structure. *J. Mater. Chem. A* **2017**, *5* (33), 17221–17229.
- (11) Reier, T.; Oezaslan, M.; Strasser, P. Electrocatalytic Oxygen Evolution Reaction (OER) on Ru, Ir, and Pt Catalysts: A Comparative Study of Nanoparticles and Bulk Materials. *ACS Catal.* **2012**, *2* (8), 1765–1772.
- (12) Huang, Z.-F.; Song, J.; Pan, L.; Zhang, X.; Wang, L.; Zou, J.-J. Tungsten Oxides for Photocatalysis, Electrochemistry, and Phototherapy. *Adv. Mater.* **2015**, *27* (36), 5309–5327.
- (13) Kirti, Dobaria, P.; Maurya, A.; Kaushik, A.; Kanani, P.; Rajput, P.; Jha, S. N.; Das, B.; Srivastava, D. N.; Kushwaha, S.; Patel, K. Hierarchical Polyoxometallate Confined in Woven Thin Films for Single-Cluster Catalysis: Simplified Electrodes for Far-Fetched O₂ Evolution from Seawater. *ACS Catal.* **2023**, *13* (7), 4587–4596.
- (14) Cheng, H.; Klaproth, M.; Sagaltchik, A.; Li, S.; Thomas, A. Ordered Mesoporous WO_{2.83}: Selective Reduction Synthesis, Exceptional Localized Surface Plasmon Resonance and Enhanced Hydrogen Evolution Reaction Activity. *J. Mater. Chem. A* **2018**, *6* (5), 2249–2256.
- (15) Darmawi, S.; Burkhardt, S.; Leichtweiss, T.; Weber, D. A.; Wenzel, S.; Janek, J.; Elm, M. T.; Klar, P. J. Correlation of Electrochromic Properties and Oxidation States in Nanocrystalline Tungsten Trioxide. *Phys. Chem. Chem. Phys.* **2015**, *17* (24), 15903–15911.
- (16) Ji, X.; Ma, M.; Ge, R.; Ren, X.; Wang, H.; Liu, J.; Liu, Z.; Asiri, A. M.; Sun, X. WO₃ Nanoarray: An Efficient Electrochemical Oxygen Evolution Catalyst Electrode Operating in Alkaline Solution. *Inorg. Chem.* **2017**, *56* (24), 14743–14746.
- (17) Nakayama, M.; Takeda, A.; Maruyama, H.; Kumbhar, V.; Crosnier, O. Cobalt-Substituted Iron-Based Wolframite Synthesized via Polyol Route for Efficient Oxygen Evolution Reaction. *Electrochim. Commun.* **2020**, *120*, 106834.
- (18) Xie, X.; Mu, W.; Li, X.; Wei, H.; Jian, Y.; Yu, Q.; Zhang, R.; Lv, K.; Tang, H.; Luo, S. Incorporation of Tantalum Ions Enhances the Electrocatalytic Activity of Hexagonal WO₃ Nanowires for Hydrogen Evolution Reaction. *Electrochim. Acta* **2014**, *134*, 201–208.

(19) Yan, T.; Liu, Q.; Wang, S.; Xu, G.; Wu, M.; Chen, J.; Li, J. Promoter rather than Inhibitor: Phosphorus Incorporation Accelerates the Activity of V_2O_5 - WO_3 /TiO₂ Catalyst for Selective Catalytic Reduction of NO_x by NH₃. *ACS Catal.* **2020**, *10* (4), 2747–2753.

(20) Chen, J.; Yu, D.; Liao, W.; Zheng, M.; Xiao, L.; Zhu, H.; Zhang, M.; Du, M.; Yao, J. WO_{3-x} Nanoplates Grown on Carbon Nanofibers for an Efficient Electrocatalytic Hydrogen Evolution Reaction. *ACS Appl. Mater. Interfaces* **2016**, *8* (28), 18132–18139.

(21) Shang, X.; Rao, Y.; Lu, S.-S.; Dong, B.; Zhang, L.-M.; Liu, X.-H.; Li, X.; Liu, Y.-R.; Chai, Y.-M.; Liu, C.-G. Novel WS₂/WO₃ Heterostructured Nanosheets as Efficient Electrocatalyst for Hydrogen Evolution Reaction. *Mater. Chem. Phys.* **2017**, *197*, 123–128.

(22) Chen, J.; Ren, B.; Cui, H.; Wang, C. Constructing Pure Phase Tungsten-Based Bimetallic Carbide Nanosheet as an Efficient Bifunctional Electrocatalyst for Overall Water Splitting. *Small* **2020**, *16* (23), 1907556.

(23) Zhao, Y.; Tang, Q.; He, B.; Yang, P. Mo Incorporated W18O49 Nanofibers as Robust Electrocatalysts for High-Efficiency Hydrogen Evolution. *Int. J. Hydrogen Energy* **2017**, *42* (21), 14534–14546.

(24) Bajuk-Bogdanović, D.; Uskoković-Marković, S.; Hercigonja, R.; Popa, A.; Holclajtner-Antunović, I. Study of the Decomposition Pathway of 12-Molybdophosphoric Acid in Aqueous Solutions by Micro Raman Spectroscopy. *Spectrochim. Acta, Part A* **2016**, *153*, 152–159.

(25) Zhu, Z.; Tain, R.; Rhodes, C. A Study of the Decomposition Behaviour of 12-Tungstophosphate Heteropolyacid in Solution. *Can. J. Chem.* **2003**, *81* (10), 1044–1050.

(26) Yan, N.; Zhang, W.; Cui, H.; Feng, X.; Liu, Y.; Shi, J. Potassium Phosphotungstate Spheres as an Anode Material for a Solar Rechargeable Battery. *Sustainable Energy Fuels* **2018**, *2* (2), 353–356.

(27) Li, M.; Xu, C.; Ren, J.; Wang, E.; Qu, X. Photodegradation of β -sheet amyloid fibrils associated with Alzheimer's disease by using polyoxometalates as photocatalysts. *Chem. Commun.* **2013**, *49* (97), 11394–11396.

(28) Rominger, K. M.; Nestor, G.; Eriksson, J. E.; Seisenbaeva, G. A.; Kessler, V. G. Complexes of Keggin POMs [PM12O40]₃- (M = Mo, W) with GlyGly Peptide and Arginine - Crystal Structures and Solution Reactivity. *Eur. J. Inorg. Chem.* **2019**, *2019* (39–40), 4297–4305.

(29) Grejfer, B.; De Donder, T.; Nestor, G.; Eriksson, J. E.; Seisenbaeva, G. A.; Kessler, V. G. Complexes of Keggin POMs [PM12O40]₃- (M = Mo, W) with GlyGlyGly and GlyGlyGlyGlyGlyOligopeptides. *Eur. J. Inorg. Chem.* **2021**, *2021* (1), 54–61.

(30) Kessler, V. G.; Seisenbaeva, G. A. Molecular Mechanisms of the Metal Oxide Sol-Gel Process and Their Application in Approaches to Thermodynamically Challenging Complex Oxide Materials. *J. Sol-Gel Sci. Technol.* **2023**, *107* (1), 190–200.

(31) Whitehead, C. B.; Ozkar, S.; Finke, R. G. LaMer's 1950 Model of Particle Formation: A Review and Critical Analysis of Its Classical Nucleation and Fluctuation Theory Basis, of Competing Models and Mechanisms for Phase-Changes and Particle Formation, and Then of Its Application to Silver Halide, Semiconductor, Metal, and Metal-Oxide Nanoparticles. *Mater. Adv.* **2021**, *2* (1), 186–235.

(32) Grejfer, B. H.; Nestor, G.; Eriksson, J. E.; Seisenbaeva, G. A.; Kessler, V. G. Factors Influencing Stoichiometry and Stability of Polyoxometalate - Peptide Complexes. *Dalton Trans.* **2022**, *51* (24), 9511–9521.

(33) Huang, X.; Wang, W.; Liu, X. H3PW12O40-Doped Pyromellitic Diimide Prepared via Thermal Transformation as an Efficient Visible-Light Photocatalyst. *J. Mater. Sci.* **2020**, *55* (20), 8502–8512.

(34) Donohue, M. D.; Aranovich, G. L. Classification of Gibbs Adsorption Isotherms. *Adv. Colloid Interface Sci.* **1998**, *76–77*, 137–152.

(35) Kessler, V. G.; Spijsma, G. I.; Seisenbaeva, G. A.; Håkansson, S.; Blank, D. H. A.; Bouwmeester, H. J. M. New insight in the role of modifying ligands in the sol-gel processing of metal alkoxide

precursors. A possibility to approach new classes of materials. *J. Sol-Gel Sci. Technol.* **2006**, *40*, 163–179.

(36) Kessler, V. G.; Seisenbaeva, G. A. Molecular mechanisms of the metal oxide sol-gel process and their application in approaches to thermodynamically challenging complex oxide materials. *J. Sol-Gel Sci. Technol.* **2023**, *107*, 190–200.

(37) Yan, N.; Zhang, W.; Shi, J.; Liu, Y.; Cui, H. Nano Potassium Phosphotungstate Spheres/Sulfur Composites as Cathode for Li-S Batteries. *Mater. Lett.* **2018**, *229*, 198–201.

Recommended by ACS

Effect of Nucleotides on the Phase and Crystal Structure of Synthetic Calcium Carbonate

Arad Lang, Boaz Pokroy, *et al.*

JUNE 09, 2023

CRYSTAL GROWTH & DESIGN

READ 

Crystal Growth and Phase Formation of High-Entropy Rare-Earth Aluminum Perovskites

Matheus Pianassola, Mariya Zhuravleva, *et al.*

DECEMBER 09, 2022

CRYSTAL GROWTH & DESIGN

READ 

Calorimetric Measurement of the Surface Energy of Enstatite, MgSiO₃

Megan A. Householder, Alexandra Navrotsky, *et al.*

SEPTEMBER 28, 2023

THE JOURNAL OF PHYSICAL CHEMISTRY C

READ 

Effect of Raw Material Particle Size on the Synthesis of La₂Zr₂O₇ by the Molten Salt Method

Hao Chen, Hao Bai, *et al.*

MARCH 09, 2023

INORGANIC CHEMISTRY

READ 

Get More Suggestions >

Complexes of Oligopeptides of Structure-Determining Amino Acids with Phosphotungstic Acid

Björn Greijer, Edgar Stigell, Timothe Guerin, and Vadim G. Kessler*

Cite This: <https://doi.org/10.1021/acs.cgd.4c00806>

Read Online

ACCESS |



Metrics & More

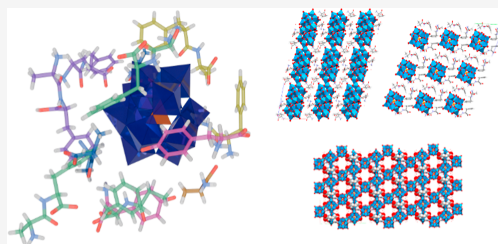


Article Recommendations



Supporting Information

ABSTRACT: Peptides tend to form anisotropic structures, being both asymmetric and chiral. Structure-determining peptides include phenylalanine (Phe) and tyrosine (Tyr) amino acids as they contain aromatic rings, which are sterically demanding and prone to self-assembly via π -stacking. Pursuing the mechanisms of protein interactions with oxide nanoparticles, we used Keggin phosphotungstic acid polyoxometalate (POM) as a model. Six complexes of the POM with different peptide-based ligands were studied, including Phe, Ala (Alanine), and Tyr. Phe–Ala formed a layered structure with pockets of π -stacking involving four Phe residues. Ala–Phe formed two structures based on the rate of formation. The faster forming structure had a loose pattern of POMs in columns surrounded by chains of the ligand with alternating H-bonding and π -stacking. The slower-forming one had a denser network, also with columns of POMs, but with a more complex network of peptides, including π -stacks of three residues appearing as a “web” rather than a “chain”. Ala–Ala showed mainly H-bonding connecting the molecules, with the peptide filling the spaces between POMs rather than controlling the structure. Ala seemed to mainly act as a bridge between three POMs, and it had the effect of forming a highly porous structure reminiscent of metal–organic frameworks (MOFs). Tyr formed long columns of the amino acid with both vertical and lateral H-bonding, resulting in alternating layers of POMs and parallel Tyr columns. These structures provide insights into the interactions between biomolecules and POMs, which is valuable for the design and synthesis of POM-derived composite materials.



INTRODUCTION

Life has been surrounded by mineral nanoparticles (NPs) since they first emerged in the primordial soup. Weathering of minerals will eventually produce nanomaterials, which remain in bodies of water and affect the organisms living in them.¹ In modern times, such materials are studied and used for a vast number of purposes, are frequently produced artificially, and are occasionally combined with biomolecules to form composite materials.²

Self-assembly reactions, such as the sol–gel process,³ are abundant in nature. Proteins frequently assemble into complex materials, both with a purpose, such as spider silk,⁴ and accidentally, such as the amyloid β -peptides plaques which cause Alzheimer's disease.⁵ Understanding the mechanism behind these assembly reactions is naturally highly sought after. It has been shown that aromatic residues, tyrosine (Tyr) and phenylalanine (Phe), are often responsible for fiber formation^{6,7} and properties.⁴

NPs have been shown to often interact with proteins.^{8,9} Determining the nature of the interactions can be difficult in systems as complex as a naturally occurring one; therefore, a model has been developed in order to discover some general principles of the interactions. By using analogues of NPs and proteins, we have developed a model system to study how they

might interact.^{10–12} This consists of Keggin polyoxometalates (POMs) and oligopeptides. Keggin POMs consist of a central heteroatom within a roughly spherical cage of 12 transition metal atoms in their highest oxidation state, all bridged by oxygen atoms. POMs have frequently been shown to interact with biomolecules.^{13–18} In this study, phosphotungstic acid (PW) was used, which has the formula $H_3[PW_{12}O_{40}]$. Oligopeptides are short chains of amino acids, which are the building blocks of proteins. In this study, sequences consisting of alanine (Ala) and phenylalanine (Phe), as well as tyrosine (Tyr), as a single amino acid were used.

Phe and Tyr, as amino acids with an aromatic side chain, play a significant role in controlling the folding of a protein. This is largely due to their ability to form π -bonds with other aromatic groups, providing greater stability to a protein fold or complex. It has been shown that oligopeptides containing

Received: June 12, 2024

Revised: July 17, 2024

Accepted: July 18, 2024

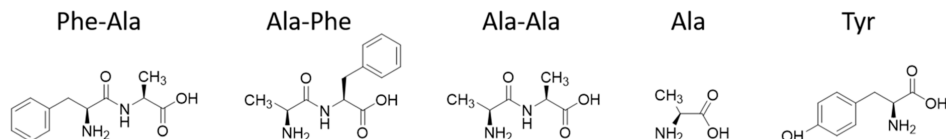


Figure 1. Bonding schemes for ligands applied in this study.

phenylalanine will self-assemble into nanostructures in aqueous media.^{6,7} Hybrid materials of POMs and biopolymers are increasingly being developed and used for purposes such as catalysis, adhesion, and biomedicine.^{2,19}

Our previous studies on this topic focused mainly on oligoglycines, which demonstrated that POMs can interact with the backbone of proteins in a variety of ways and also how changing the conditions can alter how the same components form crystals.^{10–12} Here, we have aimed to investigate how more hydrophobic oligopeptides, such as trialanine, and mixed dipeptides, such as Ala–Phe and Phe–Ala, may interact with NPs.

MATERIALS AND METHODS

All materials were purchased from Sigma-Aldrich and used without further purification. 0.01 mmol of phosphotungstic acid and 0.03 mmol of peptide were dissolved in 5 mL of HCl each (0.1 M for 4 and 6 and 0.5 M for 1, 2, 3, and 5). The peptide solution was added to the POM solution and mixed in a 15 mL Falcon tube. A portion was transferred to a Petri dish to evaporate quickly. The tube was left open to allow the solvent to evaporate slowly. X-ray quality crystals formed within several months for 1, 3, 4, and 5 in test tubes and within a few days for 2 and 6 in a Petri dish. The ligands used were Phe–Ala for 1, Ala–Phe for 2 and 3, Ala–Ala for 4, Ala–Ala (degraded to Ala) for 5, and Tyr for 6. Single-crystal XRD data was collected using a Bruker D8 QUEST ECO instrument and was processed using the Apex4 software package. Details are given in [Supporting Information Methods](#). EDS was performed with a Hitachi FlexSEM 1000 II instrument (Oxford Instruments) operated by Aztec software. Infrared spectroscopy was performed with a PerkinElmer Spectrum-100 FTIR spectrometer PerkinElmer Spectrum-100.

RESULTS AND DISCUSSION

The peptides used (Figure 1) were chosen for their ability to simulate a more complex part of a protein than our previous studies, which mainly focused on oligoglycines.^{10–12} The amino acids used here are both more complex and more hydrophobic, which is more accurate to globular proteins, as they often show a hydrophobic core and a hydrophilic surface. Details of the data collection and refinement are provided in [Table 1](#).

Structure 1 (Figure 2) was found in yellow, block-shaped crystals and forms distinct layers (Figure 2B), with alternating sheets of POMs and peptides. Viewed straight on, the POM layer is arranged in a “mirrored zig zag.” The peptides form chains of four π -stacked Phe side chains (Figure 2C) and H-bonds (Figure 2D).

The hydrogen bonding network is extensive, with the shortest bonds being to a particular water molecule and other water molecules and a carbonyl group: O(1)–O(4) 2.495(2) Å, O(1)–O(1Y) 2.535(2) Å, and O(1)–O(6) 2.551(2) Å. Only slightly longer are groups of bonds between peptides and water: O(2X)–O(10) 2.615(2) Å, O(3X)–O(4) 2.627(2) Å, O(1Y)–O(3Z) 2.662(2) Å, and O(3V)–O(1Z) 2.677(2) Å. Next comes a group of water molecules bonding terminal POM oxygen, amine groups, carboxyl groups, and

other water molecules: N(2X)–O(7) 2.698(3) Å, O(35B)–O(8) 2.715(2) Å, O(9)–O(13) 2.741(3) Å, N(2Z)–O(8) 2.752(3) Å, O(1V)–O(9) 2.763(2) Å, O(2)–O(10) 2.781(2) Å, and O(6)–O(9) 2.789(2) Å. A group of bonds with terminal POM oxygen to an amine group, water, and a carboxyl group and terminal POM oxygens and water follows: O(28B)–O(8) 2.792(2) Å, O(38B)–N(2X) 2.794(1) Å, O(34B)–O(10) 2.822(1) Å, O(26A)–O(4) 2.825(2) Å, and O(25A)–O(27B) 2.838(1) Å. Next is a mixed group of bonds with terminal and bridging POM oxygen, water, amine groups, and carboxyl groups, with most combinations represented: N(2V)–O(2Z) 2.842(2) Å, O(13B)–O(6) 2.845(1) Å, O(24A)–N(2X) 2.847(2) Å, O(3)–O(2) 2.847(2) Å, O(31B)–N(2X) 2.855(2) Å, N(2Y)–O(9) 2.890(1) Å, O(30A)–O(12) 2.900(1) Å, O(29B)–O(2V) 2.902(3) Å, O(37A)–O(31B) 2.903(3) Å, O(2Y)–O(13) 2.914(2) Å, O(9B)–O(5) 2.926 Å, O(10)–O(11) 2.931(4) Å, N(2V)–O(12) 2.933(3) Å, N(2Z)–O(5) 2.942(1) Å, and O(2Y)–N(2Z) 2.946(1) Å. Next comes a series of bonds with mostly POM oxygens or water molecules bonding amine, amide, carbonyl groups, water molecules, and each other: O(28A)–O(33B) 2.947(2) Å, O(25A)–O(28B) 2.947(2) Å, O(30B)–O(4) 2.961(2) Å, O(39B)–N(2V) 2.963(4) Å, O(1X)–O(11) 2.965(1) Å, O(11A) N(1Y) 2.966(2) Å, O(33B)–O(12) 2.966(2) Å, O(36B)–O(3Y) 2.969(3) Å, N(2Z)–O(6) 2.972(1) Å, O(5)–O(7) 2.977(2) Å, N(2Y)–O(2) 2.978(3) Å, O(30A)–O(34B) 2.980(1) Å, O(33A)–N(2V) 2.992(2) Å, and O(18B)–O(2) 2.993(2) Å. Pushing the upper limit of hydrogen bonding, but still worth noting, are a group of bonds between carbonyl, carboxyl, and amide groups and water or POM oxygen, as well as POM–POM contacts: O(2Y)–O(1) 3.003(1) Å, O(33A)–O(34B) 3.028(1) Å, O(12A)–O(5) 3.028(1) Å, O(36B)–O(3X) 3.030(2) Å, O(39A)–O(29B) 3.032(2) Å, O(2Y)–O(6) 3.038(2) Å, and O(39A)–N(1X) 3.060(2) Å.

Some of the bonds to O1 are extremely short, but this can be attributed to the tight packing and strong attractive forces between the molecules. The oxygen atoms O1–O13 do not have hydrogen placed on them, but it is clear from their placement and bonding patterns that they are, in fact, water molecules. O9 and O10 appear to have bond angles close to those of oxonium ions and are likely protonated. The close contacts between POMs are likely due to protonation of the POM, as they are in the range of H-bonds.

In contrast to 1, the needle-shaped crystals of 2 (Figure 3) do not form layers, but rather columns of POMs surrounded by a matrix of peptides (Figure 3B). The peptides form chains of alternating H-bonds between peptides, POMs and water molecules (Figure 3C), and π -stacked Phe side chains (Figure 3D).

The shortest contacts are between carboxyl groups and an amino group N(1B)–O(2A) 2.658(8) Å or water O(1B)–O(1X) 2.838(6) Å. Slightly longer are bonds terminal POM oxygen and an amide group O(18)–N(2B) 2.903(4) Å, a

Table 1. Crystallographic Data for Compounds 1–6

	1	2	3	4	5	6
chemical formula	$C_{35}H_{48}N_6O_{49}PW_{12}$	$C_{34}H_{48}N_6O_{50}PW_{12}$	$C_{18}H_{13}N_4O_{34}P_3W_6$	$C_{12}H_{31}N_4O_{30}PW_{12}$	$C_6H_{19}N_2O_7P_1W_{18}$	$C_{18}H_{35}N_2O_{48}PW_{12}$
formula weight	3445.20 g/mol	3423.78 g/mol	1791.98 g/mol	3257.49 g/mol	4605.95 g/mol	3273.56 g/mol
temperature	293(2) K	293(2) K	293(2) K	293(2) K	293(2) K	295(2) K
wavelength	0.71073 Å	0.71073 Å	0.71076 Å	0.71073 Å	0.71073 Å	0.71073 Å
crystal size	0.130 × 0.180 × 0.240 mm	0.020 × 0.080 × 0.210 mm	0.300 × 0.300 × 0.800 mm	0.010 × 0.080 × 0.100 mm	0.320 × 0.340 × 0.540 mm	0.020 × 0.020 × 0.100 mm
crystal system	monoclinic	monoclinic	triclinic	monoclinic	orthorhombic	triclinic
space group	$P12_11$	$P12_11$	$P1$	$P12_11$	$C222$	$P1$
unit cell dimensions	a 15.0118(6) Å	9.737(6) Å	9.8759(8) Å	9.9033(5) Å	16.1458(8) Å	14.516(4) Å
	b 26.6598(12) Å	26.169(16) Å	14.3510(11) Å	26.5990(14) Å	34.5595(17) Å	14.786(5) Å
	c 15.5858(6) Å	14.337(9) Å	14.6921(11) Å	10.0515(5) Å	12.9893(6) Å	90°
volume	6106.2(4) Å ³	3546. (4) Å ³	1820.2(3) Å ³	2647.4(2) Å ³	7247.9(6) Å ³	2918.8(15) Å ³
Z	4	2	2	2	4	2
theta range for data collection	2.06 to 35.26°	2.14 to 28.13°	2.44 to 34.98°	2.17 to 35.13°	2.52 to 35.11°	2.12 to 26.60°
index ranges	$-24 \leq h \leq 24$	$-12 \leq h \leq 12$	$-15 \leq h \leq 15$	$-16 \leq h \leq 15$	$-25 \leq h \leq 23$	$-18 \leq h \leq 18$
	$-42 \leq k \leq 42$	$-34 \leq k \leq 34$	$-21 \leq k \leq 22$	$-42 \leq k \leq 42$	$-55 \leq k \leq 55$	$-18 \leq k \leq 18$
	$-24 \leq l \leq 24$	$-18 \leq l \leq 18$	$-23 \leq l \leq 23$	$-15 \leq l \leq 16$	$-20 \leq l \leq 20$	$-19 \leq l \leq 19$
reflections collected	103,478	49,681	24,187	49,121	48,469	26,319
independent reflections	50,215 [R(int) = 0.0500]	17,101 [R(int) = 0.0490]	19,537 [R(int) = 0.0342]	21,811 [R(int) = 0.0561]	15,371 [R(int) = 0.0998]	11,856 [R(int) = 0.0769]
no. of observed independent reflections; $I > 2\sigma(I)$	42,803	13,023	13,164	15,898	12,863	7309
final R indices, observed	R1 = 0.0402, wR2 = 0.0867	R1 = 0.0497, wR2 = 0.1172	R1 = 0.0617, wR2 = 0.1364	R1 = 0.0548, wR2 = 0.1276	R1 = 0.0463, wR2 = 0.1073	R1 = 0.0708, wR2 = 0.1789
final R indices, all data	R1 = 0.0527, wR2 = 0.0915	R1 = 0.0751, wR2 = 0.1289	R1 = 0.1062, wR2 = 0.1564	R1 = 0.0830, wR2 = 0.1469	R1 = 0.0603, wR2 = 0.1131	R1 = 0.1233, wR2 = 0.2049

C

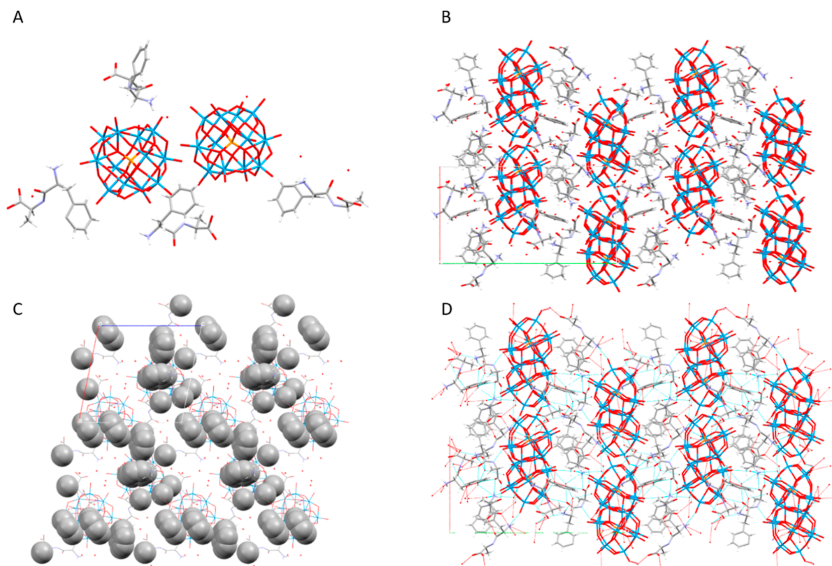


Figure 2. Structure 1 $[(\text{H}_3\text{O})_2(\text{HPhe-Ala})_4[\text{PW}_{12}\text{O}_{40}]\cdot 11\text{H}_2\text{O}]$ shown as (A) molecular arrangement and (B) packing. Highlighted are (C) hydrophobic groups and (D) H-bonds.

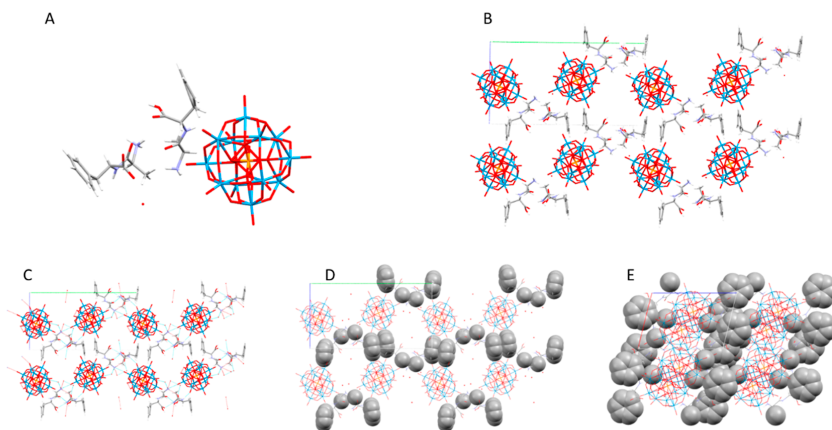


Figure 3. Structure 2 $[(\text{HAla-Phe})_2[\text{HPW}_{12}\text{O}_{40}]\cdot 4\text{H}_2\text{O}]$ shown as (A) molecular arrangement and (B) crystal packing. Highlighted are (C) H-bonding and hydrophobic interactions viewed from the side (D) and from the top (E).

bridging POM oxygen O(16)–O(15) 2.906(4) Å, an amino group O(42)–N(1A) 2.938(4) Å, as well as a contact between an amino group and a carbonyl group N(1B)–O(3A) 2.909(7) Å. Next are a contact between a terminal and bridging POM oxygen O(25)–O(40) 2.961(3) Å, a carboxyl group and an amino group O(1B)–N(1A) 2.973(5) Å, and several contacts between terminal POM oxygen O(16)–O(41) 2.977(3) Å, O(38)–O(11) 3.007(3) Å, and O(18)–O(40) 3.037(3) Å. In addition, there is π -stacking between the Phe side chains. These form pairs from nonequivalent peptides and lie in a parallel displaced conformation (Figure 3E).

Despite containing the same components as 2, the structure of 3 (Figure 4) is quite different. First, the crystal was block-like. Second, the structure appears to be more dense, containing no water molecules and showing less porosity. The POMs are arranged in columns, surrounded by a matrix of peptides, but the peptides are arranged less like a chain and more like a net, with connections to each other in three dimensions (Figure 4B). These connections are both π -stacking (Figure 4C) and H-bonding (Figure 4D), with the former in both face–face and face–edge conformations.

The shortest H-bonds are between carbonyl groups and a carboxyl group O(3B)–O(1C) 2.612(4) Å, and two amino

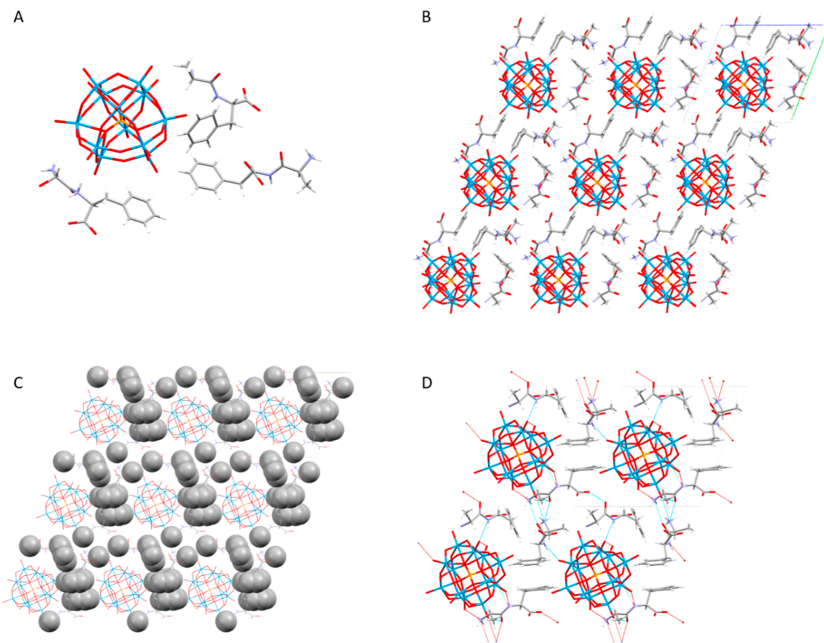


Figure 4. Structure 3 $[(\text{HAla-Phe})_3[\text{PW}_{12}\text{O}_{40}]]$ shown as (A) molecular arrangement and (B) crystal packing. Highlighted are (C) hydrophobic groups and (D) H-bonding.

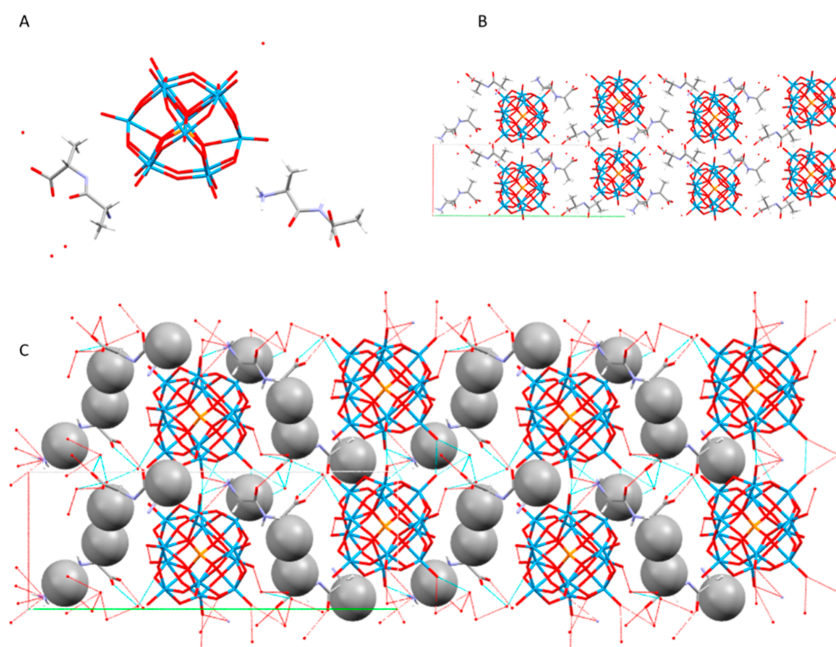


Figure 5. Structure 4 $[(\text{HAla-Ala})_2[\text{HPW}_{12}\text{O}_{40}]\cdot 4\text{H}_2\text{O}]$ shown as (A) molecular arrangement and (B) crystal packing. Highlighted are (C) H-bonding and hydrophobic interactions.

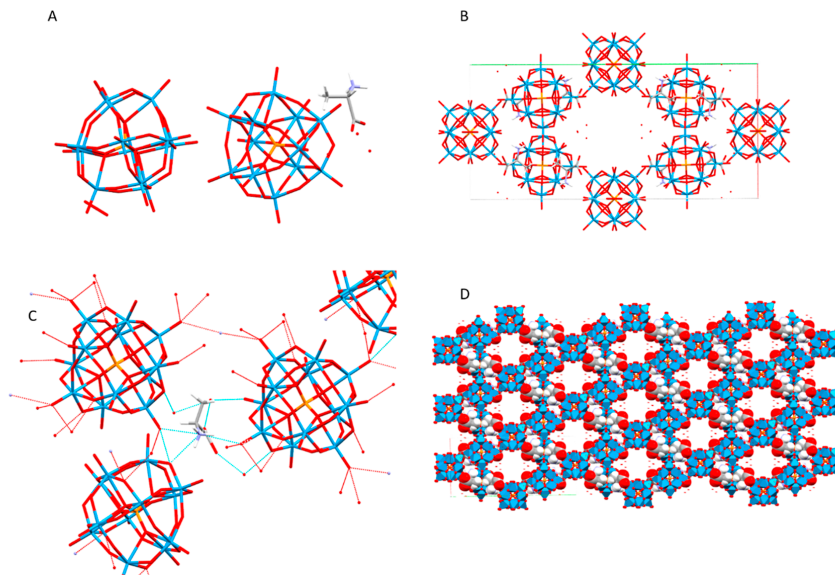


Figure 6. Structure 5 [(HALa)H₂[PW₁₂O₄₀]₂·4H₂O] shown as (A) molecular arrangement and (B) crystal packing. Highlighted are (C) H-bonding and the (D) MOF-like matrix.

groups O(1B)–N(1A) 2.797(3) Å, N(1B)–O(1A) 2.841(3) Å. The rest of the H-bonds are to terminal POM oxygen, with other terminal POM oxygens O(25)–O(1) 2.868(3), O(12)–O(9) 3.017, bridging POM oxygen O(18)–O(9) 2.895(2) Å, amine groups O(27)–N(1B) 2.906(4) Å, O(37)–N(1A) 2.948(3) Å, amide groups O(1)–N(2C) 2.992(3) Å, O(36)–N(2A) 2.996(3) Å, O(9)–N(2B) 3.001(3) Å, O(12)–N(2B) 3.018(3) Å, and a carbonyl group O(37)–O(1B) 3.023(3) Å.

The colorless, block-shaped crystals forming the structure of 4 (Figure 5) contain far more H-bonds compared to complexes 2 and 3, likely due to the comparatively lower hydrophobicity of the peptide. The main force directing this structure appears to be H-bonding, while in 2 and 3, it appears to be π -stacking, though van der Waals interactions (approximately 4 Å) between the Ala side chains are visible (Figure 5C).

The shortest H-bonds are between carboxyl groups and carbonyl groups, O(3A)–O(2B) 2.655(4) Å and O(2A)–O(3B) 2.666(3) Å, and between water molecules, O(1X)–O(2X) 2.669(9) Å, O(2X)–O(4X) 2.727(10), and O(2X)–O(3X) 2.779(10) Å. Next are contacts between water molecules and carboxyl groups, O(1B)–O(1X) 2.718(4) Å, O(1A)–O(3X) 2.871(6) Å, terminal POM oxygen O(30)–O(4X) 2.862(4) Å, O(32)–O(3X) 2.917(5) Å, or bridging POM oxygen O(9)–O(1X) 2.932(3) Å. The longest H-bonds are between two terminal POM oxygens, O(30)–O(38) 2.960(3) Å, O(4)–O(6) 2.977(2) Å, and O(34)–O(39) 3.038(3) Å, a carboxyl group and a water molecule, O(2A)–O(4X) 3.003(5) Å, terminal POM oxygen, and one particular amino group, O(31)–N(2B) 2.962(3) Å, and O(4)–N(2B) 2.988(3) Å, and O(6)–N(2B) 3.017(3) Å and O(37)–N(2B) 3.029(3) Å, a water molecule, O(38)–O(4X) 2.963(4) Å, or bridging POM oxygen, O(7)–O(31) 3.018(3) Å and O(37)–

O(12) 3.023(3) Å. In addition, two Ala side chains form a van der Waals interaction, with C(3A)–C(3B) 4.023(8) Å.

Structure 5 (Figure 6) was synthesized using trialanine, though it contains only the monomer, and formed large, colorless, block-shaped crystals. Most likely, the acidic conditions degraded the peptide bonds over time, as the sample was left for several months before crystals formed. The structure is remarkably porous, with voids approximately 12 × 8 × 5 Å in volume (Figure 6B,D). This structure is reminiscent of metal–organic frameworks (MOFs), though as it is held together by H-bonds (Figure 6C) rather than covalent bonds, it should not be considered a true MOF.

The H-bonding network is extensive, with the shortest contacts being between water and a carboxyl group, O(2A)–O(3AA) (2.454(7) Å), and two water molecules, O(1AA)–O(4AA) 2.637(6) Å. Slightly longer are H-bonds between bridging POM oxygen and water O(22)–O(3AA) 2.782(5) Å, terminal POM oxygen and the amine group O(25)–N(1A) 2.788(2) Å, O(17)–N(1A) 2.910(2) Å, and terminal POM oxygen and water O(18)–O(4AA) 2.923(5) Å. The longest contacts are between POM oxygens O(24)–O(17) 2.929(2) O(25)–O(7) 2.960(1) Å, O(17)–O(17) 2.973(2) Å, and O(25)–O(25) 3.028(2) Å, bridging POM oxygen and the amine group O(7)–N(1A) 2.959(2) Å, a carboxyl group and water O(1A)–O(1AA) 3.008(5) Å, and terminal POM oxygen and water O(11)–O(1AA) 3.028(3) Å. In addition, there are hydrophobic interactions between the Ala side chains, causing the formation of isolated pairs of the amino acid between the POMs. The amine group is in contact with three adjacent POMs (Figure 5C), and each such triad is touched by two amine groups at the center. The pattern of the side chains interacting with each other is reflected in the structure of pure L-alanine,²⁰ as well as in those of leucine²¹ and isoleucine,²² begging the question of whether a MOF-like structure with

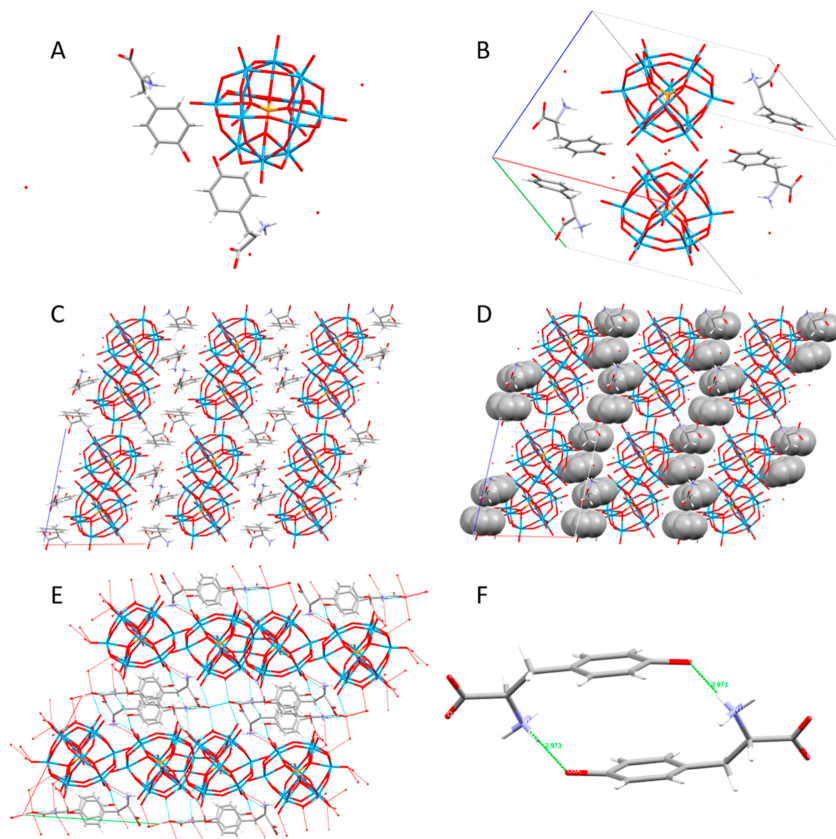


Figure 7. Structure **6** [(HTyr)₂[HPW₁₂O₄₀]·4H₂O] shown as (A) molecular arrangement and (B) crystal packing. Highlighted are the (C) layering of the packing, (D) chains of π -stacked rings, (E) H-bonding in the whole structure, and (F) H-bonding between stacked amino acids.

larger voids could be produced using the amino acids with longer side chains.

6 (Figure 7) is a light brown, needle-shaped crystal, with phosphotungstate forming a complex with an amino acid rather than an oligopeptide, though its relevance for the sake of comparison with Phe cannot be overlooked. Tyr has a carbonyl group on the phenyl ring, allowing for additional H-bonding as well as π -stacking. The structure shows a chain of stacked rings (Figure 7C,D), with the amino acids alternating in the direction, allowing for lateral connections between stacks (Figure 7E), as well as occasional H-bonds between the carbonyl and amine groups (Figure 7F).

The structure contains a number of H-bonds, the shortest of which are between water and a carboxyl group O(1X)–O(2A) 2.719(4) Å, two water molecules O(2A)–O(3A) 2.767(5) Å, and between terminal POM oxygen and carbonyl groups O(33)–O(3X) 2.793(3) Å, O(29)–O(3Y) 2.804(3) Å. Slightly weaker are bonds between water molecules and terminal POM oxygen O(21)–O(6A) 2.869(6) Å; an amine group, N(1X)–O(2A) 2.894(4) Å; bridging POM oxygen O(7)–O(4A) 2.897(4) Å; and terminal POM oxygen O(5)–O(6A) 2.897(6) Å. Next come bonds between terminal POM

oxygens O(29)–O(49) 2.904(3) Å, O(34)–O(39) 2.957(3) Å, bridging POM oxygen and water O(24)–O(3A) 2.914(6) Å, terminal POM oxygen and an amine group O(34)–N(1X) 2.944(3) Å, and a carbonyl group and an amine group O(3X)–N(1X) 2.973(3) Å. The weakest bonds are from terminal POM oxygen to other terminal POM oxygens, O(5)–O(21) 2.980(2) Å, O(18)–O(21) 2.988(3) Å, an amine group, O(36)–N(1Y) 2.984(3), bridging POM oxygen, O(26)–O(34) 2.991(4) Å, and water, O(38)–O(2A) 3.024(3) Å. In addition to H-bonds, there are π -interactions between the aromatic rings in the side chains.

It should be noted that atoms C(2Y), C(3Y), O(1Y), and N(1Y) are highly disordered, and their positions may in reality be more varied than the structure suggests, and atom C(2X) was disordered and had to be treated to fix thermal deviation parameter for the most probably atomic arrangement. There are also voids likely containing a disordered solvent.

EDS spectra of **1**, **3**–**6** were taken (Figure S1), showing the composition to be of tungsten, phosphorus, oxygen, nitrogen, and carbon in the approximate ratios one would expect from the structure (Tables S1–S5), with minor variations likely due to dried mother liquor, which also explains the presence of

chloride in some samples. FTIR spectra of 1, 3–5 were taken (Figure S2–S5), showing that the carboxyl groups are likely protonated for those peptides.

The Phe-containing structures all displayed isolated pockets of π -stacking, while H-bonding to the environment occurred via the oxygen- and nitrogen-containing groups. The same pattern is found in globular proteins, which typically have a hydrophobic core and a hydrophilic surface. Ala-containing peptides had a weak tendency to place the Ala side chains in contact with each other, likely due to their hydrophobicity. We have shown previously that longer oligopeptides tend to direct structure formation more strongly than shorter ones, and may cause a different ratio of POM to peptide in the crystal than there was in solution,^{10,11} as was also the case here. It is reasonable to suggest that the side chains direct complex formation before crystal nucleation and so dictate the structure of the crystal to a degree. This is much like how a protein will fold its hydrophobic side chains toward each other as it is extruded from the ribosome, while hydrophilic groups seek each other to form the secondary structures of α -helices and β -sheets.

As for the contacts between peptides and POMs, 1 shows mainly H-bonding with the amine group, and 2 has only two direct contacts, with amine and amide groups. 3 also has both types, but more of them. 4 has several H-bonds to amine groups, and 5 has two amine groups central to each POM triad. In 6, POMs have H-bonds to the amino group, as well as the carbonyl group on the ring. The rings in 1–3 lie with the edge toward POMs, while in 6, the angle is less perpendicular but still not face-on. All rings appear wedged between terminal oxygen and lie closer to the bridging oxygen.

The difference between compounds 2 and 3 is notable. 3 appears more dense, with no water or cavities in the structure. The main difference between their syntheses is the speed of formation. A slower evaporation yielded a denser and more highly ordered packing, in that 2 showed “chains” of peptides (Figure 3B), while 3 showed a “web” of peptides (Figure 4B). 3 also has three rings involved in their stacks, compared to the pairs in 2. The additional time afforded to 3 may have allowed for a more sophisticated network, possibly by allowing the peptides to arrange themselves into stable clusters before the nucleation event, although the exact dynamics remain to be determined. As phosphotungstate is considered a superchaotropic ion,²³ it may be that chaotropic forces affect 2 more strongly than 3. 2 and 3 should also be compared to 1. Simply switching the order of the amino acids produced a remarkably different structure. Not only does 1 display nearly twice the H-bonds compared to 2 and 3 (normalized against Z), but the POMs are also arranged in layers rather than the columns seen in 2 and 3. Again, a seemingly insignificant factor produced a major effect on the structure. Finally, 6 should be compared to 1, 2, and 3. As with Phe, it is clear that π -interactions from Tyr molecules are the main force forming the structure. Adding the possibility of H-bonding to the carbonyl group and the lack of steric hindrance from other residues, the stacks form long chains rather than isolated pockets, somewhat inverting the pattern of POM columns in 2 and 3. The stacks and POMs are also arranged in layers, reflecting the motif in 1. Tyr-forming H-bonds support the findings that they are partially responsible for deformation of spider silk fibers in high humidity.⁴ The findings presented here also imply that NPs have the capacity to impact the structure and properties of protein-based composite materials. The MOF-like 5 may also

deserve some interest, as polyoxometalate-based MOFs (PMOFs) have gained attention in recent years.²⁴ Li and Wu²⁵ outline how amphiphilic ligands can form supramolecular frameworks by binding a POM at the hydrophilic head and one another at the hydrophobic tail, which is exactly what can be seen in structure 5. Using POMs and amino acids, instead of late transition metals and polypyridines or carboxylates, as materials for H-bonded nanoporous structures could present a distinct advantage.

CONCLUSIONS

Six structures of complexes with Phe, Ala, or Tyr with phosphotungstic acid have been synthesized. Columns of NPs surrounded by an organic framework and columns of π -stacked aromatic rings could be expected in composite materials with similar precursors. The addition of hydrophobic peptides moves structures from standard hexagonal packing seen for spherical particles such as Keggin POMs, and instead, we see cubic packing for many of these structures enforced by the self-assembly of the peptide ligands. These structures reveal core principles behind the formation of NP-biomolecule composites and may be used for a more refined method of designing such materials.

ASSOCIATED CONTENT

Supporting Information

The Supporting Information is available free of charge at <https://pubs.acs.org/doi/10.1021/acs.cgd.4c00806>.

Details of data collection and refinement for all six structures, EDS analysis of crystals of all obtained materials (both spectra and contents of elements in table form), FTIR spectra of compounds 3–5 with indication of most important adsorption bands, and atomic coordinates and selected bond lengths and angles for compounds 1–6 (PDF)

Accession Codes

CCDC 2362067–2362072 contain the supplementary crystallographic data for this paper. These data can be obtained free of charge via www.ccdc.cam.ac.uk/data_request/cif, or by emailing data_request@ccdc.cam.ac.uk, or by contacting The Cambridge Crystallographic Data Centre, 12 Union Road, Cambridge CB2 1EZ, UK; fax: +44 1223 336033.

AUTHOR INFORMATION

Corresponding Author

Vadim G. Kessler – Department of Molecular Sciences, Swedish University of Agricultural Sciences, Uppsala 750 07, Sweden; orcid.org/0000-0001-7570-2814; Email: vadim.kessler@kemi.slu.se

Authors

Björn Greijer – Department of Molecular Sciences, Swedish University of Agricultural Sciences, Uppsala 750 07, Sweden
Edgar Stigell – Department of Molecular Sciences, Swedish University of Agricultural Sciences, Uppsala 750 07, Sweden
Timothe Guerin – Department of Molecular Sciences, Swedish University of Agricultural Sciences, Uppsala 750 07, Sweden

Complete contact information is available at: <https://pubs.acs.org/doi/10.1021/acs.cgd.4c00806>

Notes

The authors declare no competing financial interest.

ACKNOWLEDGMENTS

The authors are grateful to Prof. Gulaim Seisenbaeva for valuable comments and help with FTIR measurements. The support from the Swedish Research Council (Vetenskapsrådet) to the grant Molecular mechanisms in oxide nanoparticle interactions with proteins, 2022-03971_VR, is gratefully acknowledged.

REFERENCES

- (1) Sharma, V. K.; Filip, J.; Zboril, R.; Varma, R. S. Natural Inorganic Nanoparticles – Formation, Fate, and Toxicity in the Environment. *Chem. Soc. Rev.* **2015**, *44* (23), 8410–8423.
- (2) Soria-Carrera, H.; Atrián-Blasco, E.; Martín-Rapún, R.; Mitchell, S. G. Polyoxometalate–Peptide Hybrid Materials: From Structure–Property Relationships to Applications. *Chem. Sci.* **2023**, *14* (1), 10–28.
- (3) Kessler, V. G.; Seisenbaeva, G. A. Molecular Mechanisms of the Metal Oxide Sol-Gel Process and Their Application in Approaches to Thermodynamically Challenging Complex Oxide Materials. *J. Sol-Gel Sci. Technol.* **2023**, *107* (1), 190–200.
- (4) Greco, G.; Arndt, T.; Schmuck, B.; Francis, J.; Bäcklund, F. G.; Shilkova, O.; Barth, A.; Gonska, N.; Seisenbaeva, G.; Kessler, V.; Johansson, J.; Pugno, N. M.; Rising, A. Tyrosine Residues Mediate Supercontraction in Biomimetic Spider Silk. *Commun. Mater.* **2021**, *2* (1), 43.
- (5) Hardy, J.; Selkoe, D. J. The Amyloid Hypothesis of Alzheimer's Disease: Progress and Problems on the Road to Therapeutics. *Science* **2002**, *297* (5580), 353–356.
- (6) Kurbasic, M.; Garcia, A. M.; Viada, S.; Marchesan, S. Tripeptide Self-Assembly into Bioactive Hydrogels: Effects of Terminus Modification on Biocatalysis. *Molecules* **2021**, *26* (1), 173.
- (7) Marchesan, S.; Vargiu, A. V.; Stryan, K. E. The Phe-Phe Motif for Peptide Self-Assembly in Nanomedicine. *Molecules* **2015**, *20* (11), 19775–19788.
- (8) Lynch, I.; Dawson, K. A. Protein-Nanoparticle Interactions. *Nano Today* **2008**, *3* (1–2), 40–47.
- (9) Cedervall, T.; Lynch, I.; Lindman, S.; Berggard, T.; Thulin, E.; Nilsson, H.; Dawson, K. A.; Linse, S. Understanding the Nanoparticle-Protein Corona Using Methods to Quantify Exchange Rates and Affinities of Proteins for Nanoparticles. *Proc. Natl. Acad. Sci. U.S.A.* **2007**, *104* (7), 2050–2055.
- (10) Rominger, K. M.; Nestor, G.; Eriksson, J. E.; Seisenbaeva, G. A.; Kessler, V. G. Complexes of Keggin POMs [PM12O40]3– (M = Mo, W) with GlyGly Peptide and Arginine—Crystal Structures and Solution Reactivity. *Eur. J. Inorg. Chem.* **2019**, *2019* (39–40), 4297–4305.
- (11) Greijer, B.; De Donder, T.; Nestor, G.; Eriksson, J. E.; Seisenbaeva, G. A.; Kessler, V. G. Complexes of Keggin POMs [PM12O40]3– (M = Mo, W) with GlyGlyGly and GlyGlyGlyGly Oligopeptides. *Eur. J. Inorg. Chem.* **2021**, *2021* (1), 54–61.
- (12) Greijer, B. H.; Nestor, G.; Eriksson, J. E.; Seisenbaeva, G. A.; Kessler, V. G. Factors Influencing Stoichiometry and Stability of Polyoxometalate – Peptide Complexes. *Dalton Trans.* **2022**, *51* (24), 9511–9521.
- (13) Absillis, G.; Parac-Vogt, T. N. Peptide Bond Hydrolysis Catalyzed by the Wells–Dawson Zr(α_2 -P₂W₁₇O₆₁)₂ Polyoxometalate. *Inorg. Chem.* **2012**, *51* (18), 9902–9910.
- (14) Vandebroek, L.; Van Meervelt, L.; Parac-Vogt, T. N. Direct Observation of the ZrIV Interaction with the Carboxamide Bond in a Noncovalent Complex between Hen Egg White Lysozyme and a Zr-Substituted Keggin Polyoxometalate. *Acta Crystallogr., Sect. C: Struct. Chem.* **2018**, *74* (11), 1348–1354.
- (15) Ly, H. G. T.; Parac-Vogt, T. N. Spectroscopic Study of the Interaction between Horse Heart Myoglobin and Zirconium(IV)-Substituted Polyoxometalates as Artificial Proteases. *ChemPhysChem* **2017**, *18* (18), 2451–2458.
- (16) Bijelic, A.; Aureliano, M.; Rompel, A. The Antibacterial Activity of Polyoxometalates: Structures, Antibiotic Effects and Future Perspectives. *Chem. Commun.* **2018**, *54* (10), 1153–1169.
- (17) Breibeck, J.; Bijelic, A.; Rompel, A. Transition Metal-Substituted Keggin Polyoxotungstates Enabling Covalent Attachment to Proteinase K upon Co-Crystallization. *Chem. Commun.* **2019**, *55* (77), 11519–11522.
- (18) Bijelic, A.; Dobrov, A.; Roller, A.; Rompel, A. Binding of a Fatty Acid-Functionalized Anderson-Type Polyoxometalate to Human Serum Albumin. *Inorg. Chem.* **2020**, *59* (8), 5243–5246.
- (19) Zhao, Y.; Wang, Z.; Ni, J.; He, P. Self-Assembly of Polyoxometalate Clusters into Nanostructures with Different Dimensions. *Eur. J. Inorg. Chem.* **2024**, No. e202400184.
- (20) Simpson, H. J.; Marsh, R. E. The Crystal Structure of L-Alanine. *Acta Crystallogr.* **1966**, *20* (4), 550–555.
- (21) Coll, M.; Solans, X.; Font-Altaba, M.; Subirana, J. A. Structure of L-Leucine: A Redetermination. *Acta Crystallogr., Sect. C: Struct. Chem.* **1986**, *42* (5), 599–601.
- (22) Torii, K.; Itaka, Y. The Crystal Structure of L-Isoleucine. *Acta Crystallogr., Sect. B: Struct. Sci., Cryst. Eng. Mater.* **1971**, *27* (11), 2237–2246.
- (23) Assaf, K. I.; Nau, W. M. The Chaotropic Effect as an Assembly Motif in Chemistry. *Angew. Chem., Int. Ed.* **2018**, *57* (43), 13968–13981.
- (24) Zhang, Y.; Liu, Y.; Wang, D.; Liu, J.; Zhao, J.; Chen, L. State-of-the-Art Advances in the Syntheses, Structures, and Applications of Polyoxometalate-Based Metal–Organic Frameworks. *Polyoxometalates* **2023**, *2* (1), 9140017.
- (25) Li, B.; Wu, L. Perspective of Polyoxometalate Complexes on Flexible Assembly and Integrated Potentials. *Polyoxometalates* **2023**, *2* (1), 9140016.

the mode of action of TATT against the enveloped virus was through interaction with membrane phospholipids.

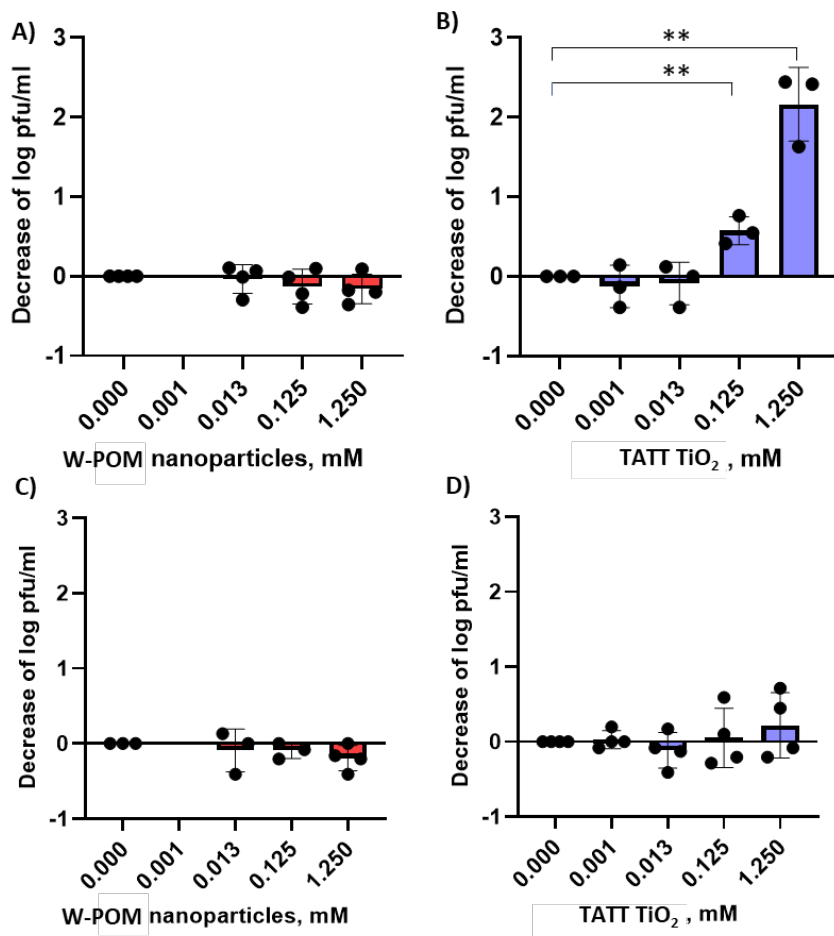


Figure 1. Effect of NPs of silicotungstate POM (POM) and TATT on TGEV virus (A,B) and EMCV virus (C,D). The TATT concentration is given with respect to particles, not TiO₂ formula unit. Decrease in infectivity (log decrease in plaque forming units (PFU)/mL) in the presence of different concentrations of NPs is shown. Asterisks mark data points statistically different from control experiment according to ANOVA statistical analysis.

Binding models for ³¹P NMR study at different temperature and pH 7.0

Aiming to verify our suggestion that the interaction between particles and the virus occurs via strong complexation of the TATT NP with membrane phospholipids, resulting in potential

ACTA UNIVERSITATIS AGRICULTURAE SUECIAE

DOCTORAL THESIS No. 2024:69

Mineral nanoparticles are abundant in our surroundings, and are often produced artificially. It is necessary to understand how they affect living things. To study this, we have produced a number of X-ray crystal structures of nanoparticles in complex with oligopeptides. Through these, we identified a number of factors which determine how nanoparticles might interact with biomolecules. We also produced materials by sol-gel method from the nanoparticles, which acted as a remarkably efficient catalyst.

Björn H. Greijer received his graduate education at the Department of Molecular Sciences, SLU, Uppsala. He received his Bachelor's degree in Biology and Master's degree in Applied Biotechnology from Uppsala University.

Acta Universitatis Agriculturae Sueciae presents doctoral theses from the Swedish University of Agricultural Sciences (SLU).

SLU generates knowledge for the sustainable use of biological natural resources. Research, education, extension, as well as environmental monitoring and assessment are used to achieve this goal.

ISSN 1652-6880

ISBN (print version) 978-91-8046-360-7

ISBN (electronic version) 978-91-8046-396-6